

# **Interfaces of Ionic Liquids and of Liquid Metals Studied by X-Ray Photoelectron Spectroscopy**

**Grenzflächen ionischer Flüssigkeiten  
und flüssiger Metalle untersucht mit  
Röntgenphotoelektronenspektroskopie**

Der Naturwissenschaftlichen Fakultät der  
Friedrich-Alexander-Universität Erlangen-Nürnberg  
zur Erlangung des Doktorgrades Dr. rer. nat.

vorgelegt von  
**Florian Rietzler**  
aus Illertissen

Als Dissertation genehmigt  
von der naturwissenschaftlichen Fakultät  
der Universität Erlangen-Nürnberg

Tag der mündlichen Prüfung: 24.6.2016

Vorsitzender des Promotionsorgans: Prof. Dr. Jörn Wilms

Gutachter: Prof. Dr. Hans-Peter Steinrück  
Prof. Dr. Jörg Libuda





---

## Contents

<b>1. Introduction and Motivation .....</b>	<b>1</b>
<b>2. Fundamentals and Techniques .....</b>	<b>5</b>
2.1. Ionic Liquids .....	5
2.2. Angle-Resolved X-Ray Photoelectron Spectroscopy .....	10
2.3. Experimental Setup .....	15
2.4. Sample Preparation .....	17
2.5. Data Acquisition and Analysis .....	21
<b>3. The Ionic Liquid / Carbon Interface .....</b>	<b>25</b>
3.1. The Ionic Liquid / HOPG Interface .....	28
3.1.1. Growth Behavior .....	28
3.1.2. Initial Adsorption Behavior .....	31
3.2. The Ionic Liquid / Graphene Interface .....	34
3.2.1. Graphene Growth .....	34
3.2.2. Adsorption and Growth on Nickel-Supported Graphene .....	35
3.3. Summary and Conclusions .....	38
<b>4. The Ionic Liquid / Metal Interface .....</b>	<b>41</b>
4.1. Introducing Electrospray Ionization Deposition of Ionic Liquids .....	42
4.1.1. Proof of Principle: $[\text{C}_8\text{C}_1\text{Im}][\text{Tf}_2\text{N}]$ on Au(111) .....	44
4.1.2. Thin Films of $[\text{C}_8\text{C}_1\text{Im}]\text{Cl}$ on Au(111) .....	49
4.1.3. Atomic Force Microscopy Investigations .....	54
4.1.4. Optical Microscopy Investigations .....	55
4.1.5. Conclusions .....	56
4.1.6. Summary .....	57
4.2. $[\text{C}_2\text{C}_1\text{Im}][\text{EtOSO}_3]$ and $[\text{C}_2\text{C}_1\text{Im}][\text{OTf}]$ on Pristine and Modified Au Surfaces .....	59
4.2.1. Thermal Decomposition of $[\text{C}_2\text{C}_1\text{Im}][\text{EtOSO}_3]$ .....	59

4.2.2. PVD vs. ESID [C <sub>2</sub> C <sub>1</sub> Im][EtOSO <sub>3</sub> ] Thin Films.....	66
4.2.3. Initial Adsorption Behavior .....	68
4.2.4. Growth Mode .....	70
4.2.5. Influence of Surface Carbon on [C <sub>2</sub> C <sub>1</sub> Im][EtOSO <sub>3</sub> ] Thin Films on Au(111) .....	71
4.2.6. Growth and Adsorption of [C <sub>2</sub> C <sub>1</sub> Im][OTf] Thin Films on Pristine Au(111) .....	74
4.2.7. Influence of Pd Deposition on [C <sub>2</sub> C <sub>1</sub> Im][OTf] Thin Films .....	76
4.2.8. Summary and Conclusions .....	81
<b>5. Surface Properties of Pd-Ga and Pt-Ga Alloys .....</b>	<b>85</b>
5.1. Pd Deposition onto Ga <sub>2</sub> O <sub>3</sub> / Ga.....	89
5.2. Surface Composition of a Low Pd Content Pd-Ga Alloy .....	93
5.3. Surface Composition of Pd-Ga-Based Catalysts.....	95
5.4. Oxidation of Pt-Ga Alloys .....	100
5.5. Summary and Conclusions.....	103
<b>6. Summary and Outlook .....</b>	<b>107</b>
<b>7. Zusammenfassung und Ausblick.....</b>	<b>113</b>
<b>8. Appendix.....</b>	<b>119</b>
8.1. [C <sub>1</sub> C <sub>1</sub> Im][Tf <sub>2</sub> N] on 1.7 L Graphene .....	119
8.2. Au 4f Data – Pd / [C <sub>2</sub> C <sub>1</sub> Im][OTf] / Au(111) .....	123
<b>9. Bibliography .....</b>	<b>124</b>
<b>List of Abbreviations .....</b>	<b>138</b>
<b>Acknowledgements .....</b>	<b>141</b>





## 1. Introduction and Motivation

According to the common definition, ionic liquids (ILs) are entirely ionic compounds with a melting point (MP) below 100 °C. Therefore, aqueous solutions of salts do not match this definition as they do not consist entirely of ions.<sup>1</sup> Ethylammonium nitrate, the first compound which nowadays would be called an IL was first synthesized by Walden as soon as 1914,<sup>2</sup> but it took nearly a century for ILs to gain wider interest in the scientific community. However, since the turn of the millennium, the number of publications involving ILs is strongly increasing, as visualized in Figure 1.1.

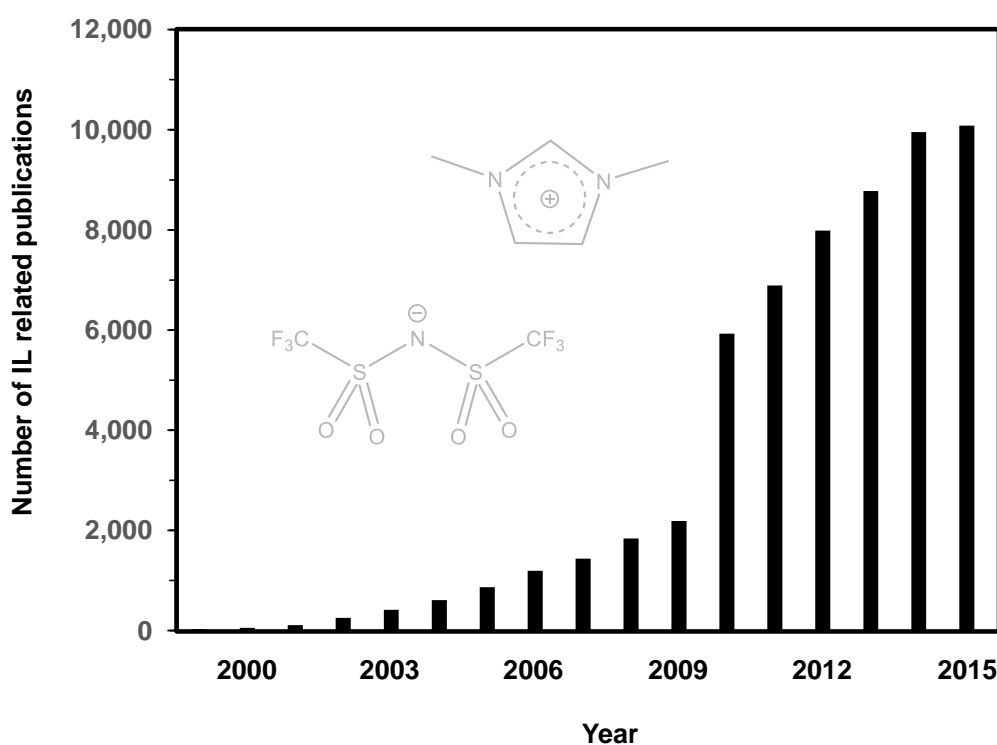


Figure 1.1: Annual number of publications related to ionic liquids. Numbers from Web of Science.<sup>3</sup>

ILs with desired properties can be designed by the selected combination of certain anions and cations. Hence, ILs have drawn the attention of scientists in many research fields. They can be used to replace conventional solvents in synthesis which leads in many cases to an increase of reactivity and selectivity.<sup>4, 5</sup> With their broad electrochemical window, ILs have also been proven as perfect electrolytes for

many electrochemical applications, such as fuel cells,<sup>6, 7</sup> electrodeposition,<sup>8-10</sup> electrochemical double layer capacitors,<sup>11-16</sup> and solar cells.<sup>17-20</sup> Last but not least, ILs led to the development of completely new approaches to catalysis, namely, solid catalyst with ionic liquid layer (SCILL) and supported ionic liquid phase (SILP) (cf. Figure 1.2).<sup>21-23</sup>

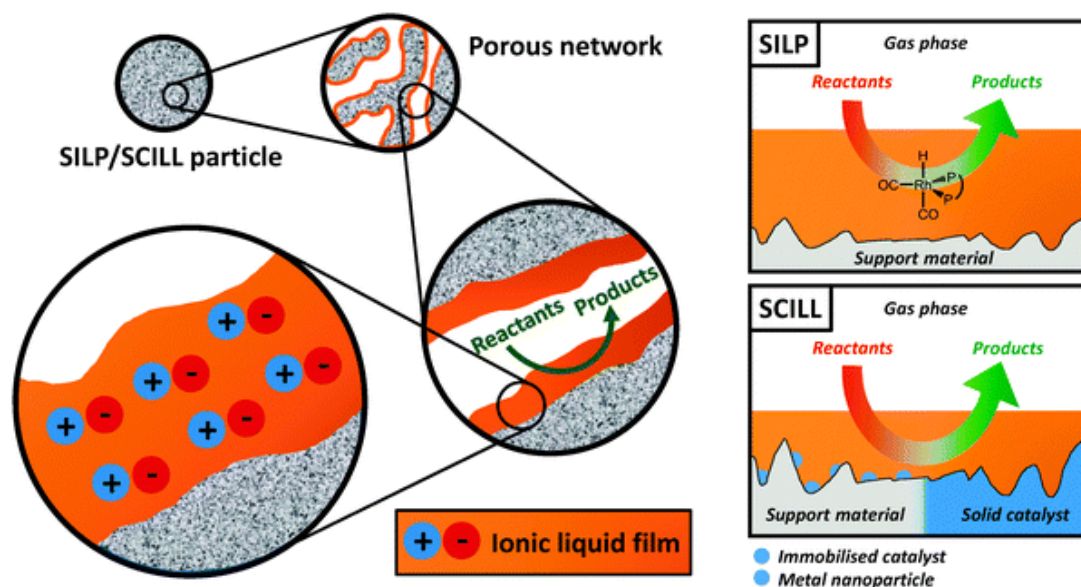


Figure 1.2: Schematic drawing of the SILP and SCILL concepts, taken from reference <sup>24</sup>.

The SILP concept (cf. Figure 1.2, top right) is based on a porous inert support material coated with a thin IL layer. Therein, the actual catalyst is homogeneously dissolved. SILP combines the advantages of homogenous catalysis (highly product- and stereo-selective) and heterogeneous catalysis (stationary catalyst phase of a continuous flow reactor). In SCILL systems (cf. Figure 1.2, bottom right), where the catalyst material or catalytically active species immobilized on a solid support material is impregnated with an IL layer, enhanced selectivity, product distribution and yields may be observed. This is achieved by specific interactions of the IL with reactive sites of the heterogeneous catalyst particles or by solubility and mass transport changes when reactants and products diffuse through the IL to/from the catalyst surface.<sup>24</sup>

The low vapor pressure of ILs allows for the investigation of IL surfaces with UHV techniques, such as X-ray photoelectron spectroscopy (XPS),<sup>25-27</sup> ultraviolet photoelectron spectroscopy (UPS),<sup>28-31</sup> near edge X-ray absorption fine structure (NEXAFS),<sup>30, 32, 33</sup> metastable impact electron spectroscopy (MIES),<sup>28, 29</sup> low energy ion scattering (LEIS),<sup>34</sup> time-of-flight secondary ion mass spectrometry

---

(ToF-SIMS)<sup>35-37</sup> or high resolution electron energy loss spectroscopy (HREELS),<sup>29</sup> which are traditionally restricted to solid samples. For thin IL films applied in the context of SILP and SCILL catalysis, besides the outer IL surface, structure and composition of the IL/solid (IL/metal and IL/oxide) interface are of particular interest. Also for applications in the field of electrochemistry, profound knowledge about the IL/solid (IL/metal and IL/carbon) interface is indispensable for further advancements. Thus, during the last years, the IL/solid interface is drawing increasing attention and has been studied with numerous techniques including sum frequency generation (SFG),<sup>38, 39</sup> scanning tunneling microscopy (STM),<sup>40-42</sup> atomic force microscopy (AFM),<sup>41, 43</sup> neutron reflectometry,<sup>44</sup> and XPS<sup>40, 45-48</sup>.

In this work, angle-resolved XPS (ARXPS) was applied in order to deepen the knowledge on the IL/solid interface properties. The thesis is structured as follows: After this introduction, in chapter 2, fundamental information on the applied materials and techniques, as well as on the experimental setup is given. In chapters 3 and 4 results on the IL/solid interface will be presented. Chapter 3 is devoted to the IL/carbon interface, more precisely, to the interface of in-situ prepared thermally evaporated ultrathin IL films with highly ordered pyrolytic graphite (HOPG) and Nickel-supported graphene. Chapter 4 deals with the IL/metal interface, particularly in the context of SCILL catalysis. Along the way, electrospray ionization deposition (ESID) is introduced as an alternative technique for IL thin film production for thermally unstable ILs. In the following, ARXPS investigations on interface properties of ultrathin IL films – prepared alternately by thermal deposition or ESID – on pristine and modified gold surfaces are presented. After the detailed studies on the IL/solid interface, in chapter 5, it's about time to think a bit outside the IL box and the focus is drawn on a novel kind of non-IL catalytic concept: porous supports coated with a thin film consisting of low amounts of a catalytically active noble metal (platinum or palladium) dissolved in a liquid metal (gallium). Besides fundamental research on the surface composition of pristine and oxidized Ga alloy surfaces, structure and composition of real catalysts were investigated by means of XPS. Chapters 3 – 5 each feature a separate introduction providing further insights on the respective subjects.



## 2. Fundamentals and Techniques

### 2.1. Ionic Liquids

Historical aspects and some common applications involving ILs have already been mentioned in the introduction. In this section, important physicochemical properties of ILs in general, as well as in more detail for the specific ILs applied within this work will be discussed.

IL cations usually possess an organic structure of low symmetry with a positively charged nitrogen or phosphorus atom being part of the cationic head group.<sup>49</sup> Typical cations are based for instance on ammonium, phosphonium, imidazolium, pyridinium or pyrrolidinium, which are usually completely substituted at the hetero atoms.<sup>49</sup> Typical IL anions are weakly basic inorganic or organic compounds with a diffuse or protected negative charge.<sup>49</sup> Besides, also purely inorganic ILs are known, as for instance hydrazonium bromide  $[\text{N}_2\text{H}_5]\text{Br}$  or hydrazonium nitrate  $[\text{N}_2\text{H}_5][\text{NO}_3]$  with MPs of 86.5 and 70 °C, respectively.<sup>1</sup> Whereas most research on ILs has focused on ILs with non-protonated cations, i.e. on so called aprotic ILs,<sup>1</sup> some ILs are formed by a proton transfer between an equimolar mixture of a Brønsted acid and a Brønsted base.<sup>49</sup> These ILs therefore include an exchangeable proton and consequentially are called protic ILs. More recently, functionalized ILs become increasingly important. These “task-specific” ILs are designed for specific purposes in catalysis or synthesis.<sup>1, 49</sup> Another promising class of ILs are chiral ILs, which are potentially useful as solvents or chiral catalysts for asymmetric organic synthesis.<sup>1</sup>

The low MP of ILs stems from their molecular structure. Unlike typical high-boiling salts such as NaCl, which are composed of small ions with the positive and negative charge being located mainly on a single atom, the large IL ions possess widely delocalized electron structures. The resulting low molecular charge densities of both the cation and the anion lead to very low lattice energies of the salts and consequentially also to low MPs.<sup>50</sup> Moreover, their usually bulky, asymmetric shape causes an additional low packing efficiency in the lattice structure, which is also

contributing to a low MP.<sup>51</sup> Compared to conventional liquids, due to their ionic nature, ILs exhibit some unique physicochemical properties. Of particular importance for this work is their extremely low vapor pressure, which at RT is in the order of  $10^{-10}$  mbar,<sup>52</sup> allowing for the investigation of IL surfaces in UHV via XPS. For higher temperatures, the IL vapor pressure increases gradually. Zaitsau et. al experimentally determined the vapor pressure of different ILs. At a temperature of  $\sim 450$  K, the observed vapor pressure of all investigated ILs was in the order of  $10^{-5}$  mbar.<sup>53</sup> In many cases, the relatively high vapor pressure of ILs at elevated temperatures allows for their thermal evaporation in UHV for thin film production. This method, referred to as IL physical vapor deposition (IL-PVD), was established in Erlangen at the Chair of Physical Chemistry II<sup>45, 46</sup> and represents one of the main techniques during the work on this thesis. Some ILs, however, are thermally unstable.<sup>54, 55</sup> Upon heating, these ILs start to decompose at temperatures, which are still too low for an appreciable evaporation rate necessary for PVD. During the work on this thesis, this drawback was addressed to by introducing ionic liquid electrospray deposition (IL-ESID) as an alternative technique for IL thin film production, which can be applied independently of the thermal stability of an IL.<sup>56</sup>

All ILs applied in the experiments of this work possess an 1,3-dialkylimidazolium based cation (cf. Figure 2.1), each substituted at the N<sub>1</sub> and N<sub>3</sub> positions with one methyl and another alkyl chain of variable length (methyl, ethyl or octyl). The most prominent feature of the imidazolium structure is the aromatic ring system, leading to high stability and excellent liquescency due to the delocalization of the positive charge and thus low charge density.<sup>57</sup> Charge on C<sub>4</sub> and C<sub>5</sub> is almost neutral, but carbon C<sub>2</sub> is positively charged due to the electron deficit in the C=N bond, making C<sub>2</sub>-H slightly acidic.<sup>58</sup> Accordingly, C<sub>2</sub>-H was found to be an excellent hydrogen bond donor.<sup>59, 60, 61</sup> Besides its hydrogen-bonding ability, coulombic and dispersive forces contribute to the interactions of an imidazolium based cation with the respective counterion. Compared to Coulomb-dominated traditional ionic compounds such as NaCl, for an imidazolium based IL, theoretical calculations suggest a much stronger contribution of dispersive forces on the overall interionic interactions, leading to a flattening of the repulsive region of the potential, providing another explanation for the low MP of imidazolium based ILs.<sup>62</sup> For alkyl chain lengths < 8 carbon atoms, the so-called symmetry-breaking

region, a decrease of the MP is observed with increasing chain length, whereas for alkyl chains  $\geq 8$  the MP increases with increasing chain length as a result of the increasing van der Waals interactions.<sup>63</sup>

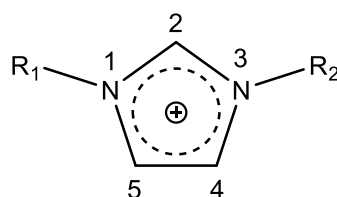


Figure 2.1: General structure of 1,3-dialkylimidazolium cations.

The most frequently used anion of this work is  $[\text{Tf}_2\text{N}]^-$  (cf. Figure 2.2a). Its bulky structure, the negative charge being distributed over the whole  $[\text{O}_2\text{S-N-SO}_2]$  moiety and the additional electron-withdrawing non-coordinating  $\text{CF}_3$ -groups make  $[\text{Tf}_2\text{N}]^-$  a perfect IL anion.<sup>64</sup> Additional key factors for the low MP of  $[\text{Tf}_2\text{N}]^-$  ILs are the large number of nearly degenerate low energy conformations and the shielding of the negatively charged ionic center by the bulky triflate ( $\text{CF}_3\text{SO}_2$ ) groups, both impeding the formation of a stable crystal structure.<sup>65</sup> Imidazolium  $[\text{Tf}_2\text{N}]$  ILs are known to be thermally stable and can easily be used for the preparation of thin films by means of thermal evaporation.<sup>45-48</sup>

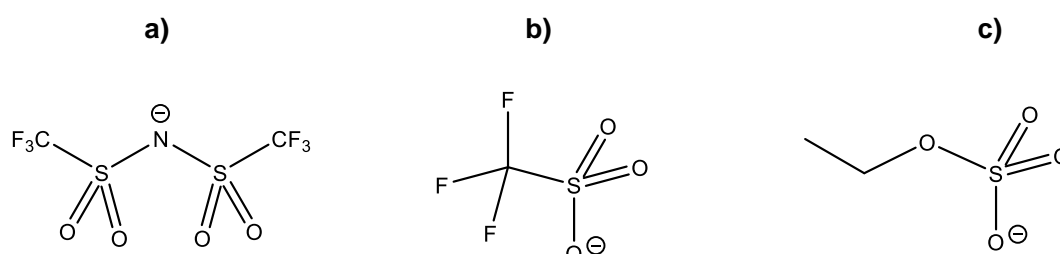


Figure 2.2: Structures of a) bis(trifluoromethylsulfonyl)imide ( $[\text{Tf}_2\text{N}]^-$ ), b) trifluoromethanesulfonate ( $[\text{OTf}]^-$ ), and c) ethyl sulfate ( $[\text{EtOSO}_3]^-$ ).

Besides  $[\text{Tf}_2\text{N}]^-$ , for particular studies also other anions were applied. Imidazolium-based ILs with the chemically related – however less bulky – trifluoromethanesulfonate ( $[\text{OTf}]^-$ ) anion (cf. Figure 2.2b) were shown to be thermally inert, similar to imidazolium  $[\text{Tf}_2\text{N}]$  ILs.<sup>54</sup> ILs composed of the ethyl sulfate ( $[\text{EtOSO}_3]^-$ ) anion (cf. Figure 2.2c) and an 1,3-dialkylimidazolium cation are known to be highly hygroscopic as both, the C-H groups in the dialkylimidazolium ring and particularly the  $-\text{SO}_3$  group in the ethyl sulfate anion are characteristic moieties interacting with water molecules by hydrogen bonding.<sup>66</sup> Furthermore,

imidazolium [EtOSO<sub>3</sub>]<sup>-</sup> ILs are known to be thermally unstable and show a tendency to decomposition over evaporation when heated at atmospheric pressure.<sup>67</sup> Nevertheless, evaporation of intact ion pairs was successful when thin IL films were heated under UHV conditions.<sup>68</sup> The small size and the highly localized charge of the chloride anion leads to a significantly higher MP of corresponding – thermally unstable – dialkylimidazolium ILs.<sup>69</sup> Chemical structures and the most relevant properties of the ILs applied in this work are summarized in table 2.1.

IL	M (g/mol)	MP (°C)	$\delta$ (g/cm <sup>3</sup> )	$\sigma$ (mJ/ K·m <sup>2</sup> )	$d_{ML}$ (Å)	Structure
1,3-dimethyl- imidazolium bis(trifluoromethyl- sulfonyl)imide  [C <sub>1</sub> C <sub>1</sub> Im][Tf <sub>2</sub> N]	377.29	26 <sub>70</sub>	1.57 (25 °C) <sub>71</sub>	36.3 (25 °C) <sub>71</sub>	7.4	
1-methyl-3-octyl- imidazolium bis(trifluoromethyl- sulfonyl)imide  [C <sub>8</sub> C <sub>1</sub> Im][Tf <sub>2</sub> N]	475.41	-86* <sub>72</sub>	1.32 (25 °C) <sub>53</sub>	29.5 (25 °C) <sub>71</sub>	8.4	
1-methyl-3- octylimidazolium chloride  [C <sub>8</sub> C <sub>1</sub> Im]Cl	230.78	-87* <sub>69</sub>	1.00 (25 °C) <sub>69</sub>	30.9 (25 °C) <sub>71</sub>	7.2	
1-methyl-3- ethylimidazolium trifluoromethane- sulfonate  [C <sub>2</sub> C <sub>1</sub> Im][OTf]	260.23	-9 <sub>73</sub>	1.39 (22 °C) <sub>73</sub>	44.2 (27 °C) <sub>74</sub>	6.8	
1-methyl-3- ethylimidazolium ethyl sulfate  [C <sub>2</sub> C <sub>1</sub> Im][EtOSO <sub>3</sub> ]	236.29	-78.4* <sub>75</sub>	1.24 (20 °C) <sub>76</sub>	48.79 (25 °C) <sub>77</sub>	6.8	

Table 2.1: IUPAC names, molar masses ( $M$ ), melting points ( $MP$ , \*glass transition temperatures), densities ( $\delta$ ), surface tensions ( $\sigma$ ), estimated thicknesses of 1 ML according to equation 5 ( $d_{ML}$ ), and chemical structures of the ILs applied in this work.

## 2.2. Angle-Resolved X-Ray Photoelectron Spectroscopy

X-ray photoelectron spectroscopy (XPS), also known as electron spectroscopy for chemical analysis (ESCA), can be used to determine the elemental composition of the outer surface of condensed material. XPS is based on the photoelectric effect, which was discovered in 1887 by Hertz and explained by Einstein in 1905.<sup>78, 79</sup> In its simplest approximation, XPS describes a single step process in which an electron initially bound to an atom/ion is ejected by a photon (cf. Figure 2.3a); the excited electron leaves the sample without energy loss and is detected by an electron analyzer (cf. Figure 2.3c).<sup>80</sup>

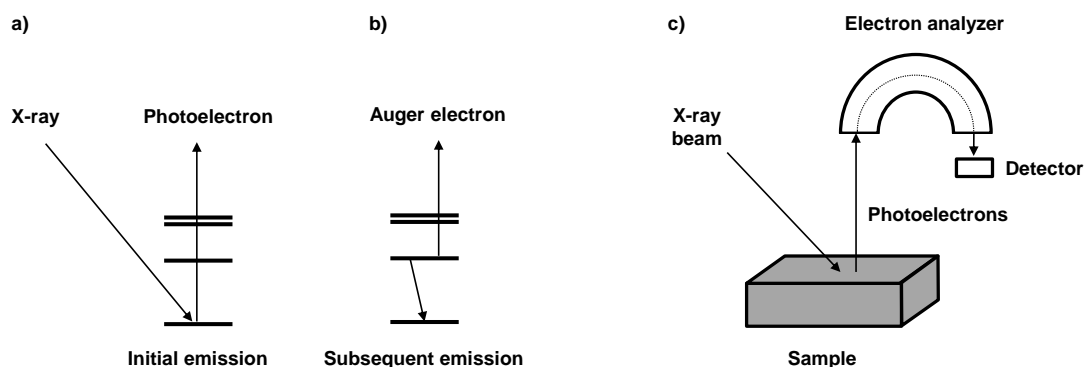


Figure 2.3: a) Schematic scheme of the photoelectron process. b) Subsequent Auger de-excitation process. c) Basic setup of an XPS instrument.

This photoelectron possesses a defined kinetic energy  $E_{kin}$  which depends on the binding energy (BE) of the electron and the energy of the impinging photon  $h\nu$  and which can be measured with an energy dispersive electron analyzer (e.g., a hemispherical analyzer). Thus, by knowing  $E_{kin}$  and  $h\nu$ , BE can be determined by the Einstein equation 1.<sup>80</sup>

$$BE = h\nu - E_{kin} \quad (1)$$

However, equation 1 is only valid for gas phase measurements, because for condensed matter the work functions of both the sample and the analyzer have to be considered. Thus, the analyzer has to be calibrated either to the Fermi level or to an XPS line from which the BE is known. In this case the Einstein equation can be extended to equation 2.<sup>80</sup>

$$BE = h\nu - E_{kin} - \phi_{spec} = h\nu - E_{kin}^{eff} \quad (2)$$

The binding energy of a core electron is influenced by its chemical environment. These so-called chemical shifts mainly depend on the change of the oxidation state and lie within a range of 0.1 – 10 eV. Having measured a certain chemical shift in XPS, conclusions on the oxidation state of the elements of a sample can be drawn.<sup>80</sup> The kinetic energy of a photoelectron is higher for a negative and lower for a positive partial charge.<sup>81</sup> The effect of a permanent partial charge of the emitting atom on the kinetic energy of the photoelectron is counted to the so-called initial state effects.<sup>81</sup> Besides, there are additional – so-called final state – effects which have to be taken into account.<sup>82</sup> Both terms refer to the respective energies in the photoemission process resulting in the measured BE,<sup>80</sup>

$$BE = E_f^{N-1} - E_i^N \quad (3)$$

with  $E_i^N$  being the energy of the ground state with N electrons and  $E_f^{N-1}$  being the final state with N-1 electrons. An important final state effect is the relaxation of an electron system in response to the creation of a core hole. Besides, multi-electron excitations such as plasmon losses or shake-up and shake-off transitions are counted to the group of final state effects.<sup>80</sup> All these processes have in common that upon photoemission, an electronically excited final state is created. Consequentially, the photoelectron obtains less kinetic energy, leading to satellite lines shifted to higher BE relative to the main peak.<sup>81</sup> Satellite peaks by shake-up and shake-off processes occur when an additional electron is excited from an occupied into a bound unoccupied state or into a state in the continuum just above the vacuum level, respectively.<sup>81</sup>

In a common XP spectrum, the measured intensities are plotted against the corresponding BE (cf. Figure 2.4). For s-type orbitals, only one peak is observed. For p, d and f orbitals the peaks are split into doublets. This is due to the coupling between spin and a non-zero orbital angular momentum ( $l > 0$ ) for p, d and f shells, which leads to two non-degenerate states with total angular momentums of  $j_+ = l + 1/2$  and  $j_- = l - 1/2$ .<sup>80</sup>

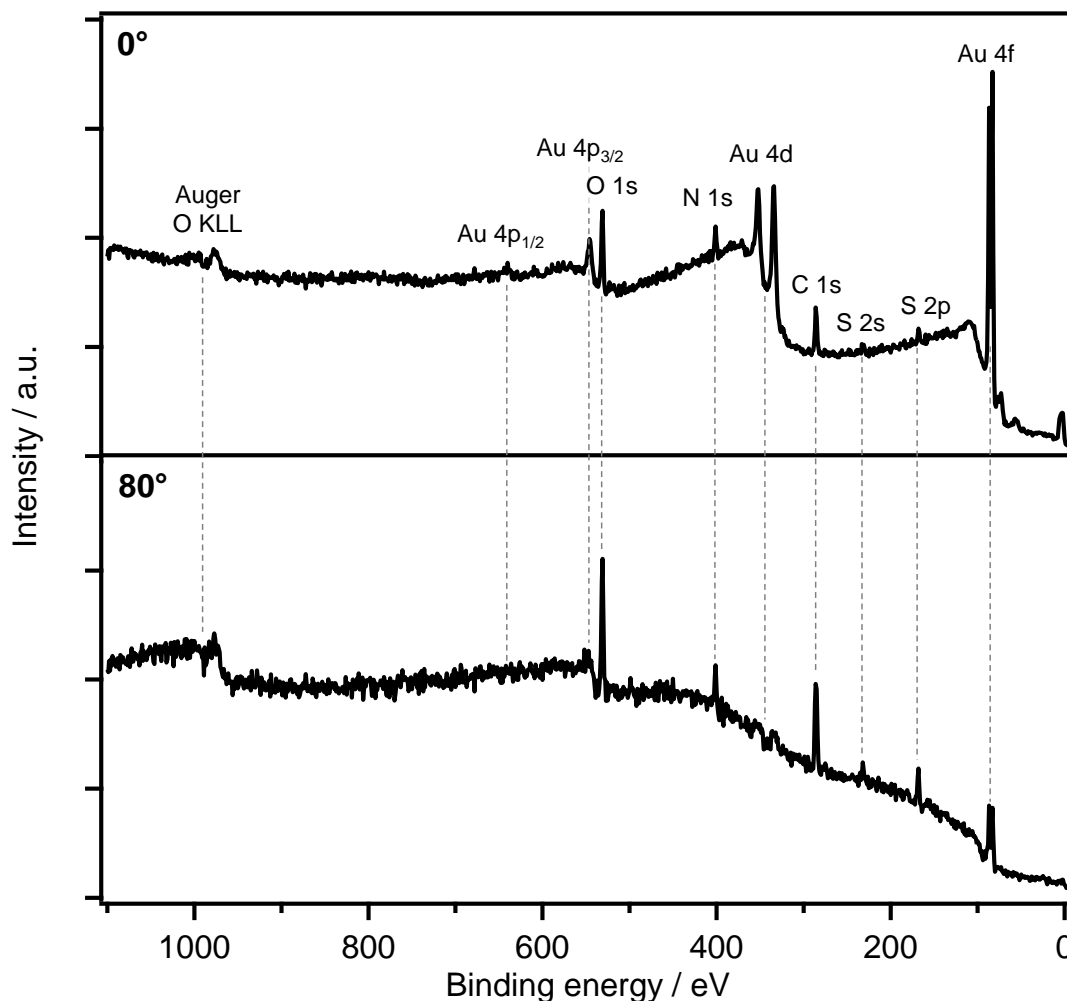
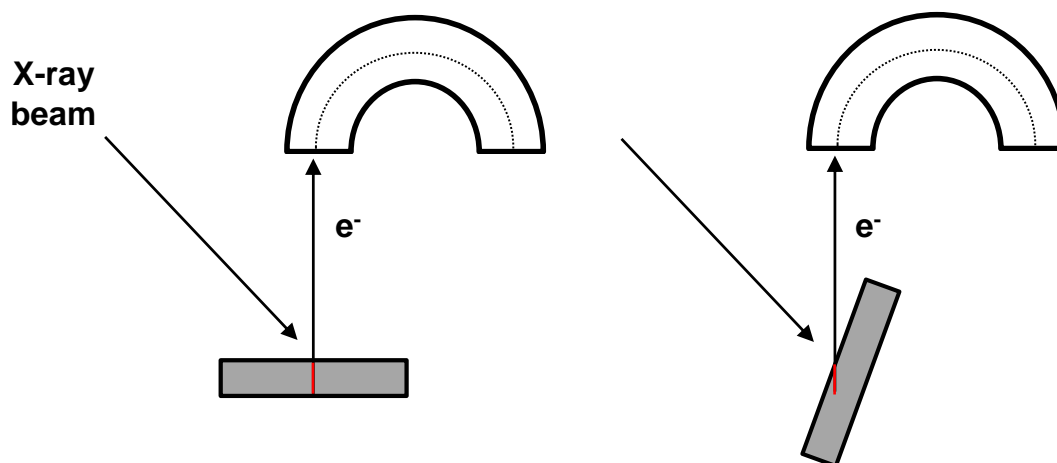


Figure 2.4: XPS overview scans of an ultrathin  $[C_2C_1Im][EtOSO_3]$  IL film deposited onto Au(111) via electrospray ionization, recorded in normal (top) and  $80^\circ$  (bottom) emission.

As demonstrated in Figure 2.4, additional signals occur in the spectra due to the so-called Auger effect, where the positive hole, left behind by the escaped photoelectron, can be filled by an electron originating from an energetically higher-lying shell. The energy that is set free in this process is transferred to another electron of the same shell. This Auger electron is then also emitted from the sample (cf. Figure 2.3b).<sup>80</sup> Unlike photoelectrons, the kinetic energy of an Auger electron does not depend on the energy of the primary X-ray beam but only on the energy difference of the two core levels involved in the Auger process.

Emitted photo- and Auger electrons interact with the surrounding matter. Apart from elastic scattering, these interactions cause energy losses of the primary photoelectrons. Additionally, secondary electrons can be generated. These events result in the formation of a superimposed background signal, which is reflected in

an increase of the overall XPS intensity with increasing BE (cf. Figure 2.4). The mean travelling distance before an excited photoelectron is inelastically scattered, is called inelastic mean free path (IMFP). Depending on kinetic energy and density of the surrounding, the IMFP is typically 0.5 – 3 nm for matter.<sup>83</sup> Due to the small IMFP of photoelectrons, ultra-high vacuum (UHV) conditions are required for XPS. Therefore, for a long time, the technique was limited mainly to solid materials, as the usually much higher vapor pressure of liquids did not allow for measurements under UHV. ILs and liquid metals, which are analyzed in this work, deviate from this rule as both classes of materials exhibit vapor pressures comparable to solid matter.



*Figure 2.5: Schematic principle of ARXPS: The information depth decreases when tilting the sample relative to the entrance of the analyzer.*

In order to further enhance surface sensitivity, the sample can be tilted relative to the electron analyzer. As seen in Figure 2.5, the total path length the emitted photoelectrons travel through the sample before inelastic scattering occurs, remains the same, but the information depth decreases.<sup>84</sup> This method is called angle-resolved XPS (ARXPS) and is the main technique applied in this work. With ARXPS information about growth modes and the composition of ultra-thin films is accessible.<sup>85</sup> The influence of the emission angle on an XP spectrum can be seen in Figure 2.4 showing the spectra of an ultrathin  $[\text{C}_2\text{C}_1\text{Im}][\text{EtOSO}_3]$  film deposited onto Au(111) via electrospray ionization, recorded in 0 and 80°. Whereas the same core levels are observed in both emission angles, their relative intensities differ. Due to the larger information depth, in normal emission the substrate-related Au peaks are much more intense compared to 80° emission. Vice versa, the IL-related

signals (S 2p, S 1s, C 1s, N 1s, O 1s, and the oxygen's KLL Auger line) stemming from the upper most layers of the sample are enhanced in the surface sensitive 80° geometry. Detailed information on acquisition and analysis of the ARXPS data is given in chapter 2.5.

## 2.3. Experimental Setup

The modified ESCALAB 200 UHV system used for the experiments of this work consists of three chambers: an analysis chamber, a preparation chamber and a sample transfer system (load lock), allowing for the introduction of samples into the main UHV chambers without venting (cf. Figure 2.6).

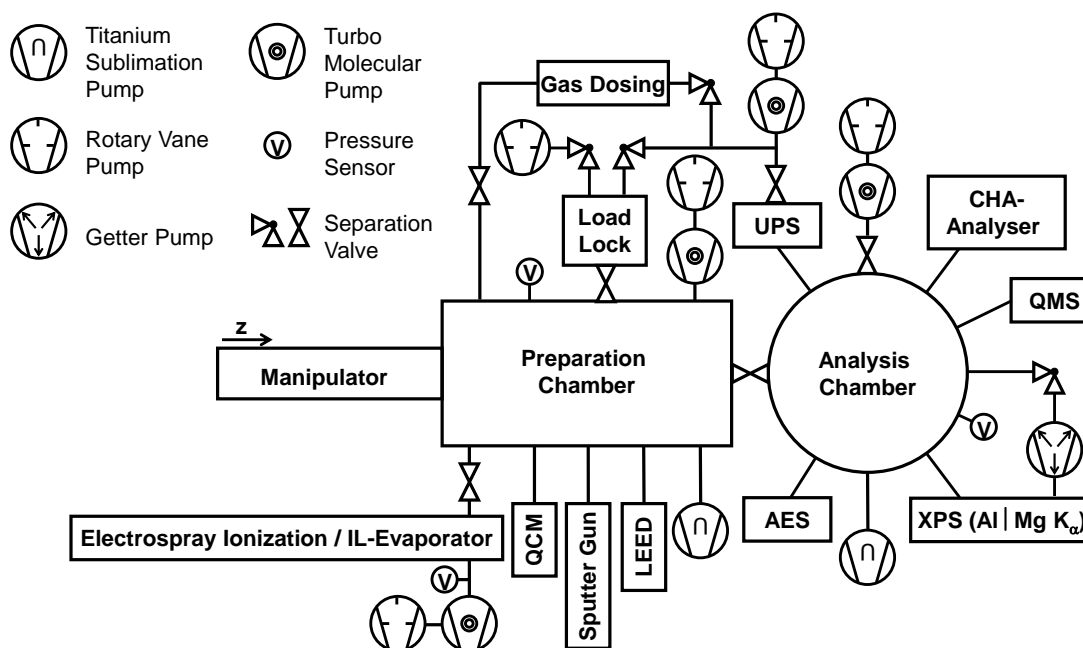


Figure 2.6: Schematic overview of the ESCALAB 200 UHV system in its current state. Adapted from reference<sup>86</sup>.

XPS measurements are performed in the analysis chamber, which is equipped with a SPECS XR50 dual anode X-ray gun, generating Al K $\alpha$  or Mg K $\alpha$  radiation and a SCIENTA R3000 hemispherical electron energy analyzer. The preparation chamber provides a sputter gun for sample cleaning with accelerated Ar<sup>+</sup> ions. Both the IL evaporator and the ESID apparatus can be mounted to the preparation chamber without venting of the chamber. Flux of the IL evaporator can be monitored by a flexible quartz crystal microbalance (QCM). A gas dosing system is attached to the preparation chamber by a fine control valve. For analyzing a sample's surface structure, the preparation chamber is equipped with low-energy electron diffraction (LEED) optics. The system's manipulator offers 360° continuous rotation, a thoria-doped tungsten filament for heating (which can also be used for electron bombardment heating from backside, with the sample being set under high voltage) and the possibility of mounting a detachable device for cooling

the system with liquid nitrogen (down to 90 K). A detailed description of the original setup of the ESCALAB 200 system and its basic modifications are given elsewhere.<sup>87</sup> More recent modifications, such as the replacement of the old manipulator and the original X-ray gun and electron analyzer, and the attachment of the IL evaporator have been discussed in reference <sup>86</sup>. During the work on this thesis the electrospray system was introduced as a novel method for IL thin film production.

## 2.4. Sample Preparation

### Au(111)

The Au(111) single crystal with a size of 11 x 11 x 2 mm<sup>3</sup> was purchased from MaTecK (purity 99.999 %, one side polished and aligned to the (111) plane with an accuracy better than 0.1°). It was mounted onto a Mo sample holder and fixed with two Ta wires. Surface preparation was performed by sputtering with 1.0 keV Ar<sup>+</sup> ions, followed by annealing at ~800 K. Sample cleanliness was checked by XPS. For the atomic force microscopy (AFM) measurements, the IL films were deposited onto mica substrates coated with epitaxial gold films of 0.3 μm thickness (Georg Albert PVD) with preferential (111) surface orientation.<sup>88</sup>

### Highly-Ordered Pyrolytic Graphite (HOPG)

The HOPG single crystal with a mosaic spread of 0.8° ± 0.2° was purchased from MaTecK (15 x 15 x 2 mm<sup>3</sup>; purity 99.99 %). The crystal was mounted on a Mo sample holder with a double-coated carbon conductive tab. Surface preparation was performed ex-situ by cleaving the HOPG with adhesive tape. The cleanliness of the sample was checked with XPS.

### Ni(111)-supported graphene

The Ni(111) single crystal (MaTecK; 11 x 11 x 2 mm<sup>3</sup> size; purity 99.99 %; one side polished to the (111) plane better than 0.1°) was mounted on a Mo sample holder and fixed with two Ta wires. It was cleaned by 1 keV Ar<sup>+</sup> ion sputtering at room temperature (RT). Surface order was restored by annealing at ~1100 K. Rapid cooling of the sample with the liquid N<sub>2</sub> cooling system was necessary in order to prevent surface segregation of impurities (especially sulfur). The cleanliness of the Ni(111) surface was confirmed by XPS and LEED.

Submonolayer (0.6 layer) and monolayer (1.0 layer) graphene were grown on Ni(111) by in-situ chemical vapor deposition (CVD). Ni(111) has been chosen as support for graphene, because of its small lattice mismatch of only 1.3 % to graphene.<sup>89</sup> Thus, graphene adopts an almost perfectly flat geometry, in contrast to

other transition metal surfaces, on which graphene grows in a corrugated Moiré structure to compensate for significant lattice mismatches. The experimentally deduced vertical spacing between graphene and supporting Ni(111) ranges from 2.1 – 2.8 Å,<sup>90, 91</sup> which is considerably smaller than the interplanar spacing in graphite (3.4 Å). Graphene was prepared at temperatures of 800 – 900 K by a combination of carbon segregation from the nickel bulk<sup>92</sup> and CVD with butene at a chamber pressure of  $\sim 10^{-5}$  mbar, using a nozzle pointing towards the sample. The achieved graphene coverage was determined by XPS; note that the LEED pattern always showed a clear 1x1 pattern independent of the graphene coverage.

## Pd Deposition

Ultrathin films of Pd were evaporated with a Focus EFM 3 electron beam evaporator, which was mounted to the preparation chamber of the UHV system. For Pd deposition, electrons were accelerated towards a positively biased Pd rod from a surrounding tungsten filament. Heat radiation was adsorbed by a water-cooled shroud; throughout the deposition procedure, the pressure inside the preparation chamber did not exceed  $1 \times 10^{-10}$  mbar. Deposition time was controlled by a manual built-in shutter. Prior to the experiments, the flux was calibrated by QCM and by XPS. For this purpose, Pd was deposited onto a clean Au(111) single crystal and the attenuation of Au 4f substrate signals was monitored upon Pd deposition. Before and after each deposition, the Pd flux was checked for constancy by QCM. Additionally, during deposition, the integral flux monitor was used for real-time control of the deposition rate. As Pd is known to form surface alloys with Au even at RT,<sup>93</sup> comparative measurements were performed with a N<sub>2</sub> (l) cooled Au(111) crystal as for low temperatures surface alloying can successfully be suppressed.<sup>93</sup> In contrast to the surface sensitive 80° data, no influence of the surface alloy formation on the Pd/Au XPS intensity ratio was found in normal emission. Therefore, only the 0° data were used for calibration of the Pd flux. The evaporator's distance from the sample was chosen large enough to ensure homogeneous Pd deposition across the sample. As the Pd beam partly consists of accelerated Pd cations, which could create defects in the substrate surface similar to Ar<sup>+</sup> sputtering, the sample was positively biased with + 1 kV vs. ground to prevent the impact of high energy ions.

---

## Physical Vapor Deposition of Ionic Liquids

Ultrathin IL films were prepared by ionic liquid physical vapor deposition (IL-PVD) using a modified high-temperature Knudsen cell for organic materials (Tetra WKC3) onto the substrates kept at RT. The evaporation temperature of the Knudsen cell was regulated to temperatures between 430 and 445 K by a Eurotherm 2261 controller with an accuracy of  $\pm 1$  K, using a type-K thermocouple. The IL flux was checked using a quartz crystal microbalance (QCM) before and after each deposition step. The QCM was calibrated by deposition of the IL onto a Au(111) single crystal before and after each deposition series. Detailed information on the experimental setup can be found in the following publications.<sup>46-48, 86</sup>

## Electrospray Ionization Deposition of Ionic Liquids

IL films were prepared by ESI deposition (IL-ESID) using the UHV<sub>4</sub><sup>+</sup> system (MolecularSpray Ltd.). For deposition both ILs were dissolved in methanol ( $c_{\text{IL}} \approx 10^{-3}$  M). A syringe pump with a constant flow rate of 500  $\mu\text{L}/\text{h}$  transported the IL solution to the emitter needle (NewObjective; inner diameter: 0.1 mm), which was positively biased vs. the grounded entrance capillary by voltages between 1.4 and 1.6 kV. A schematic overview of the experimental setup is shown in Figure 2.7. Three differential pumping stages allowed for the direct attachment of the system to the preparation chamber of the UHV system with a base pressure  $< 10^{-9}$  mbar. The pressure increased to  $\sim 10^{-7}$  mbar during IL deposition. Mass spectrometry (MS) showed that this pressure increase resulted from the evaporating methanol only, as the amount of IL was below the detection limit of the MS-setup. Throughout the IL-ESID procedure, occasional pressure drops indicated misalignment of the beam through the pumping stages into the preparation chamber, which required repositioning of the ESI emission capillary by lateral displacements in the sub-millimeter range. In few cases, the emission permanently dropped due to partial blocking of the capillary – which could be replaced easily. Due to these occasional fluctuations of the beam flux over the very long deposition times, the amount of deposited IL could not be reliably estimated from the deposition time. Thus, the amount of deposited IL was determined from the attenuation of the Au

substrate XPS signals, as it was done in earlier studies.<sup>94</sup> When the sample was positioned perpendicularly to the ion beam and for a distance of 0.7 m between sample and entrance capillary, the deposition area on the sample was circular with a diameter of 4 mm in diameter. This shape was determined using XPS by scanning the sample in front of the analyzer.

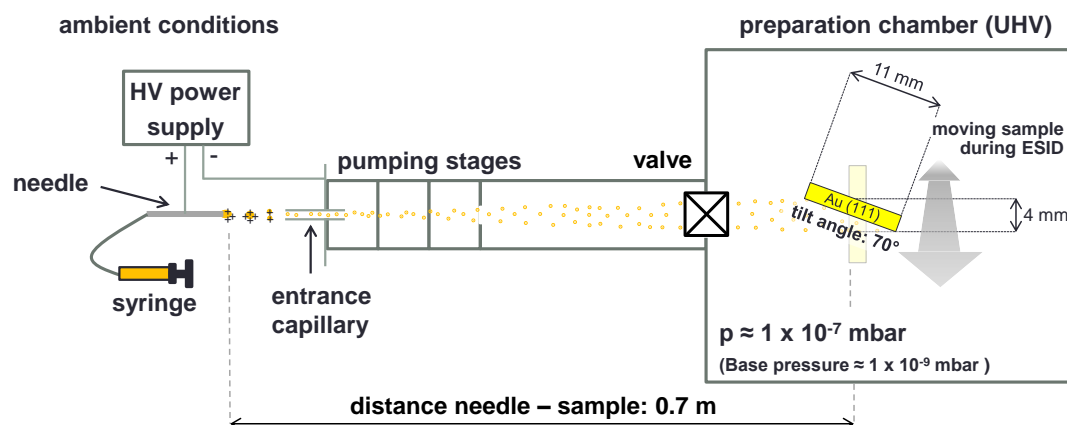


Figure 2.7: Schematic overview of the experimental setup (for details, see text).

In order to achieve a homogeneously covered surface area, which is sufficiently large for ARXPS measurements with the experimental setup, the Au crystal was tilted during IL deposition in one direction to an angle of  $70^\circ$  relative to the ion beam normal, and, additionally, the sample was continuously moved in the perpendicular direction (cf. Figure 2.7) during deposition. The whole deposition process was performed at RT. In order to reduce the radiation damage during XPS, a maximum of three consecutive deposition steps was performed; thereafter, the gold surface was again restored by sputtering and annealing for the following deposition steps.

The  $[\text{C}_8\text{C}_1\text{Im}][\text{Tf}_2\text{N}]$  and  $[\text{C}_8\text{C}_1\text{Im}]\text{Cl}$  thin films for the AFM measurements were prepared in a separate chamber with a base pressure  $< 10^{-8}$  mbar. These films were deposited via IL-ESID onto epitaxially grown Au(111) films supported on mica. The distance between sample and entrance capillary in this setup was significantly shorter (0.4 m), resulting in a smaller deposition area with a diameter of  $\sim 2$  mm.

## 2.5. Data Acquisition and Analysis

### Angle Resolved X-Ray Photoelectron Spectroscopy (ARXPS)

The XP spectra were measured with a VG Scienta R3000 electron analyzer and a SPECS XR 50 X-ray gun using non-monochromatized Al-K $\alpha$  radiation ( $h\nu = 1486.6$  eV) at a power of 250 W ( $U = 12.5$  kV,  $I = 20$  mA). Survey spectra were recorded with a pass energy (PE) of 200 eV, whilst the detailed core level spectra were recorded with a PE of 100 eV (overall resolution FWHM:  $\sim 0.9$  eV). The inelastic mean free path (IMFP) of photoelectrons with energies between 800 and 1300 eV in organic matter is 2 – 3 nm.<sup>95</sup> Consequently, the information depth (ID) of 0° measurements corresponds to 7 - 9 nm, that is several molecular layers. In the more surface sensitive geometry at 80°, the ID is reduced by a factor of  $\sim 6$  down to 1 – 1.5 nm.<sup>46</sup> To account for an overall reduction in intensity at grazing emission, all 80° spectra shown in this work were multiplied by an empirical factor which was determined by measurements of macroscopic films of the respective ILs under identical conditions. For the ultrathin film measurements, all XPS binding energy (BE) values were referenced to the Fermi edge, resulting in BE values of 852.4 eV for the Ni 2p $_{3/2}$  peak of Ni(111), and 284.5 eV for the C 1s peak of HOPG. [C $_1$ C $_1$ Im][Tf $_2$ N] reference XP spectra were measured using a macroscopically thick film, which was prepared ex-situ by spreading about 0.1 ml of the IL onto a polycrystalline Au foil under ambient conditions. For quantification, all IL spectra were fitted with a Voigt profile (30 % Lorentzian contribution) after a Shirley background subtraction. In accordance with previous studies, the C 1s spectra of [C $_1$ C $_1$ Im][Tf $_2$ N] were fitted with constraints for the width-at-half-maximum (FWHM) namely  $\text{FWHM} (C_{\text{cation}}) = \text{FWHM} (C_{\text{anion}}) \times 1.11$ . N 1s spectra were fitted with equal FWHM of the anion and cation contributions.<sup>96</sup> Film thicknesses were determined by analysis of the attenuation of the substrate signals (HOPG C 1s signal for IL/HOPG; C 1s and Ni 2p signals for IL/graphene/Ni(111)) according to equation 4:

$$\frac{I_{d(n)}}{I_0} = e^{\frac{-d(n)}{\lambda \cos \vartheta}} \quad \text{or} \quad d(n) = \lambda \cos \vartheta \cdot \ln \frac{I_0}{I_{d(n)}} \quad (4)$$

$\lambda$  is the inelastic mean free path (IMFP),  $d(n)$  the total film thickness of  $n$  completed layers, and  $\vartheta$  the emission angle with respect to the surface normal. For C 1s

electrons with a kinetic energy around 1200 eV,  $\lambda = 2.8$  nm,<sup>95</sup> whereas for Ni 2p<sub>3/2</sub> electrons with a lower kinetic energy around 630 eV,  $\lambda = 1.6$  nm.<sup>47</sup> In line with earlier publications, the IL film thicknesses are given in monolayers (ML); thereby 1 ML of IL refers to one closed layer of ion pairs with anions and cations on top of each other. The height  $h$  of 1 ML is estimated from the bulk molecular volume  $V_m$ , as derived from the IL's molar mass  $M$  and its mass density  $\rho$ , using equation 5,

$$h = \sqrt[3]{\frac{V_m}{N_A}} = \sqrt[3]{\frac{M}{N_A \cdot \rho}} \quad (5)$$

with  $N_A$  being the Avogadro constant. For instance, this approximation yields a thickness (height) of  $h = 0.73$  nm for [C<sub>1</sub>C<sub>1</sub>Im][Tf<sub>2</sub>N]. According to this coverage definition, one closed layer of ions covering the surface in a so-called checkerboard configuration, with both cations and anions adsorbed directly on the surface next to each other, corresponds to a coverage of 0.5 ML.<sup>46</sup>

To study the IL growth on the HOPG sample, the attenuation of the HOPG C 1s substrate signal was determined at 0° and 80°; on Ni(111), only the 0° signal could be used, since due to the smaller size of this sample, at 80°, minor contributions of the crystal edges (which are not covered by IL), did not allow for a reliable thickness determination. However, since the IL only adsorbed on the front face of the crystal, the IL signals at 80° were used for data analysis.

Due to differences in cross section for the photoelectric effect for different elements and core levels, for quantitative XPS analysis, so-called atomic sensitivity factors (ASF) are required to calculate the relative atomic concentration from the integrated peak area.<sup>97</sup> By multiplying the measured peak intensities of the individual core levels of an XPS spectrum with these specific factors, the intensities are normalized and made comparable. As also the experimental setup has an effect on the measured XPS intensities of different core levels in dependence of the kinetic energy of the respective photoelectrons, for most of the measured core levels, reference substances with known stoichiometry have been measured to determine the respective ASF values (this holds true particularly for all IL related XPS signals). ASF values for Ga and Pd core levels, however, were calculated by applying a setup specific calibration function on literature ASF values determined by Wagner.<sup>98</sup>

---

### Atomic Force Microscopy (AFM)

After ESI deposition of IL films on Au/mica in UHV, AFM measurements were performed under ambient conditions on an Easyscan DFM (Nanosurf) in noncontact mode. In all cases, scanning speed was maximized and free amplitude as well as amplitude reduction minimized (down to a level where stable imaging conditions were still maintained) in order to reduce the influence of the tip on the liquid films. Corresponding images were analyzed with the software WSxM 4.0 (Nanotec Electronica S.L).

### Optical Microscopy (OM)

Samples for analysis with Optical Microscopy (OM) were prepared in the same way as for AFM measurements. The pictures were taken in bright-field mode with a DM2500 M instrument (Leica Microsystems) set to highest possible contrast.

### Mass Spectrometry (MS)

The analysis on the thermal decomposition of  $[\text{C}_2\text{C}_1][\text{EtOSO}_3]$  by mass spectrometry (MS) was conducted in a separate UHV chamber with a base pressure of  $10^{-8}$  mbar. The applied instrument was a Hiden Analytical RC RGA analyzer. Spectra were recorded with the MASsoft software (version 7 professional) in the secondary electron multiplier collection (SEM) mode.



### 3. The Ionic Liquid / Carbon Interface

The content of this chapter is based on the following publication:<sup>99</sup>

*Interface of Ionic Liquids and Carbon: Ultrathin [C<sub>1</sub>C<sub>1</sub>Im][Tf<sub>2</sub>N] Films on Graphite and Graphene*, F. Rietzler, J. Nagengast, H.-P. Steinrück, and F. Maier, *J. Phys. Chem. C*, 2015, **119** (50), 28068–28076.

ILs are promising candidates for the improvement of electrochemical devices. For instance, when combined with graphite or graphene electrodes, ILs show outstanding performance in electric double layer capacitors (EDLC).<sup>11, 12</sup> Graphene, one layer of carbon atoms arranged in hexagonal cells, is the thinnest known material, and yet stronger than diamond.<sup>100</sup> Moreover, graphene exhibits high flexibility, electrical conductivity and thermal stability. It can be fabricated by either top-down (TD) or bottom-up (BU) approaches. Starting material for TD graphene fabrication are bulky graphitic substances which are chopped down to the desired final crystal size. Conversely, BU fabrication is performed by starting with rather small units, which are built up to larger functional constructs.<sup>101</sup> In a UHV environment, graphene can be grown in-situ in a BU approach by chemical vapor deposition (CVD) of carbon-rich precursors (e.g. alkenes) on various metal single crystals such as Co, Ir, Rh, Ni, etc.<sup>102, 103</sup>

Despite the high potential of IL-carbon systems for electrochemical applications, only little is known about the corresponding interfaces. A SFG study of a graphene-covered CaF<sub>2</sub> crystal immersed in the IL [C<sub>4</sub>C<sub>1</sub>Im][MeOSO<sub>3</sub>] revealed only weak interaction of both anions and cations with the graphene layer. For cations in direct contact with the substrate, the alkyl chain was found to be parallel to the graphene plane and the imidazolium ring slightly tilted. Methyl groups of first layer anions exhibit a tilt angle of  $> 40^\circ$ .<sup>104</sup> In some AFM studies focusing on the IL solid interface, dilute IL solutions were applied to create thin IL films by solvent evaporation.<sup>105, 106</sup> Zhang et al. prepared thin films of the IL [C<sub>4</sub>C<sub>1</sub>Im][PF<sub>6</sub>] on HOPG and found ordered IL layers up to a critical coverage, which was in the order

of 1 – 2 layers. Due to the stability of the ordered structures, which could be easily imaged with AFM, an almost solid-like behavior of the adsorbed IL was claimed. For higher coverages, dewetting and the formation of droplets was observed.<sup>106</sup> Only nanodroplets and the total absence of ordered structures were found by Bovio et al. for thin [C<sub>4</sub>C<sub>1</sub>Im][Tf<sub>2</sub>N] films on HOPG. When studying the same IL on non-carbon substrates, such as mica, amorphous silica, and oxidized Si(110)-wafers with AFM, they found very different film morphologies than on HOPG, namely layered IL structures with step heights up to 50 nm.<sup>105</sup> The different adsorption behavior of [C<sub>4</sub>C<sub>1</sub>Im][PF<sub>6</sub>] and [C<sub>4</sub>C<sub>1</sub>Im][Tf<sub>2</sub>N] on HOPG was explained by Zhang et al. by the lower melting point of the latter IL, making it less “solid-like”, and by the larger anion size, which leads to a larger anion-cation distance for the [Tf<sub>2</sub>N]<sup>-</sup> IL on the non-polar graphite surface.<sup>106</sup> Atkins et al. determined solvation force profiles for three ILs, including [C<sub>2</sub>C<sub>1</sub>Im][Ac], by measuring the forces when approaching an AFM tip towards a substrate surface covered with the IL. The force-distance curves revealed an oscillatory behavior with six or seven solvation layers for [C<sub>2</sub>C<sub>1</sub>Im][Ac] on graphite. The [C<sub>2</sub>C<sub>1</sub>Im]<sup>+</sup> ion was found to adopt a flat orientation relative to the substrate.<sup>107</sup>

Theoretical studies of the IL-graphene interface were performed by Feodorov et al. using molecular dynamic simulations (MDS), and by Ghatee et al. using density functional theory (DFT); they simulated the interface of bulk [C<sub>1</sub>C<sub>1</sub>Im][PF<sub>6</sub>] and [C<sub>1</sub>C<sub>1</sub>Im][Cl] with freestanding graphene. For [C<sub>1</sub>C<sub>1</sub>Im][Cl], both studies found a stronger interaction between graphene with the imidazolium cation than with the Cl<sup>-</sup> anion, resulting in a layered structure with alternating layers of cations and anions in close proximity to the graphene layer.<sup>108, 109</sup> In case of [C<sub>1</sub>C<sub>1</sub>Im][PF<sub>6</sub>], no preferred adsorption of cations or anions was found.<sup>108</sup> For both ILs the imidazolium ring tends to be oriented parallel to the graphene plane.<sup>108, 109</sup> The adsorption strength was found to strongly depend on the anion. For Cl<sup>-</sup>, charge transfer from the anion to the cation dominates, resulting in weak IL interaction with the graphene surface. Stronger adsorption was found for [C<sub>1</sub>C<sub>1</sub>Im][PF<sub>6</sub>] on graphene, which was attributed to considerable charge transfer between the cation and graphene.<sup>108</sup> MDS of [C<sub>4</sub>C<sub>1</sub>Im][PF<sub>6</sub>] on graphite suggest the direct adsorption of both anions and cations. Thereby, the cation is oriented parallel to the graphite surface plane and adsorbs more strongly than the anion. Further, layering of the first three layers in

---

proximity to the graphite surface was found.<sup>110, 111</sup> To obtain new insights into the interface of ILs with carbon surfaces, the first systematic angle-resolved X-ray photoelectron spectroscopy (ARXPS) study of ultrathin [C<sub>1</sub>C<sub>1</sub>Im][Tf<sub>2</sub>N] films deposited in-situ onto different graphene surfaces was performed, that is, a partial and a complete graphene layer, grown on Ni(111). For comparison, also [C<sub>1</sub>C<sub>1</sub>Im][Tf<sub>2</sub>N] films deposited onto HOPG were investigated; these corresponding results will be discussed first. [C<sub>1</sub>C<sub>1</sub>Im][Tf<sub>2</sub>N] was chosen for thin film preparation on the different carbon substrates, because (a) PVD of this IL occurs without any thermal decomposition, (b) the growth of this IL on bare Ni(111) was already studied in detail,<sup>47</sup> and (c) the carbon signals of the IL do not interfere with carbon signals from graphite or graphene in XPS due to the absence of alkyl chains in the IL.

### 3.1. The Ionic Liquid / HOPG Interface

As a reference system, thin films of the IL  $[C_1C_1Im][Tf_2N]$  were deposited onto a HOPG single crystal. In contrast to previous studies on metal surfaces, the measurement of a macroscopic film, prepared ex-situ by spreading an IL droplet on the surface was not possible since the IL did not wet the surface; a typical situation is shown in the inset of Figure 3.1. The XP spectra of the resulting IL droplets, measured at  $0^\circ$ , are shown in Figure 3.1. The observation of the HOPG C 1s signal confirms that a significant fraction of the surface is not covered by the IL.

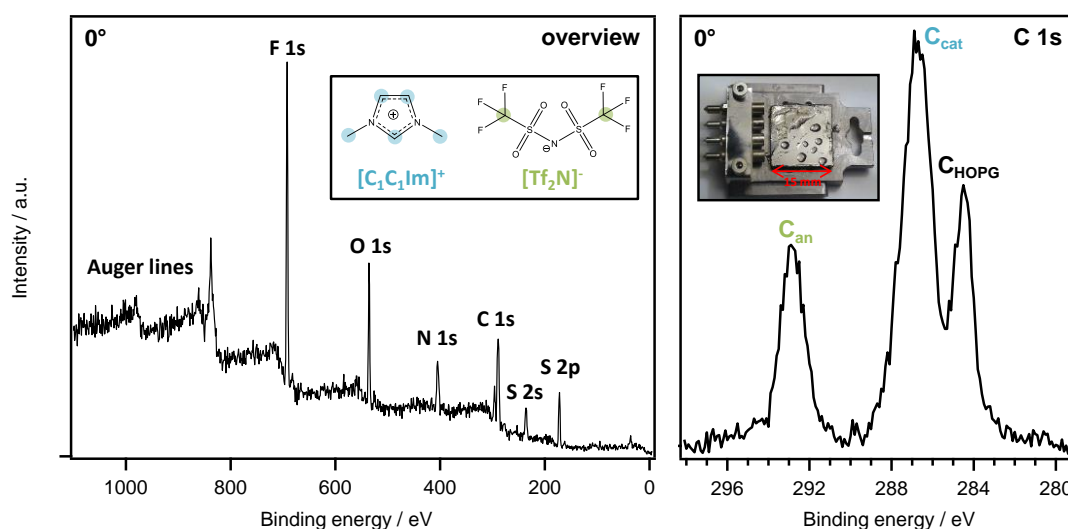


Figure 3.1: Overview and C 1s high resolution spectra of macroscopic  $[C_1C_1Im][Tf_2N]$  droplets on HOPG (ex-situ preparation). The spectra were measured at normal emission ( $0^\circ$ ). Sample position was optimized to obtain maximum IL signals in XPS. Besides all the expected IL signals, the HOPG C 1s signal is still visible.

#### 3.1.1. Growth Behavior

To gain a better understanding of the IL/HOPG interface, thin films of  $[C_1C_1Im][Tf_2N]$  were grown on HOPG by PVD and analyzed with XPS. Figure 3.2 shows the corresponding C 1s spectra at  $0^\circ$  (bulk sensitive) and at  $80^\circ$  (surface sensitive) against nominal IL layer thickness, which was calculated from the calibrated flux of the evaporator (see experimental section). With increasing exposure, that is nominal thickness, the HOPG substrate signal at 284.5 eV decreases, and the IL-derived peaks at 286.7 eV (cation) and 292.7 eV (anion)

increase in intensity, from top to bottom. In Figure 3.3a, the attenuation of the HOPG signal is plotted versus nominal thickness, and in Figure 3.3b the calculated thickness  $d$ , is shown, as obtained from equation 4.

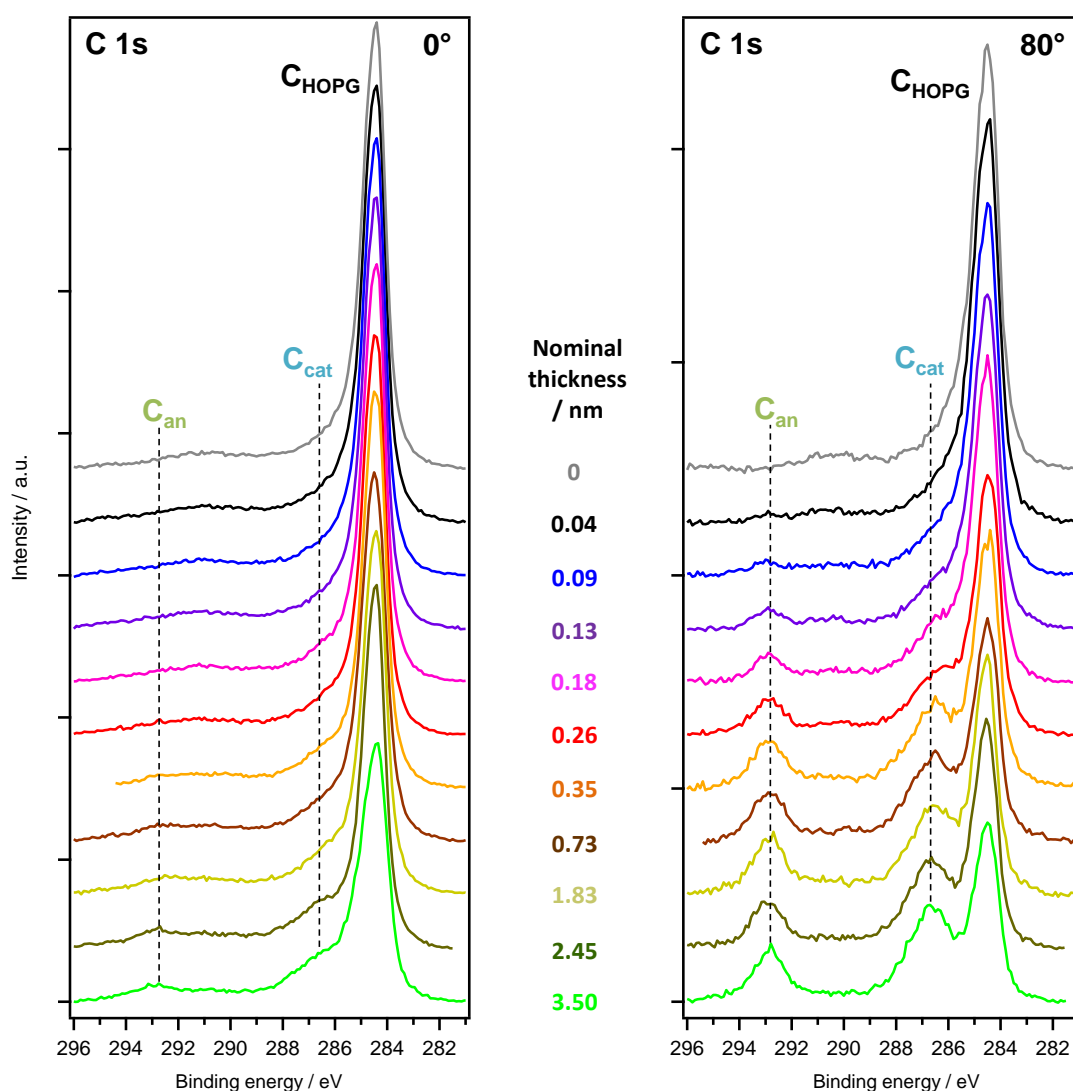


Figure 3.2: *C 1s* spectra of  $[C_1C_1Im][Tf_2N]$  films on HOPG, with increasing deposition time from top to bottom; collected at  $0^\circ$  (left) and  $80^\circ$  (right).

Initially, for both  $0^\circ$  and  $80^\circ$  the data points follow a linear behavior as expected for two dimensional growth (dashed lines). This behavior drastically changes when the nominal IL thickness exceeds a critical value of 0.35 nm, which corresponds to 0.5 ML. This coverage is consistent with a HOPG surface fully covered with cations and anions next to each other in a checkerboard-type structure. For nominal coverages of  $0.65 \text{ nm} < d < 1.5 \text{ nm}$ , the HOPG signal at  $80^\circ$  even increases despite of additional IL deposition. Consequently, the corresponding calculated thickness decreases for these coverages. From this behavior, it is concluded that the formation

of a second ion layer does not seem to be a favorable situation, and instead droplet formation on top of a thin wetting layer occurs. The deviations from the behavior expected for layer-by-layer growth in both measurement geometries, thus provide clear evidence for pronounced 3D growth for coverages exceeding 0.5 ML, in line with the observation of macroscopic droplets in the inset of Figure 3.1. The suggested growth mode of  $[C_1C_1Im][Tf_2N]$  on HOPG is depicted schematically in Figure 3.3c.

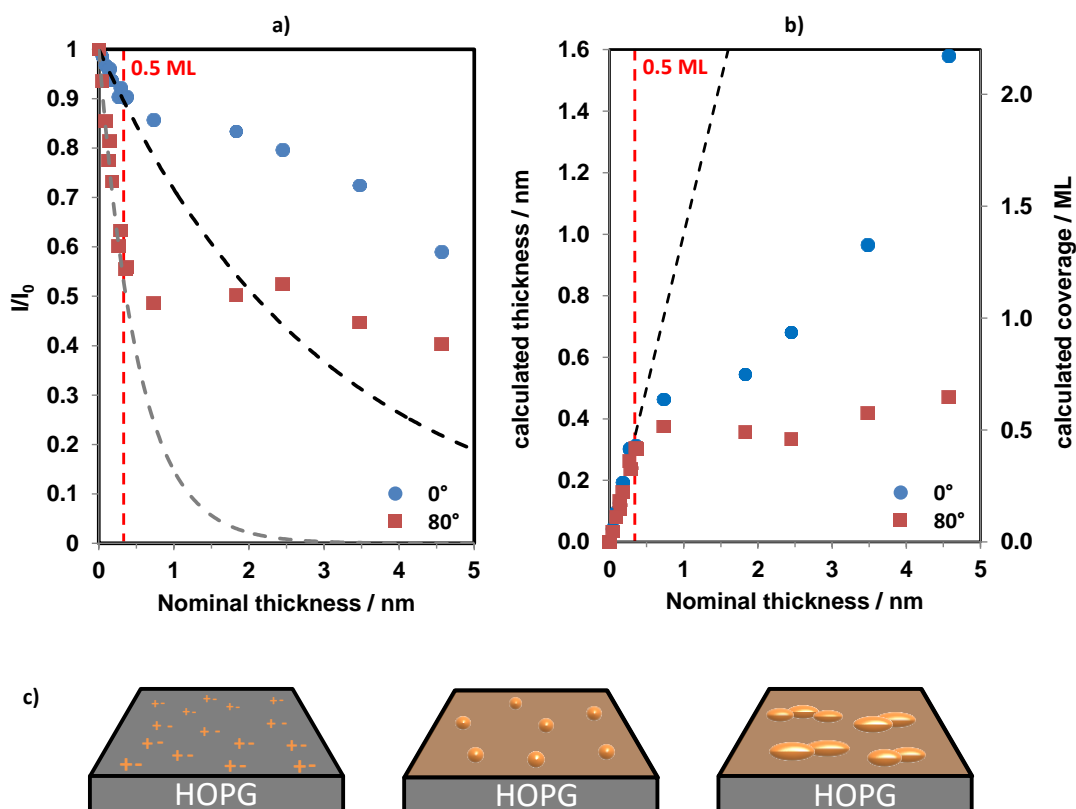


Figure 3.3: a) Attenuation of the C 1s substrate signal at  $0^\circ$  and  $80^\circ$  upon IL (data from Figure 3.2), compared to the expected attenuation for 2D layer-by-layer growth (dashed black and grey lines). b) Calculated mean thickness of the IL film as a function of nominal thickness as derived from the  $0^\circ$  and  $80^\circ$  data using equation 4, with  $\lambda(C\ 1s)=2.8\text{ nm}$ .<sup>95</sup> The strong deviations from the expected linear growth (dashed black line) are a clear indication for a 3D growth mode. c) Schematic drawing of the suggested growth mode of  $[C_1C_1Im][Tf_2N]$  on HOPG.

### 3.1.2. Initial Adsorption Behavior

Figure 3.4 shows the F 1s, O 1s and N 1s spectra of the thin IL films for increasing deposition time, at 0° (top) and 80° (bottom). The N 1s spectra are composed of two peaks, at ~399 and ~402 eV, which originate from the single N atom in the anion and the two N atoms in the cation, respectively. From the spectra in Figure 3.4 and from the quantitative analysis of the 80° data in Figure 3.5 (left), it is deduced that these two signals exhibit a 1 : 2 ratio (that is  $0.55 \pm 0.05$ ), independent of coverage. This value agrees very well with the nominal value of 0.5. From the fact that this value is observed also at the lowest coverages, it is concluded that both anions and cations are adsorbed next to each other on the surface, in a checkerboard structure (see Figure 3.3c). If anions were adsorbed on top of cations or vice versa, one of the two signals would be damped, leading to a deviation from the nominal ratio, as it was e.g. observed on Ni(111) at this coverage.<sup>47</sup> The quantitative analysis of the F 1s signal at 80° shows an enhancement at low coverages. This is evident from Figure 3.5 (right), where at 80° an F 1s : N 1s (total signal) ratio of ~4 is observed, which is to be compared to the nominal ratio of 2 (6 F atoms versus 3 N atoms). It is thus concluded that adsorption of the anion preferentially occurs with the oxygen atoms being in contact with the HOPG substrate and the CF<sub>3</sub> groups pointing towards vacuum. This strong enhancement is found up to a nominal thickness of 0.35 nm, that is 0.5 ML IL, and slowly decreases at higher nominal thicknesses. This behavior can be interpreted as further evidence for the formation of IL droplets, as the random orientation of the IL ions within the droplets counteracts the preferential orientation of the initially adsorbed ions in direct contact to the HOPG substrate. The F 1s / N 1s ratio remains higher than the ratio of a macroscopic IL film up to a nominal thickness of ~5 nm. This behavior is in line with the pronounced formation of IL islands or droplets on top of a thin wetting layer. However, at this point, from the XPS data it cannot be ruled out that the initial wetting layer breaks apart upon formation of the larger droplets.

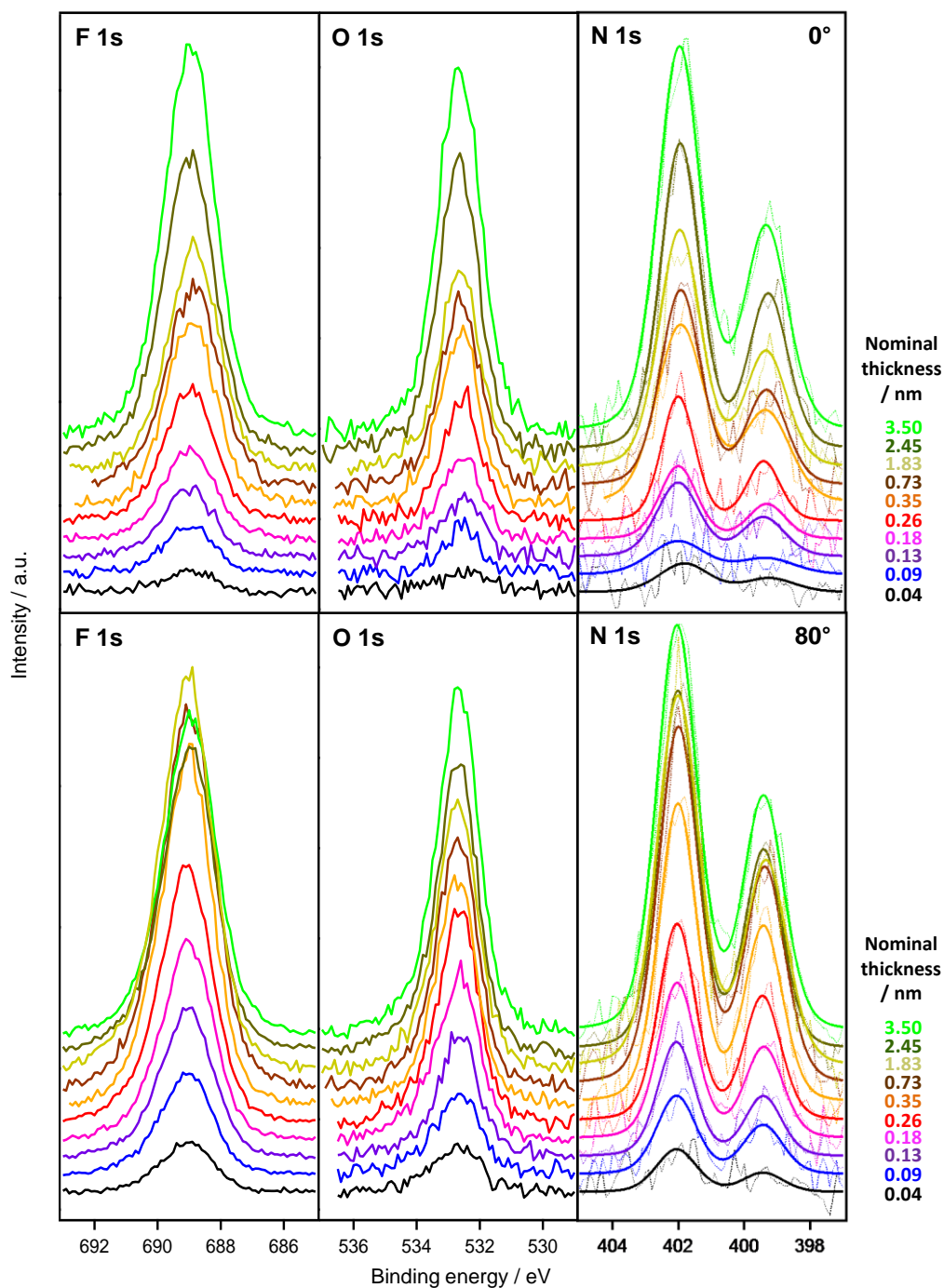


Figure 3.4: IL-related signals for  $[C_1C_1Im][Tf_2N]$  films on HOPG with increasing nominal thickness; collected at  $0^\circ$  (top) and  $80^\circ$  (bottom).

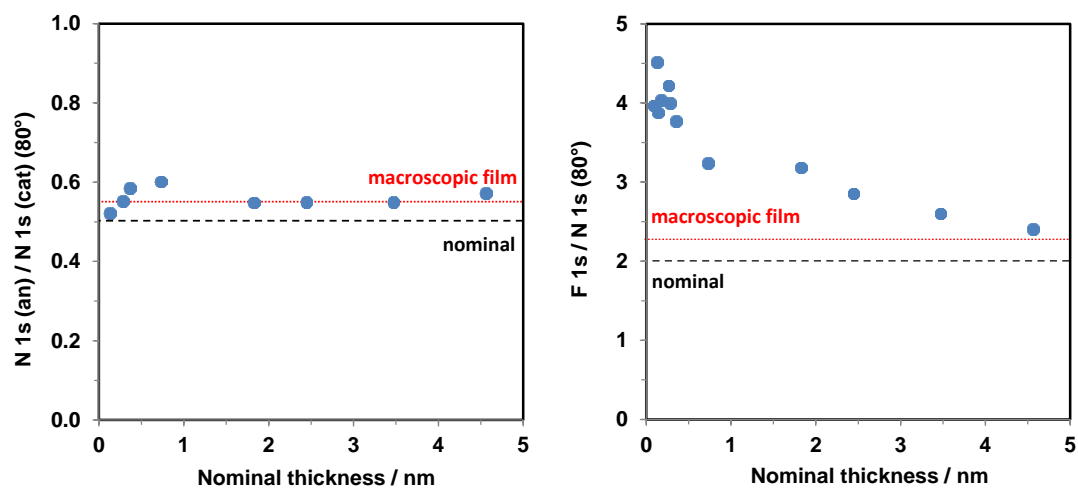


Figure 3.5:  $N_{an} / N_{cat}$  ratio (left) and  $F\ 1s / N\ 1s$  ratio (right) for  $[C_1C_1Im][Tf_2N]$  films on HOPG with increasing IL coverage; for the data from Figure 3.4 collected at  $80^\circ$ . The nominal ratios are indicated as black dashed lines, the value observed for thick macroscopic films as red dotted lines.

## 3.2. The Ionic Liquid / Graphene Interface

### 3.2.1. Graphene Growth

Graphene was prepared on Ni(111) by CVD using butene gas. The graphene coverage was controlled by varying crystal temperature and nucleation time (see experimental section). The IL growth behavior will be discussed for a partial and a full layer of graphene, that is, for 0.6 and 1.0 layers of graphene. The coverage calibration was done by two different methods, which yielded consistent results within the margin of error. In the first, the attenuation of the Ni 2p substrate signal was used and in the second, the graphene C 1s signal was calibrated by comparison to the C 1s signal of a saturated benzene layer on Ni(111), which corresponds to a  $(\sqrt{7} \times \sqrt{7})R19.1^\circ$  structure with a benzene coverage of 0.143 ML, that is, to a carbon coverage of 0.86 ML.<sup>112</sup> Figure 3.6 shows the  $0^\circ$  Ni 2p and C 1s spectra of clean Ni(111), Ni(111) covered with 0.6 and 1.0 layers of graphene, and the benzene/Ni(111) reference spectrum. The graphene C 1s BE was  $285.0 \pm 0.1$  eV, in agreement with previous studies.<sup>113</sup> Note that with the given energy resolution of 0.9 eV the bridge-top and top-fcc graphene adsorption geometries<sup>113</sup> cannot be resolved.

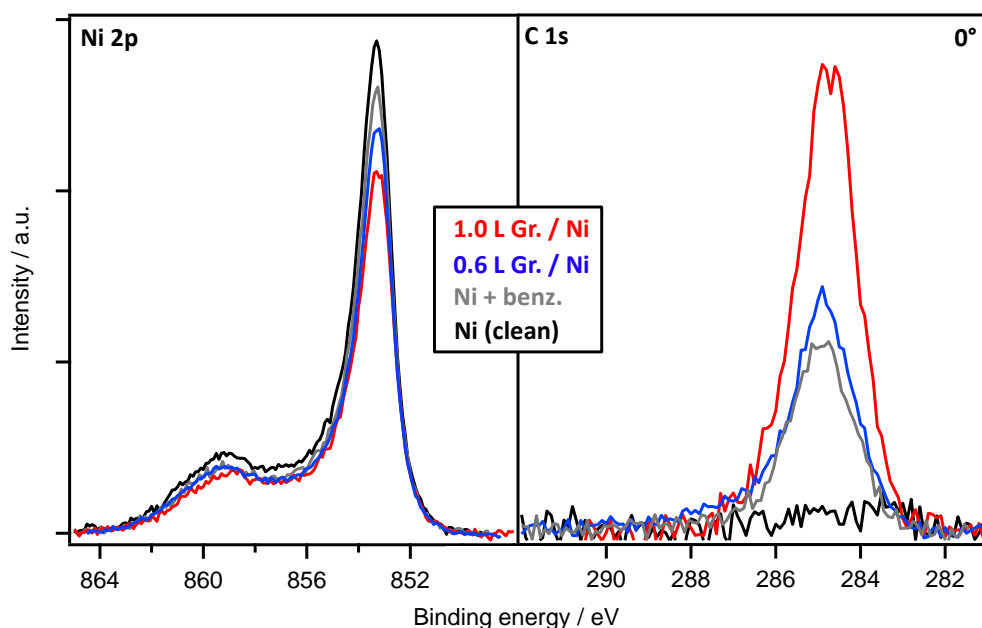


Figure 3.6: Ni 2p and C 1s spectra of clean Ni(111) and graphene / Ni(111) with graphene coverages of 0.6 and 1.0 layers; collected at  $0^\circ$ .

### 3.2.2. Adsorption and Growth on Nickel-Supported Graphene

In Figure 3.7, 0 and 80° C 1s spectra of  $[C_1C_1Im][Tf_2N]$  films deposited onto the two different graphene/Ni(111) samples are depicted as a function of increasing IL coverage. The spectra show that for comparable amounts (indicated by the same colors) of deposited IL, pronounced intensity differences of the IL signals and of the damping of the graphene signals are found for the two substrates differing in their graphene coverage.

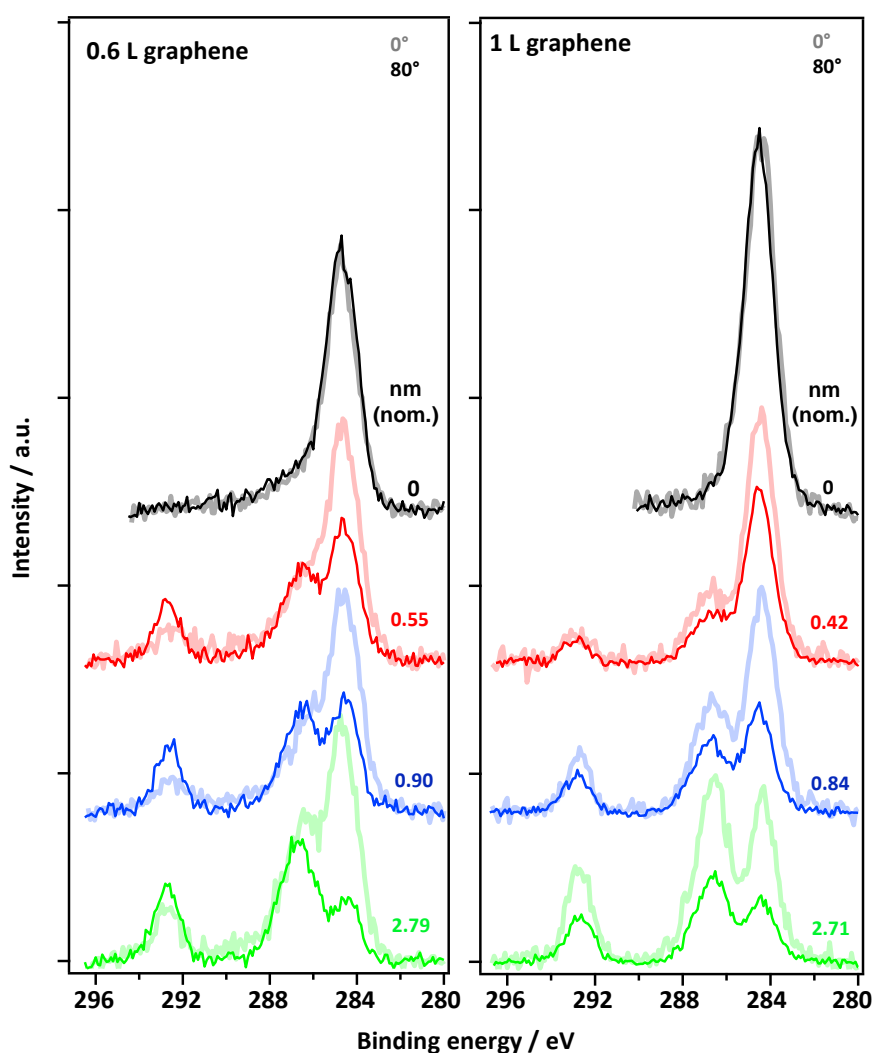


Figure 3.7: 0° (light colors) and 80° (dark colors) C 1s spectra of  $[C_1C_1Im][Tf_2N]$  thin films deposited on graphene / Ni(111). Graphene coverage (in layers) is given in the top left corner. Nominal IL film thickness (in nm) is given on the right hand side of each diagram.

Starting with the situation for 1 layer graphene on Ni(111), a different behavior compared to HOPG is observed. While on HOPG the behavior expected for 2D IL growth (indicated as dashed lines in Figure 3.8a and Figure 3.8b) is only found up

to a nominal IL thickness of  $\sim 0.35$  nm (0.5 ML IL), for 1 layer graphene this behavior is found up to 0.70 nm, that is, 1 ML IL. The attenuation of the Ni 2p substrate signal (Figure 3.8a) and the C 1s graphene signal (Figure 3.8b) shows the same behavior (note that due to the lower IMFP, Ni 2p signals is stronger attenuated than the C 1s signal). At IL coverages above 0.70 nm, the graphene C 1s signal and the Ni 2p signal decay slower than expected for layer-by-layer growth. It is therefore concluded that at an IL coverage of 1 ML a homogeneous wetting layer is formed with the height of one ion pair, and that at higher coverages 3D islands are formed on top of the wetting layer, indicating a Stranski-Krastanov-type growth mode. One reason for the different wetting and growth behaviors of the IL on graphene/Ni(111) compared to the IL growth on HOPG might be the so-called wetting transparency of graphene as introduced by Rafiee et al. They studied the contact angle of water (CAW) with Cu as well as with Cu-supported single- and few-layer graphene.<sup>114</sup> CAW measured for single-layer graphene/Cu was found to be almost identical to that for bare Cu. With an increasing number of graphene layers, the initial CAW on copper gradually increased, approaching the value on bulk graphite at around six graphene layers. This behavior was explained by considering long-range van der Waals forces between the adsorbed water molecules and the underlying C and Cu substrate atoms. For each graphene layer inserted, the initial interaction of water with Cu is gradually replaced by interaction with C.<sup>114</sup> The same situation is likely to account for the IL/1 ML graphene/Ni(111) results: in contrast to IL on HOPG where the IL interacts only with underlying carbon, the IL on 1 ML graphene/Ni(111) is able to interact with both graphene carbon and Ni atoms; for the latter, a Stranski-Krastanov growth mode also occurs.<sup>47</sup>

At low coverages onto the 1 layer graphene/Ni(111) sample, the quantitative analysis of the N 1s signals at  $80^\circ$  yields the stoichiometric  $N_{\text{cat}} : N_{\text{an}}$  ratio of 2 : 1, similar to the initial adsorption of  $[\text{C}_1\text{C}_1\text{Im}][\text{Tf}_2\text{N}]$  on HOPG; thus, it is concluded that anions and cations initially adsorb next to each other, in direct contact with the surface. Note that this arrangement is similar to that found on Au(111),<sup>46</sup> but differs from that on the bare Ni(111) surface, where at this coverage a sandwich-like structure with the anions on top of the cations is formed.<sup>47</sup> The fact that the observed behavior on 1 layer graphene follows the dashed line up to 0.70 nm suggests that – in contrast to HOPG – also a second (half) layer grows 2D-like on top of the first

half-layer, most likely anions on top of cations and cations on top of anions, yielding a total coverage of 1 ML. The proposed arrangement at low coverage is also supported by the enrichment of the F 1s signal in the surface sensitive  $80^\circ$  geometry, which again indicates preferential adsorption of the anion with its  $\text{CF}_3$  groups pointing towards vacuum (data not shown). The fact that this enrichment effect is less pronounced than on HOPG is probably due to the fact that the formation of the second half layer partly already starts before completion of the first half layer.

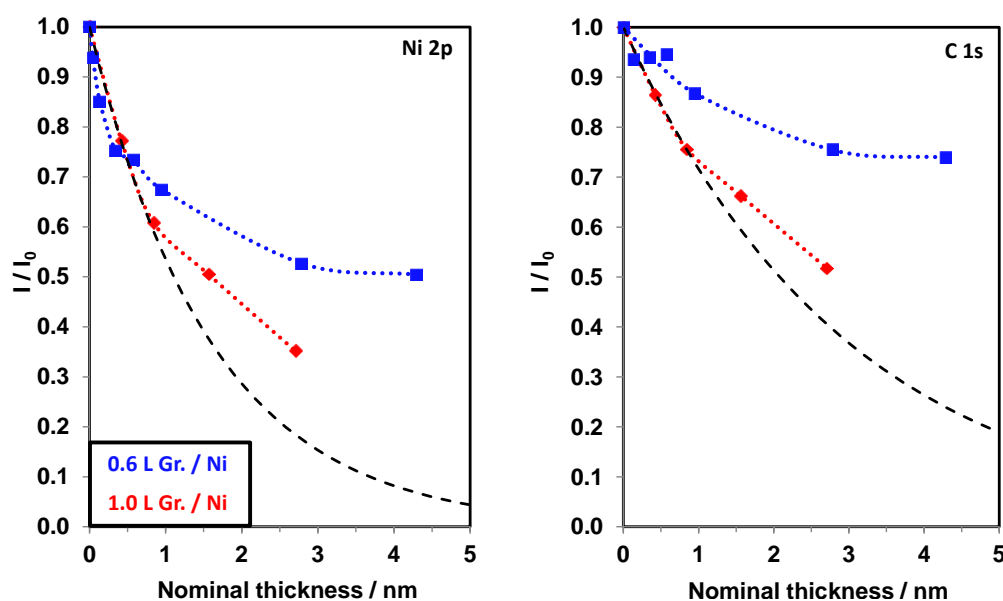


Figure 3.8: Attenuation of the Ni 2p and the C 1s substrate signals upon IL deposition in  $0^\circ$  emission compared to the expected theoretical attenuation for 2D layer-by-layer growth (dashed lines).

Next the data for 0.6 layers graphene on Ni(111) is analyzed. The data in Figure 3.8 show that at  $0^\circ$  the initial attenuation of the Ni 2p and graphene C 1s signal at 285 eV upon IL deposition (until 0.3 – 0.4 nm) is much more pronounced than the attenuation of the graphene C 1s signal (which remains nearly unchanged), and even stronger than expected for uniform 2D growth. This behavior indicates preferential IL adsorption on the (stronger damped) Ni regions, which results from diffusion of the IL from the graphene-covered regions to the Ni regions, which is possible due to the high mobility of the IL on graphene. In a previous study, it was shown that on Ni(111),  $[\text{C}_1\text{C}_1\text{Im}][\text{Tf}_2\text{N}]$  initially adsorbs in a sandwich like configuration, i.e. with the anions on top of the cations.<sup>47</sup> From the strong enhancement of the N 1s and C 1s anion signals at  $80^\circ$  emission for low nominal

[C<sub>1</sub>C<sub>1</sub>Im][Tf<sub>2</sub>N] coverages (cf. Figures 3.9a and 3.9b), it is concluded that on 0.6 layers graphene / Ni(111) the same configuration is also found on the bare Ni regions. In line with this interpretation, at low IL coverages, the cation-related N 1s peaks are found to be shifted towards lower BE by  $\sim -0.2$  eV (Figure 3.9c, blue), as also observed for IL deposition onto the bare Ni crystal (dashed black line); in contrast, on 1 layer graphene, they are shifted towards higher BE by  $\sim +0.2$  eV (red). These findings strongly suggest that for graphene coverages below a full layer, the adsorption of the IL preferentially occurs on bare Ni surface areas.

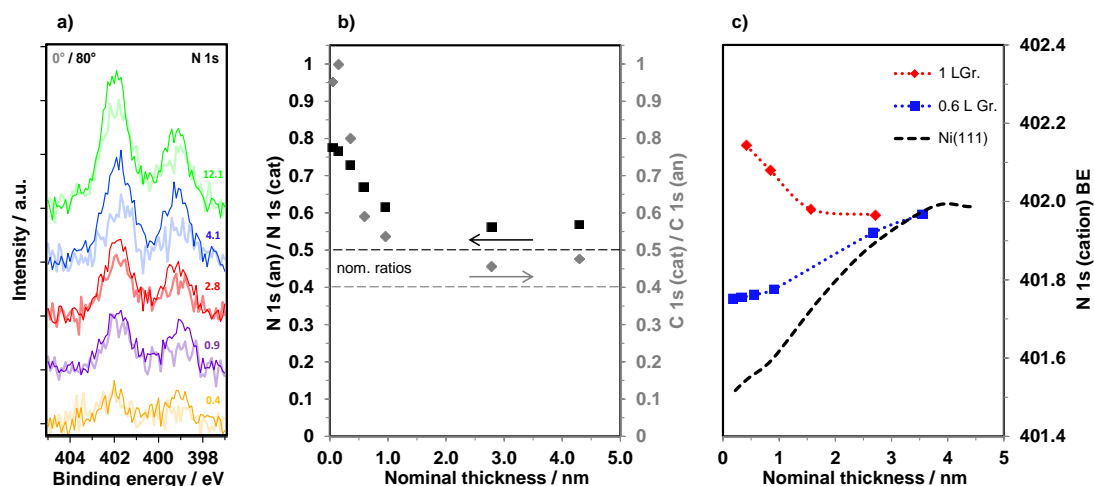


Figure 3.9: a) 0 and 80° high resolution N 1s spectra of [C<sub>1</sub>C<sub>1</sub>Im][Tf<sub>2</sub>N] films on 0.6 L graphene / Ni(111) with increasing IL coverage. b) 80° N<sub>cat</sub> / N<sub>an</sub> and C<sub>cat</sub> / C<sub>an</sub> ratios with increasing IL coverage. c) N 1s (cation) BE with increasing IL coverage.

For prolonged deposition times, the reduced attenuation of the Ni 2p and graphene C 1s signals is a clear evidence for 3D growth on both the graphene-covered regions and the graphene-uncovered regions. Interestingly, for larger IL coverages ( $> 1$  nm) the substrate attenuation for 0.6 layers graphene (blue lines in Figure 3.8) is weaker than for 1.0 layer graphene (red lines) and also than on Ni(111) (see ref.<sup>47</sup>). This indicates more pronounced 3D growth on the surface with a fractional graphene layer, which could be due to pinning of large islands at step edges.

### 3.3. Summary and Conclusions

Thin films of the IL [C<sub>1</sub>C<sub>1</sub>Im][Tf<sub>2</sub>N] were thermally deposited onto different carbonaceous supports, namely HOPG and Ni(111)-supported graphene with two

---

different graphene coverages, that is, 0.6 and 1.0 layers. These studies show that the initial adsorption behavior and growth strongly depend on the substrate and that even between HOPG and a single graphene layer on Ni(111) significant differences exist. On HOPG, the formation of a thin wetting layer with cations and anions next to each other occurs, with a coverage of 0.5 ML. On top of this wetting layer, further IL deposition leads to pronounced growth of 3D islands; it cannot be ruled out that the 0.5 ML IL wetting layer even breaks apart upon further IL deposition. On 1 layer graphene / Ni(111) again a wetting layer is formed; however, the thickness of this stable layer is twice the thickness on HOPG, and most likely consists of neighboring ion pairs with anions on top of cations and cations on top of anions in a checkerboard configuration, yielding a total coverage of 1 ML. On top of this wetting layer, 3D growth is less pronounced than on HOPG. On a fractional graphene layer, that is 0.6 layers graphene / Ni(111), IL adsorption preferentially occurs on bare Ni surface areas, with an arrangement as on a bare Ni(111) surface. The preferential adsorption causes more pronounced 3D growth compared to the fully graphene-covered Ni(111) surface.



## 4. The Ionic Liquid / Metal Interface

A profound knowledge of IL/metal interfaces is of pivotal interest for present and future applications of ILs, including lubrications,<sup>115, 116</sup> electrical energy devices,<sup>117, 118</sup> and catalysis.<sup>119, 120</sup> Different techniques have been applied for the investigation of the IL/metal interface, for some of which the interface is accessible through a macroscopic IL layer, such as SFG,<sup>38, 121</sup> STM,<sup>40-42, 122</sup> or AFM<sup>41, 43, 122</sup>. For surface sensitive methods like XPS,<sup>46, 47</sup> ultrathin films are required.

In this chapter, the influence of physicochemical properties of different ILs on the adsorption and growth behavior of respective ultrathin IL films will be discussed. For best comparability, all investigated ILs – [C<sub>8</sub>C<sub>1</sub>Im][Tf<sub>2</sub>N], [C<sub>8</sub>C<sub>1</sub>Im]Cl, [C<sub>2</sub>C<sub>1</sub>Im][EtOSO<sub>3</sub>], and [C<sub>2</sub>C<sub>1</sub>Im][Otf] – were deposited onto a Au(111) single crystal by means of IL-PVD or IL-ESID, a technique applied for the first time within the scope of this work. After having shown that ESID allows for the deposition of ultrathin IL films with the same quality as PVD deposited films, in subsequent experiments, both methods were applied alternatively. In a similar manner to the discussion on the IL/carbon interface in chapter 3, the main focus will lie on the initial adsorption geometry of IL ions, surface wetting and subsequent IL growth behavior, as well as on electronic interactions between the IL and the Au substrate. Moreover, changes concerning the IL wetting and growth behavior on a carbon contaminated, as well as on a Pd-modified Au(111) surface were investigated.

## 4.1. Introducing Electrospray Ionization Deposition of Ionic Liquids

The content of this chapter is based on the following publication:<sup>56</sup>

*Electrospray Ionization Deposition of Ultrathin Ionic Liquid Films: [C<sub>8</sub>C<sub>1</sub>Im]Cl and [C<sub>8</sub>C<sub>1</sub>Im][Tf<sub>2</sub>N] on Au(111)*, Florian Rietzler, Marius Piermaier, Alexey Deyko, Hans-Peter Steinrück, and Florian Maier, *Langmuir*, 2014, **30** (4), 1063–1071.

PVD is limited to thermally stable ILs, which evaporate at elevated temperatures as intact ion pairs at a sufficient rate before thermal decomposition processes take place. In order to overcome this material limitation, during the work on this thesis, an alternative technique, namely, ionic liquid electrospray ionization deposition (IL-ESID) was established. IL-ESID is suitable to deposit even thermally very unstable ILs onto any surface under UHV. The general ESI process is depicted in Figure 4.1. An easily evaporable solvent contains the dissolved target molecules (which in case of IL-ESID are IL cations and anions). The solution is transported to the emitter capillary, which is set on high voltage (HV) with respect to the opposite entrance orifice, e.g., +2 kV vs the grounded entrance. Due to the high electric field strength at the capillary tip, the leaking droplets become positively charged (in the case of positive bias voltage). Charging occurs either by spontaneous ionization of neutral molecules via protonation/deprotonation equilibria or, for dissolved ions, by directed diffusion of these ions along the electric field lines within the tip droplets.<sup>123, 124</sup> Repulsive Coulomb forces of the charged solution droplets lead to formation of a so-called Taylor cone at the capillary's tip.<sup>125-127</sup> At the point when surface tension can no longer compensate for the repulsive forces,<sup>128</sup> droplets are emitted from the cone and, due to the applied potential difference, are accelerated toward the opposed entrance orifice into the vacuum chamber. Evaporation of volatile solvent molecules in vacuo increases the droplet's charge density. When the surface tension again no longer compensates for the repulsive Coulomb forces, that is, when reaching the so-called Rayleigh limit, the initial droplets explode under formation of several smaller offspring droplets; this process is also known as Coulomb explosion. The droplet diminution process ideally proceeds down to the

stage of solvent-free small molecular clusters and even single molecules / ion pairs on their way to a spectrometer in the case of ESI mass spectrometry (ESI-MS) or to a substrate for thin film preparation in the case of ESID.

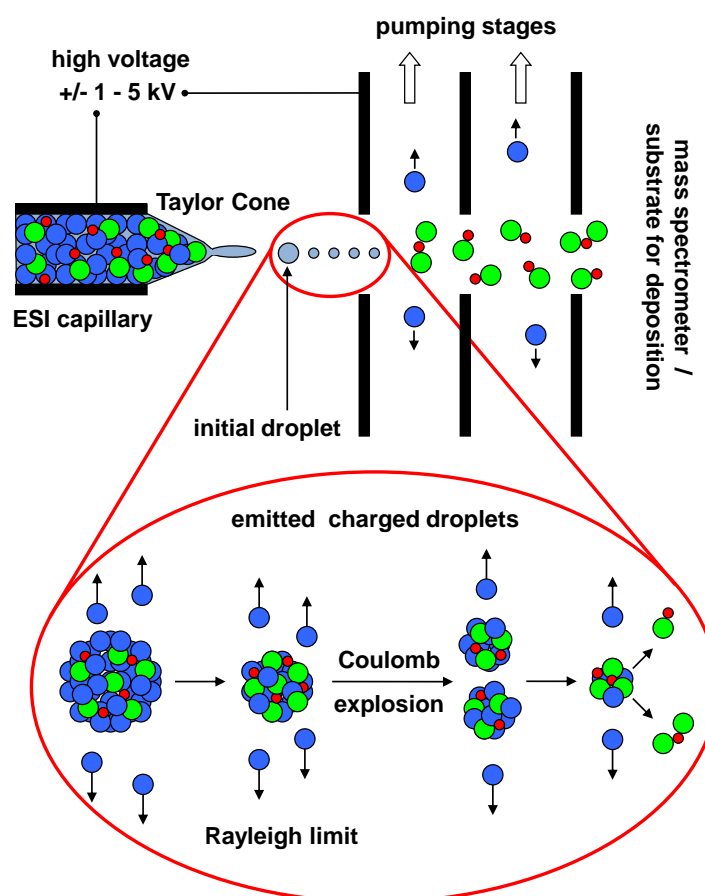


Figure 4.1: Schematic illustration of the general ESI process. Depending on bias polarity, a (slight) excess of positively or negatively charged species is present.

Initially, the ESI technique was mainly refined in combination with MS methods.<sup>129, 130</sup> More recently, ESI has been used for the deposition of thin films and clusters of both, inorganic<sup>131, 132</sup> and organic substances, particularly for the deposition of polymeric films.<sup>133-137</sup> The morphology of polymeric films was found to be dependent on numerous factors, including the type of solvent, concentration, flow rate, conductivity of the solution, temperature, viscosity, and surface energy.<sup>138</sup> Due to their ionic nature, ILs are supposed to be perfect candidates for ESID.

Generally, evaporation of ILs results in the formation of neutral ion pairs in the gas phase.<sup>139, 140</sup> Thus, IL-PVD thin films always consist of an equal amount of cations and anions. For IL-ESID, the situation is expected to be different due to the emission of charged droplets by field-induced preferential diffusion of cations (in

case of positive tip bias) or anions (in case of negative bias) towards the tip surface. Accordingly, ESI-MS studies revealed the cation/anion ratio of an IL electrospray to be  $\neq 1$ . For positive potentials, the clusters detected by MS contain an excess positive charge and possess the general composition  $C_nA_{(n-1)}$ , with C and A being the cations and anions, respectively. Accordingly, in negative mode clusters with the general composition  $C_{(n-1)}A_{(n)}$  are observed.<sup>141-143</sup> An important factor concerning the amount of charge within the molecular clusters is the initial size of the droplets that are emitted from the Taylor cone.<sup>144</sup> With increasing droplet size the relative amount of excess charge carriers decreases. The initial droplet size in turn increases with increasing needle orifice and flow rate, and with decreasing conductivity of the ESI solution.<sup>124</sup> For ESI emitters with wide orifices and for high flow rates, the initial droplet sizes are in the  $\mu\text{m}$  range.<sup>144</sup> Juraschek *et al.* studied the electrospray composition of NaCl water/methanol solutions via trap mass spectrometry. For a  $10^{-2}$  M solution at a flow rate of  $180 \mu\text{L/h}$ , they detected only one additional  $\text{Na}^+$  cation per 250 neutral ion pairs.<sup>144</sup> Similar concentrations and flux rates were employed in the IL-ESID experiments shown in this work; the absence of significant deviations from the IL anion : cation = 1 : 1 stoichiometry would thus imply the emission of large initial droplets in the ESI process with most of the IL being present as neutral clusters or even as single ion pairs.

First, the suitability of IL-ESID for the preparation of homogeneous IL thin films was evaluated. For this reason, the first IL-ESID experiments were performed on a well-understood system: thin films of the IL  $[\text{C}_8\text{C}_1\text{Im}][\text{Tf}_2\text{N}]$  were deposited onto a Au(111) surface and analyzed by ARXPS. These results are compared with a previous study in which PVD was used for thin film preparation of the same IL on Au(111). In the second part of this chapter, ESI-deposited thin films of a thermally unstable IL were investigated, namely  $[\text{C}_8\text{C}_1\text{Im}]\text{Cl}$  on Au(111).

#### 4.1.1. Proof of Principle: $[\text{C}_8\text{C}_1\text{Im}][\text{Tf}_2\text{N}]$ on Au(111)

As pointed out in the introduction to this chapter, well-defined ultrathin films of the IL  $[\text{C}_8\text{C}_1\text{Im}][\text{Tf}_2\text{N}]$  were previously grown on a Au(111) surface by means of PVD and analyzed by ARXPS.<sup>46</sup> This study clearly revealed that within the first nanometers,  $[\text{C}_8\text{C}_1\text{Im}][\text{Tf}_2\text{N}]$  grows in a layer-by-layer mode in checkerboard

configuration. For the first closed molecular layer (corresponding to a coverage of 0.5 ML according to the ML definition applied in this work), the ionic head groups are in direct contact with the gold surface, whereas the octyl chains are oriented towards the vacuum side. Since these PVD prepared  $[\text{C}_8\text{C}_1\text{Im}][\text{Tf}_2\text{N}]$  films on Au(111) represent a well understood system, this particular solid/IL interface was taken to check the general suitability of ESID for the preparation of ultrathin IL films.

### Adsorption Behavior

In Figure 4.2 the C 1s and N 1s spectra of ultrathin ESID prepared  $[\text{C}_8\text{C}_1\text{Im}][\text{Tf}_2\text{N}]$  films with coverages of 0.4, 0.7 and 1.2 ML are depicted, for an emission angle of  $80^\circ$ . For comparison, spectra of PVD-prepared films with similar coverages are also shown. The ESID (black) and PVD (grey) curves are virtually identical for the same coverage and detection angle. This is a clear indication that the IL-ESID films have the same properties as the thermally deposited IL films. Note that the corresponding deposition times were very different for the two different techniques: Whereas the deposition of the 1.2 ML film by PVD took about five minutes, the deposition of the same coverage by ESID took more than two hours demonstrating that ESID is a very time-consuming procedure.

In the C 1s region, three different carbon species can be distinguished. In the following, BE values for the thickest films are given: The peak at 287.4 eV (“C<sub>hetero</sub>”) is assigned to the five carbon atoms bound to the imidazolium nitrogen atoms, in line with previous publications.<sup>25, 45, 46, 145, 146</sup> The peak at 285.6 eV (“C<sub>alkyl</sub>”) is attributed to the seven alkyl carbon atoms of the cation that are not bound to nitrogen. The well separated peak at 293.6 eV (“C<sub>anion</sub>”) is due to the CF<sub>3</sub> groups of the anion. In the N 1s region, the peak at 400.1 eV (“N<sub>anion</sub>”) stems from the imide nitrogen of the anion, and the peak at 402.7 eV (“N<sub>cation</sub>”) from the two equivalent nitrogen atoms in the imidazolium ring of the cation. XPS signals are also observed for all other IL-related atoms, i.e. O, S and F; they also show no differences for the two preparation methods, and thus will not be discussed in the following.

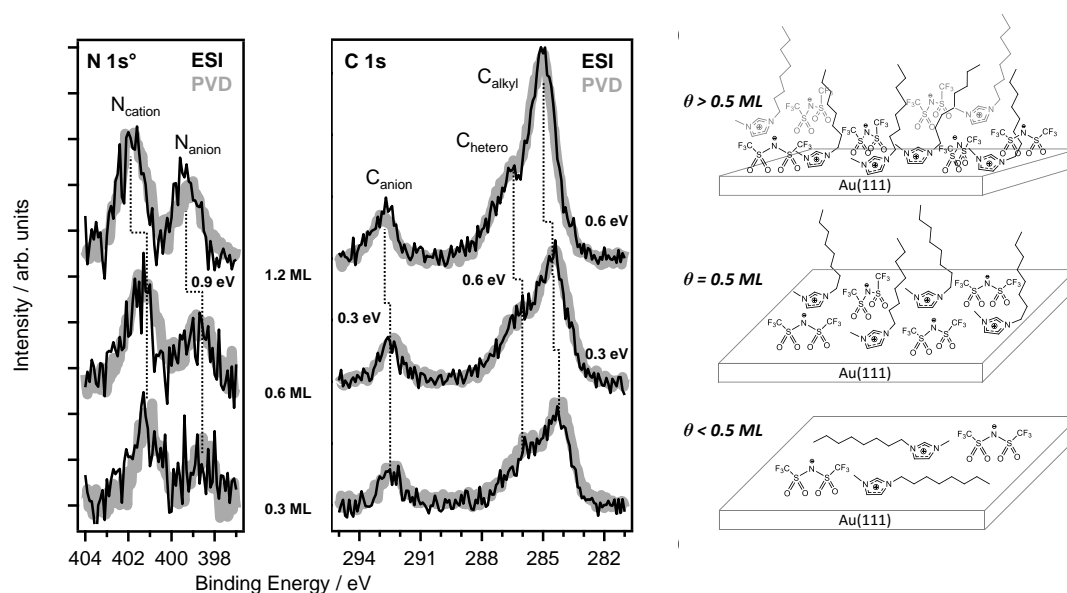


Figure 4.2: Direct comparison of 80° N 1s (left) and C 1s (middle) XPS spectra of [C<sub>8</sub>C<sub>1</sub>Im][Tf<sub>2</sub>N] thin films prepared via ESID (black curves) and PVD (gray curves). Scheme for preferential orientation of adsorbed ions at the interface of [C<sub>8</sub>C<sub>1</sub>Im][Tf<sub>2</sub>N] as a function of coverage (right); adapted from reference <sup>46</sup>.

With increasing coverage, the IL peaks shift to higher BE, in line with a previous study of the PVD films of [C<sub>8</sub>C<sub>1</sub>Im][Tf<sub>2</sub>N] on Au(111).<sup>46</sup> The differential shift of the C<sub>alkyl</sub> peak within the first 0.5 ML (= one complete layer of single ions for the checkerboard arrangement) by 0.3 eV in Figure 4.2 is explained by a preferential orientation of the initially flat-lying octyl chains towards vacuum in order to allow further ion pairs to adsorb directly on the gold surface. This change in adsorption geometry is energetically favored due to stronger substrate interactions of the polar headgroups compared to the non-polar octyl chains. The orientation of the octyl chains towards vacuum is also reflected in a relative increase of C<sub>alkyl</sub> signal at 80°, i.e. in the surface sensitive geometry.

In line with earlier findings,<sup>46</sup> the initial adsorption behavior of [C<sub>8</sub>C<sub>1</sub>Im][Tf<sub>2</sub>N] prepared by ESID on Au(111) can be summarized as follows: The imidazolium ring of the cation adsorbs parallel on the Au surface with the octyl chains preferentially pointing towards vacuum. The anion is adsorbed to the gold surface in a cis-configuration preferentially via the oxygen atoms of its SO<sub>2</sub> groups and the CF<sub>3</sub> groups are pointing towards vacuum.

## Stoichiometry

As next step, the stoichiometry of the deposited films was analyzed. This is necessary, since a small excess of cations is expected due the positively biased emitter capillary. Table 4.1 shows the  $N_{\text{anion}}/N_{\text{cation}}$  ratio, as determined from the N 1s spectra at  $0^\circ$  and  $80^\circ$ . The comparison of these two signals allows for the most accurate determination of the actual stoichiometry, as both are measured in the same spectrum. Thus, no calibration has to be performed, that is, the ratios are neither influenced by errors in the atomic sensitivity factors nor by the attenuation length due to kinetic energy-dependent IMFPs of different core level electrons. Moreover, according to the adsorption geometry, the nitrogen atom of the anion is located only slightly above the nitrogen atoms of the cation. Consequently, the measured  $N_{\text{anion}}/N_{\text{cation}}$  ratio is not significantly affected by the different surface sensitivities given by the emission angles. The analysis of the data in table 4.1 shows that within the margin of error of about  $\pm 5\%$ , the determined ratio perfectly agrees with the nominal value of 0.5. Hence, in spite of carrying out IL-ESID in positive mode, there is no indication for a preferential deposition of cations. The quantitative analysis of all IL related signals also showed no deviations exceeding the margin of error ( $\pm 10\%$ ; due to the uncertainties mentioned above).

Coverage ML	$N_{\text{anion}} / N_{\text{cation}}$	
	$0^\circ$	$80^\circ$
0.4	0.53	0.51
0.7	0.48	0.53
1.2	0.48	0.53
2.1	0.48	0.53
4.0	0.50	0.53
6.8	0.49	0.48
$\infty$	0.51	0.53
<b>nominal</b>	<b>0.50</b>	<b>0.50</b>

Table 4.1:  $N_{\text{anion}}/N_{\text{cation}}$  ratios for ESI deposited  $[C_8C_1Im][Tf_2N]$  films on Au(111) in comparison with a macroscopic IL film and the nominal value.

---

## Growth Mode

In order to gain insight into the growth mode of adsorbates via ARXPS, the attenuation of a substrate signal is monitored as function of coverage, at different detection angles. For Au(111), the intense Au 4f peak is best suited for such an analysis: Cremer and co-workers deduced 2D layer-by-layer (Frank-van-der-Merwe) growth of ultrathin PVD-prepared  $[\text{C}_8\text{C}_1\text{Im}][\text{Tf}_2\text{N}]$  films on Au(111) from the attenuation behavior of the Au 4f signals, at  $0^\circ$  and  $80^\circ$ , as a function of deposition time.<sup>46</sup> Due to the problems to maintain a constant ESI beam flux (see experimental section for details), the correlation of substrate attenuation with time is, however, not reliable for the ESI-deposited films. Nevertheless, detailed information on the growth mode can be derived by the following analysis:<sup>94</sup> In Figure 4.3, the Au 4f intensity at  $0^\circ$  and  $80^\circ$  is plotted against nominal coverage (calculated from the  $0^\circ$  data using equation 4 with  $\lambda = 3$  nm for the Au 4f photoelectrons ( $E_{\text{kin}} \approx 1400$  eV)<sup>95</sup> for the ESID-films (full symbols), and also for the PVD-films studied by Cremer et al.<sup>46</sup> (open symbols). Both data sets agree very well with each other, indicating again that with ESID identical layers are prepared as with PVD. The higher surface sensitivity of the  $80^\circ$  geometry is reflected in a much faster attenuation of the Au 4f peak. The dashed line in Figure 4.3 represents the attenuation predicted at  $80^\circ$  according to equation 4 for layer-by-layer growth. For both preparation routes, the measured  $80^\circ$  data correlates very well with this curve, which verifies layer-by-layer film growth for  $[\text{C}_8\text{C}_1\text{Im}][\text{Tf}_2\text{N}]$  films on Au(111). The ARXPS analysis therefore unequivocally demonstrates that ESID is a suitable route for the preparation of  $[\text{C}_8\text{C}_1\text{Im}][\text{Tf}_2\text{N}]$  thin films on Au(111).

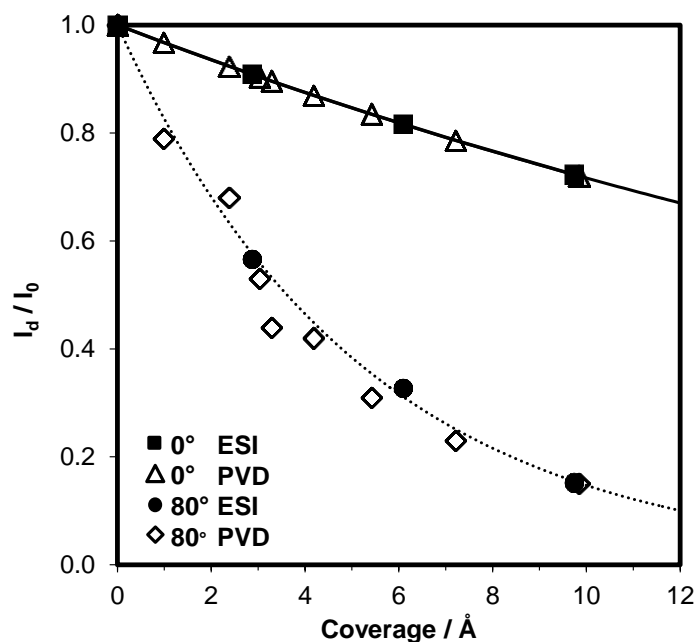


Figure 4.3: Attenuation of the Au 4f substrate intensity  $I_d$  as a function of coverage  $d$  for  $[\text{C}_8\text{C}_1\text{Im}][\text{Tf}_2\text{N}]$  films deposited by PVD (hollow triangles and diamonds) and ESI (solid squares and circles), respectively, at emission angles of  $0^\circ$  and  $80^\circ$ . The dotted line is calculated from the  $0^\circ$  fit parameters taking the additional factor  $\cos(80^\circ)$  into account. An ideal 2D layer-by-layer growth should follow along this line.

#### 4.1.2. Thin Films of $[\text{C}_8\text{C}_1\text{Im}]\text{Cl}$ on Au(111)

After the proof-of-principle experiments with  $[\text{C}_8\text{C}_1\text{Im}][\text{Tf}_2\text{N}]$ , next, the preparation of  $[\text{C}_8\text{C}_1\text{Im}]\text{Cl}$  films Au(111) via ESID was studied, in order to pursue the investigations on the IL-solid interactions.  $[\text{C}_8\text{C}_1\text{Im}]\text{Cl}$  is thermally unstable, as recently shown by Lovelock *et al.*,<sup>147</sup> and therefore, this IL is not compatible with PVD. Thus, no ultrathin films of this IL could be prepared up to now. The results for the ESID films presented here are the first of their kind and will be compared to the reference system  $[\text{C}_8\text{C}_1\text{Im}][\text{Tf}_2\text{N}] / \text{Au}(111)$  presented above.

#### Growth Mode

As first step, the overall film growth mode was investigated. Ultrathin IL films, from the sub-monolayer range up to nominally 3 ML (1 ML  $[\text{C}_8\text{C}_1\text{Im}]\text{Cl}$  corresponds to a layer thickness of 0.72 nm, see equation 5) were deposited on Au(111) using ESID. The growth mode is again deduced from the attenuation of the

substrate XPS signals with increasing IL coverage: In Figure 4.4, the Au 4f signals in  $0^\circ$  and  $80^\circ$  emission are plotted against nominal coverage. As in Section 4.1.1, the nominal coverage values were determined from the attenuation of the substrate signals measured at  $0^\circ$ , i.e. in the bulk sensitive geometry. For comparison, the corresponding data points of  $[\text{C}_8\text{C}_1\text{Im}][\text{Tf}_2\text{N}]$  from the previous section are also included in Figure 4.4; they perfectly follow the dashed line, which shows the predicted behavior at  $80^\circ$  for layer-by-layer growth. For  $[\text{C}_8\text{C}_1\text{Im}]\text{Cl}$ , the  $80^\circ$  data initially also fall onto the dashed line, for coverages up to 0.3 – 0.4 nm ( $\sim 0.5$  ML). For higher coverages, however, the measured data points for  $[\text{C}_8\text{C}_1\text{Im}]\text{Cl}$  lie significantly above the “ideal”  $80^\circ$  line, that is, the substrate signals are much less attenuated than expected for a 2D film morphology. These findings clearly indicate that 3D island growth sets in after a first closed layer of  $[\text{C}_8\text{C}_1\text{Im}]\text{Cl}$  with 0.5 ML thickness was formed on the Au substrate, in a Stranski-Krastanov growth type mode. A similar growth behavior was witnessed by ARXPS for  $[\text{C}_n\text{C}_1\text{Im}][\text{Tf}_2\text{N}]$  PVD films grown on silica surfaces, where IL islands grew on top of a first wetting layer.<sup>45, 148</sup>

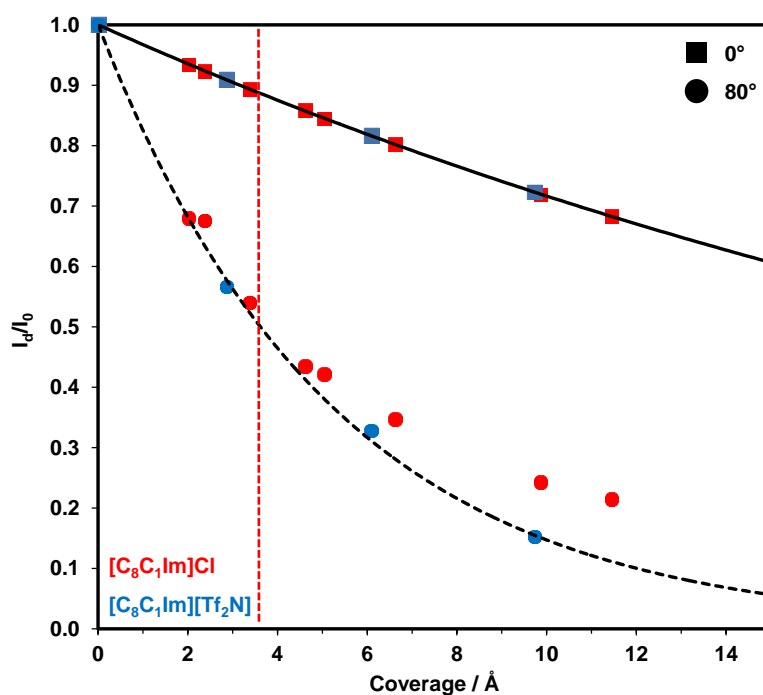


Figure 4.4: Decay of the Au 4f substrate signal as a function of coverage for emission angles of  $0^\circ$  and  $80^\circ$ . The dotted line is calculated from the  $0^\circ$  fit parameters taking the additional factor  $\cos(80^\circ)$  into account. An ideal 2D layer-by-layer growth should follow along this line. The red dotted line indicates a  $[\text{C}_8\text{C}_1\text{Im}]\text{Cl}$  coverage of 0.5 ML (= one closed ion layer).

---

## Initial Adsorption Behavior

Next, the focus is turned on the initial adsorption behavior at the metal-IL interface. In Figure 4.5, the C 1s, N 1s and Cl 2p spectra of  $[\text{C}_8\text{C}_1\text{Im}]\text{Cl}$  thin films of increasing thickness are depicted for emission angles of  $0^\circ$  and  $80^\circ$ . Apart from the gold substrate signals, no other elements were detected, which again demonstrates the cleanliness of the IL-ESID process. The two peaks in the C 1s region originate from the  $\text{C}_{\text{hetero}}$  and  $\text{C}_{\text{alkyl}}$  atoms of the cation, and the single peak in the N 1s region stems from the two N-atoms of the imidazolium ring. In the Cl 2p region, only the expected doublet structure due to spin-orbit splitting is visible. From the quantitative analysis, it is deduced that the calculated IL composition fits very well to expected nominal stoichiometry, within the margin of error of  $\pm 10\%$ , again ruling out a significant excess of cations due to the ESI process. Analysis of the coverage dependence of XPS data in Figure 4.5 suggests an initial adsorption behavior similar to that of  $[\text{C}_8\text{C}_1\text{Im}][\text{Tf}_2\text{N}]$ . Below 0.3 ML, no enrichment or depletion of certain elements in  $80^\circ$  is detected. Therefore, coadsorption of cations and anions directly on the Au(111) surface is suggested, with the octyl chains lying flat. For coverages  $> 0.3$  ML, an enhancement of the  $\text{C}_{\text{alkyl}}$  signal at  $80^\circ$ , i.e., surface enrichment of the octyl chains, is observed. A comparison of the C 1s spectra of  $[\text{C}_8\text{C}_1\text{Im}][\text{Tf}_2\text{N}]$  and  $[\text{C}_8\text{C}_1\text{Im}]\text{Cl}$  with similar coverage clearly reveals that the intensity increase of the  $\text{C}_{\text{alkyl}}$  signal at  $80^\circ$  is more pronounced for  $[\text{C}_8\text{C}_1\text{Im}]\text{Cl}$  (cf. table 4.2). A similar effect was also found in a previous ARXPS study of the outer surface of macroscopic IL films, that is, at the IL/vacuum interface: there, the degree of enrichment of the octyl chains within the surface layer of  $[\text{C}_8\text{C}_1\text{Im}]\text{X}$  ILs increases with decreasing size (and increasing coordination capability) of the anion X.<sup>145</sup> As concluded above from the attenuation of the substrate signal, further IL deposition on top of the first closed layer (with a coverage of 0.5 ML) leads to formation of IL islands for  $[\text{C}_8\text{C}_1\text{Im}]\text{Cl}$ . This behavior is in contrast to the observations for  $[\text{C}_8\text{C}_1\text{Im}][\text{Tf}_2\text{N}]$ , where layer-by-layer growth was observed at least up to 10 ML. This difference in growth mode is also reflected in a different behavior of the BE shifts with coverage for  $[\text{C}_8\text{C}_1\text{Im}]\text{Cl}$  and  $[\text{C}_8\text{C}_1\text{Im}][\text{Tf}_2\text{N}]$ . As demonstrated earlier for  $[\text{C}_n\text{C}_1\text{Im}][\text{Tf}_2\text{N}]$  PVD films on Au(111), shifts toward higher BE positions are expected for thicker layers, due to a larger average distance to the substrate.<sup>46</sup>

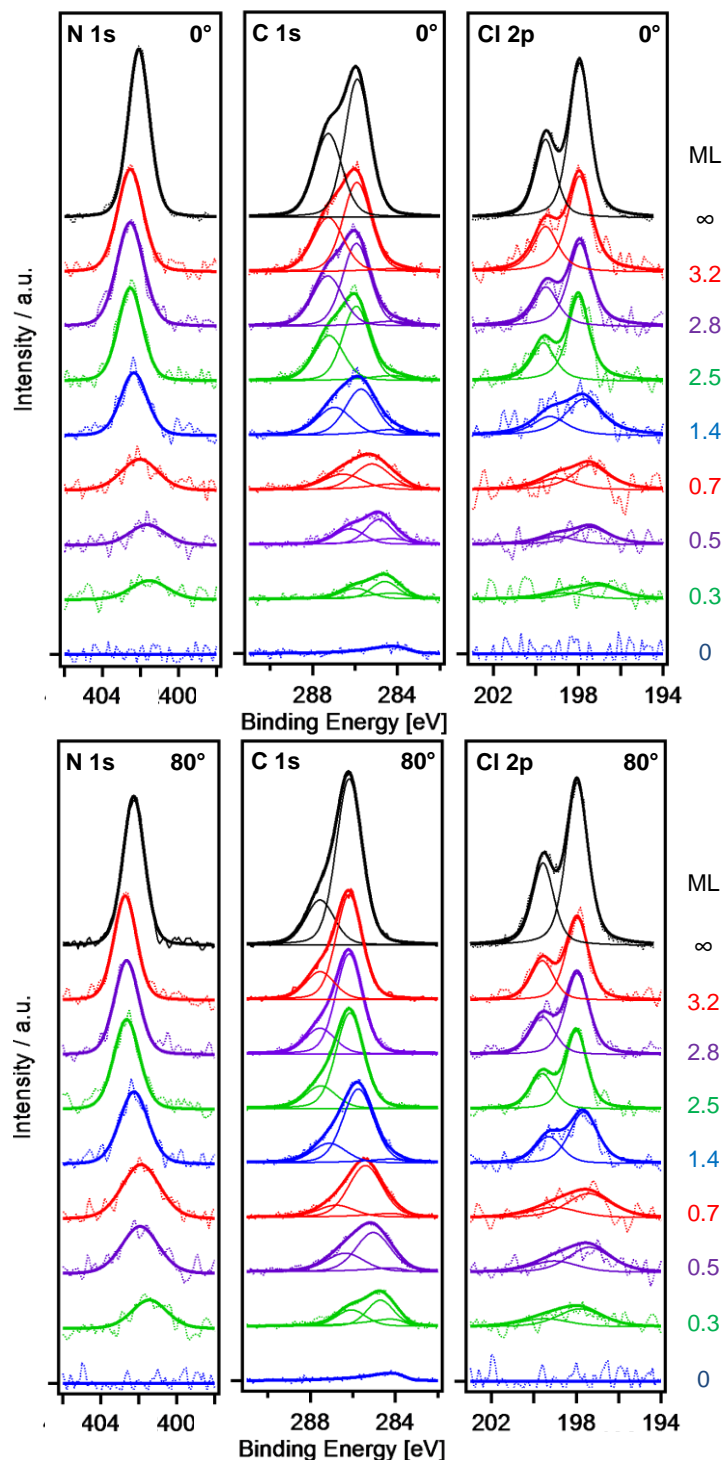


Figure 4.5: Waterfall plots of IL-ESID films of  $[\text{C}_8\text{C}_1\text{Im}]\text{Cl}$  on  $\text{Au}(111)$  with different coverages starting from the pristine substrate (0) up to a manually deposited macroscopic film ( $\infty$ ). Depicted are the N 1s, C 1s, and Cl 2p core level spectra for  $0^\circ$  and  $80^\circ$  emission. The given coverages are calculated from the  $0^\circ$  Au 4f attenuation. Due to island formation these values can only be seen as a rough estimation of the average IL coverage.

Coverage / ML	$C_{alkyl} / C_{hetero}$	
	$[C_8C_1Im]Cl$	$[C_8C_1Im][Tf_2N]$
0.3 / 0.4	1.5	1.5
1.4 / 1.2	3.5	2.5
$\infty$	3.3	2.2
<b>nominal</b>	<b>1.40</b>	<b>1.40</b>

Table 4.2:  $80^\circ C_{alkyl}/C_{hetero}$  ratios for ESI deposited  $[C_8C_1Im]Cl$  and  $[C_8C_1Im][Tf_2N]$  films on Au(111) in comparison with a manually deposited thick film ( $\infty$ ) and the respective nominal values.

Figure 4.6 shows the C 1s BE shift (average of  $C_{hetero}$  and  $C_{alkyl}$  values) at  $0^\circ$  (ID: 7 – 9 nm) as a function of coverage for  $[C_8C_1Im][Tf_2N]$  and  $[C_8C_1Im]Cl$ . For the layer-by-layer growth of  $[C_8C_1Im][Tf_2N]$  (red squares), the final BE positions are reached at a coverage above  $\sim 5$  ML ( $> 4.2$  nm) where XPS signals from ions not in contact with the substrate (that is, IL bulk signals) considerably exceed the attenuated signals originating from ions at the IL-metal interface (which are shifted in energy at least by  $-1.3$  eV). On the other hand, for  $[C_8C_1Im]Cl$  (blue diamonds), a constant BE position is already reached at  $\sim 2.5$  ML (1.8 nm). This saturation of BE position at a much lower nominal coverage of 1.8 nm is in line with the above proposed formation of  $[C_8C_1Im]Cl$  islands on top of a 0.5 ML thick wetting layer. In the case of such island formation, the majority of ions reach the bulk BE value at a lower nominal coverage due to their – on average – larger distance from the metal surface. Note that a low binding energy shoulder originating from uncovered parts of the wetting layer should still be visible in the  $0^\circ$  and  $80^\circ$  spectra in Figure 4.5 for nominal film thicknesses above 2.5 ML nominal coverage: however, these signal contributions are expected to be very small due to the large ID in  $0^\circ$  emission and due to shadowing effects at  $80^\circ$ .

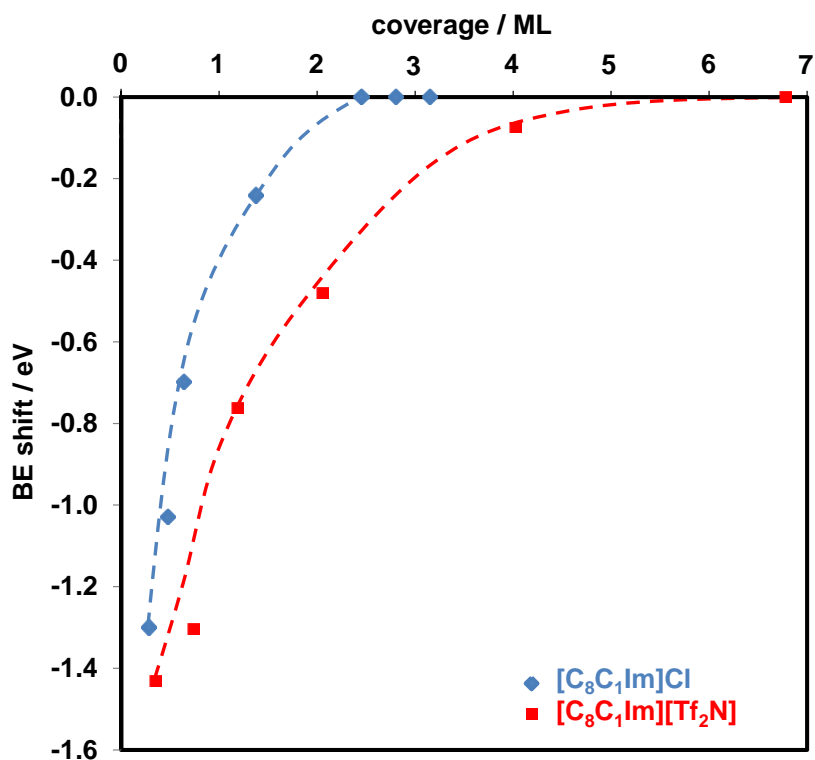


Figure 4.6: Decrease of  $0^\circ C$   $1s$  BE shift ( $C_{hetero}$ ,  $C_{alkyl}$   $1s$  average) with increasing coverage for  $[C_8C_1Im][Tf_2N]$  and  $[C_8C_1Im]Cl$ , respectively. A BE shift of 0 corresponds to the BE of the respective highest deposited coverage measured.

#### 4.1.3. Atomic Force Microscopy Investigations

In order to obtain further insights into the morphology of ESI-deposited IL films, both  $[C_8C_1Im][Tf_2N]$  and  $[C_8C_1Im]Cl$  were grown by IL-ESID on epitaxial Au(111) films supported on mica in a separate UHV system and analyzed by AFM under ambient conditions. Due to a reduced distance of the ESID source to the substrate surface, much higher IL coverages concentrated at a smaller deposition area could be achieved in this setup: after a deposition time of 3 h, the nominal film coverage for the AFM experiments was  $\sim 50$  ML; this is to be compared to the XPS experiments, where with similar deposition times only  $\sim 2$  ML thickness was achieved (albeit of a much larger area). Figure 4.7a shows an AFM image of the pristine Au/mica sample. Overall, the surface is smooth (mean height roughness:  $2.5 \text{ \AA}$ ), apart from the presence of grain boundaries between the micrometer large facets with preferential (111) surface orientation.<sup>88</sup> Figures 4.7b and 4.7c show AFM images of the Au/mica surface after ESI deposition of  $[C_8C_1Im][Tf_2N]$  and

$[\text{C}_8\text{C}_1\text{Im}]\text{Cl}$ , respectively. Due to the fact that the grain boundaries are still visible after  $[\text{C}_8\text{C}_1\text{Im}][\text{Tf}_2\text{N}]$  deposition in Figure 4.8b, it is most likely that the AFM cantilever penetrates most of the IL film. The absence of distinct islands is interpreted as further evidence for homogeneous spreading of  $[\text{C}_8\text{C}_1\text{Im}][\text{Tf}_2\text{N}]$  on the Au surface due to layer-by-layer growth. On the other hand, the equally distributed white spots in Figure 4.7c, with diameters ranging from about 1 to 4  $\mu\text{m}$  and heights between 60 and 200 nm, imply the formation of  $[\text{C}_8\text{C}_1\text{Im}]\text{Cl}$  islands on Au and thus confirm 3D growth.

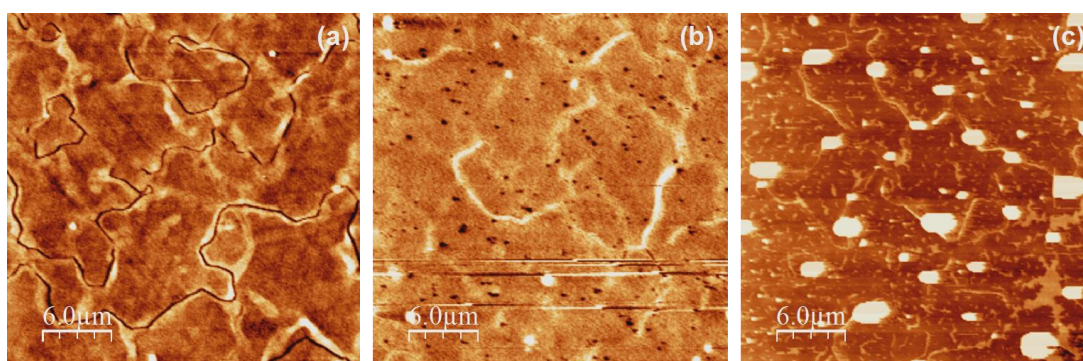


Figure 4.7: AFM images taken of a mica supported Au(111) film: a) image of the pristine surface; b) image of an ESI deposited  $[\text{C}_8\text{C}_1\text{Im}][\text{Tf}_2\text{N}]$  film; c) image of an ESI deposited  $[\text{C}_8\text{C}_1\text{Im}]\text{Cl}$  film.

#### 4.1.4. Optical Microscopy Investigations

The IL on Au/mica samples were also investigated with bright-field OM, and again, significant differences between  $[\text{C}_8\text{C}_1\text{Im}][\text{Tf}_2\text{N}]$  and  $[\text{C}_8\text{C}_1\text{Im}]\text{Cl}$  thin films become apparent. As shown in Figure 4.8a taken at 10x and 20x magnification, the  $[\text{C}_8\text{C}_1\text{Im}]\text{Cl}$  film is composed of equally distributed droplets with diameters ranging from 1 – 4  $\mu\text{m}$ . The absence of smaller droplets can be explained by Ostwald ripening.<sup>149</sup> In between these droplets an underlying homogeneous wetting layer is presumed due to the different color of this area compared to the pristine Au surface. The color change is best visible at the border of the deposition area marked with the dashed line.

No comparable structures are found within the  $[\text{Tf}_2\text{N}]$ -film. Only with strongly increased contrast, the corresponding images reveal that the overall color intensity decreases radially outwards and changes from yellow to blue (cf. Figure 4.8b). This

finding fits to the expected Gauss shape of the ESID profile. As the OM measurements were not performed on a highly ordered annealed Au(111) surface but on ex-situ prepared Au-covered mica samples, the dark spots visible in Figure 4.8b are most likely the result of preferred IL adsorption at surface defect sites or dust particles. These results provide another prove for 2D growth of  $[\text{C}_8\text{C}_1\text{Im}][\text{Tf}_2\text{N}]$  and 3D growth of  $[\text{C}_8\text{C}_1\text{Im}]\text{Cl}$ , respectively.

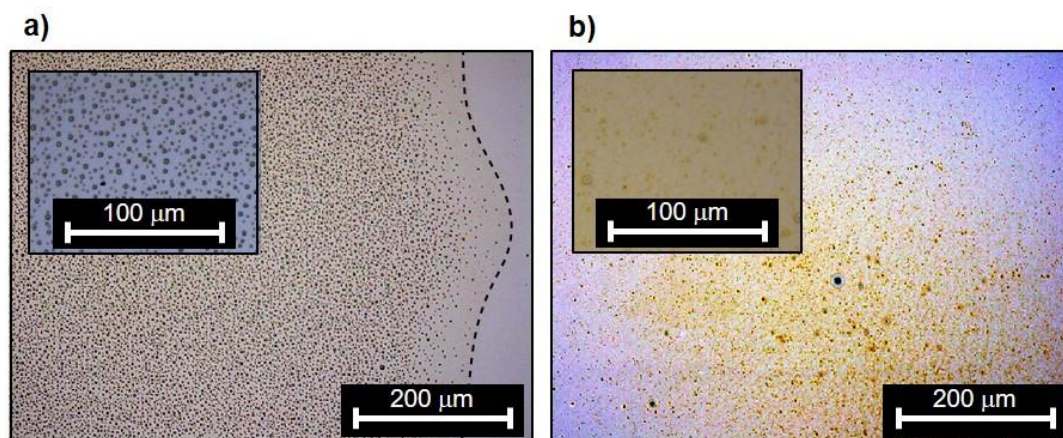


Figure 4.8: Bright-field OM images taken of a mica supported Au(111) film at 10x / 20x magnification: a) image of an ESI deposited  $[\text{C}_8\text{C}_1\text{Im}]\text{Cl}$  film; b) image of an ESI-deposited  $[\text{C}_8\text{C}_1\text{Im}][\text{Tf}_2\text{N}]$  film (with strongly increased contrast).

#### 4.1.5. Conclusions

The reason for the different film morphologies – layer by layer for  $[\text{C}_8\text{C}_1\text{Im}][\text{Tf}_2\text{N}]$  vs. island growth for  $[\text{C}_8\text{C}_1\text{Im}]\text{Cl}$  – is most likely related to the differences in the intermolecular interaction strengths of the two ILs. There are several studies focusing on the influence of the anion on the physicochemical properties. Fernandes et al. investigated the relative anion-cation interaction energies of different ILs, including imidazolium-based  $[\text{Tf}_2\text{N}]^-$  and  $\text{Cl}^-$  ILs with different chain lengths.<sup>150</sup> From tandem mass spectrometry (ESI-MS-MS) and also from quantum chemical calculations, stronger interionic interactions between the imidazolium cation and the anion are deduced for  $\text{Cl}^-$  compared to  $[\text{Tf}_2\text{N}]^-$  (cf., dissociation energies of 3.85 and 2.96 eV for  $[\text{C}_4\text{C}_1\text{Im}]\text{Cl}$  and  $[\text{C}_4\text{C}_1\text{Im}][\text{Tf}_2\text{N}]$ , respectively).<sup>150</sup> Deetlefs et al.<sup>151</sup> deduced from neutron diffraction data of several imidazolium-based ILs a decrease of hydrogen-bonding ability with increasing anion size: as the charge becomes more

delocalized the bonding strength of the anion with the acidic ring protons decreases. Kolbeck et al.<sup>71</sup> and Freire et al.<sup>152</sup> were studying the influence of anion-cation interactions on the surface tension of ILs. Both groups found a larger surface tension for n-alkyl imidazolium Cl<sup>-</sup> ILs than for their [Tf<sub>2</sub>N]<sup>-</sup> analogues. Hence, the higher coordination strength of the chloride compared to the [Tf<sub>2</sub>N]<sup>-</sup> anion might be the driving force for the [C<sub>8</sub>C<sub>1</sub>Im]Cl island growth on top of the wetting layer, whereas the weakly coordinating [Tf<sub>2</sub>N]<sup>-</sup> anion allows layer-by-layer growth for [C<sub>8</sub>C<sub>1</sub>Im][Tf<sub>2</sub>N]. Apart from these considerations concerning bulk properties, however, the interface might also play a role for the differences in growth mode. As mentioned above, a very high degree of molecular orientation for the [C<sub>8</sub>C<sub>1</sub>Im]Cl wetting layer at the Au(111) surface is revealed, with the densely packed octyl chains forming a nonpolar outer surface. Thus, the adsorption strength of IL molecules on top of this alkyl layer might be weakened, and thus, island nucleation is preferred, which then leads to efficient island growth subsequently. For the [C<sub>8</sub>C<sub>1</sub>Im][Tf<sub>2</sub>N] wetting layer, the packing density of the octyl chains – and thus, the molecular order – is less pronounced. The resulting more open structure of this wetting layer then might prevent early island nucleation, and the growing film exhibits a layer-by-layer growth. Note that if this effect was dominating, one would possibly expect island growth of [C<sub>8</sub>C<sub>1</sub>Im][Tf<sub>2</sub>N] on top of a [C<sub>8</sub>C<sub>1</sub>Im]Cl wetting layer, too. Such effects are known, e.g., from ex-situ experiments that show that [C<sub>4</sub>C<sub>1</sub>Im][Tf<sub>2</sub>N] forms nanodroplets on the (nonpolar) surface of highly oriented pyrolytic graphite (HOPG), whereas a layered film morphology is observed when the same IL is deposited on polar oxide surfaces.<sup>105</sup>

#### 4.1.6. Summary

Within the scope of this thesis, the first successful preparation of ultrathin IL films by means of electrospray ionization deposition (ESID) on surfaces under ultraclean and well defined UHV conditions was performed. Using a well-known system, namely, [C<sub>8</sub>C<sub>1</sub>Im][Tf<sub>2</sub>N] on Au(111), for the proof-of-concept investigation, it could be demonstrated that [C<sub>8</sub>C<sub>1</sub>Im][Tf<sub>2</sub>N] films obtained by ESID are virtually identical to films grown by standard physical vapor deposition (PVD). Despite the fact that the deposition rate for ESID was by more than one order of magnitude

---

smaller than for PVD, no contaminations were observed. Most importantly, quantitative XPS analysis revealed no measurable excess of cations for ESID, although the process was performed in the positive mode. This finding is attributed to the large excess of neutral IL ion pairs in the initial droplets formed during the ESI process. From quantitative ARXPS it is concluded that the IL film growth on Au(111) starts by forming a complete wetting layer of  $[\text{C}_8\text{C}_1\text{Im}][\text{Tf}_2\text{N}]$  (corresponding to a coverage of 0.5 ML). In this film, the ionic head groups are directly adsorbed on the Au(111) surface in a checkerboard configuration, with the octyl chains preferentially pointing towards vacuum. Further deposition leads to a homogeneous layer-by-layer film growth, again in perfect agreement with a previous IL-PVD study on the same system.<sup>46</sup> After establishing ESID as tool to grow ultrathin IL films, the initial adsorption behavior and growth mode of  $[\text{C}_8\text{C}_1\text{Im}]\text{Cl}$  on Au(111) was studied as a first example of an IL that cannot be prepared as ultrathin film otherwise. As for all halide ILs, PVD cannot be applied because thermal decomposition dominates before evaporation of intact ion pairs starts. By ARXPS, it was shown that  $[\text{C}_8\text{C}_1\text{Im}]\text{Cl}$  also forms a wetting layer on Au(111), with the cationic imidazolium ring and the chloride anion adsorbed next to each other in the checkerboard configuration. The orientation of the octyl chains towards vacuum in this wetting layer is even more pronounced than for  $[\text{C}_8\text{C}_1\text{Im}][\text{Tf}_2\text{N}]$  on Au(111), indicating a high degree of order in the  $[\text{C}_8\text{C}_1\text{Im}]\text{Cl}$  wetting layer. In contrast to  $[\text{C}_8\text{C}_1\text{Im}][\text{Tf}_2\text{N}]$ , further deposition of  $[\text{C}_8\text{C}_1\text{Im}]\text{Cl}$  leads to pronounced island growth on top of the wetting layer, which is independently deduced from the attenuation behavior of the gold signals, from the intensities and the binding energy changes of IL signals, and from ex-situ AFM and OM measurements. The difference between both ILs is attributed to differences in the cation-anion interactions and in the degree of order in the wetting layer of the two ILs.

## 4.2. [C<sub>2</sub>C<sub>1</sub>Im][EtOSO<sub>3</sub>] and [C<sub>2</sub>C<sub>1</sub>Im][OTf] on Pristine and Modified Au Surfaces

In this section, another complex ARXPS study will be presented. The interactions of [C<sub>2</sub>C<sub>1</sub>Im][EtOSO<sub>3</sub>] and [C<sub>2</sub>C<sub>1</sub>Im][OTf] thin films with pristine and Pd-modified Au model surfaces were investigated to obtain a better understanding of real hydrogenation SCILL catalysts, exhibiting high activity and selectivity. Due to the limited thermal stability of [C<sub>2</sub>C<sub>1</sub>Im][EtOSO<sub>3</sub>], both PVD and ESID techniques were combined to obtain clean IL deposits. To study potential effects of carbon impurities settling on the catalyst surface on IL wetting and adsorption behavior, thin IL films were deposited on pristine Au(111) and on a carbon-contaminated Au surface. In addition to [C<sub>2</sub>C<sub>1</sub>Im][EtOSO<sub>3</sub>], the thermally more stable IL [C<sub>2</sub>C<sub>1</sub>Im][OTf] was chosen for more elaborate studies on the interface interactions of an IL with Pd deposited onto Au(111) previous or subsequent to IL thin film deposition.

### 4.2.1. Thermal Decomposition of [C<sub>2</sub>C<sub>1</sub>Im][EtOSO<sub>3</sub>]

When performing IL-PVD tests with [C<sub>2</sub>C<sub>1</sub>Im][EtOSO<sub>3</sub>], a drastic increase of background pressure was observed during deposition (cf. Figure 4.9). Due to the negligible vapor pressure of ILs<sup>53</sup> the increase in pressure cannot be explained by the evaporation of intact ion pairs, but is an indication for the formation of more volatile decomposition products. Thermal decomposition of [C<sub>2</sub>C<sub>1</sub>Im][EtOSO<sub>3</sub>] is known from literature: Upon heating the IL under vacuum conditions, Fernandez et al. observed that the decomposition of the [EtOSO<sub>3</sub>]<sup>-</sup> anion sets in at temperatures as low as 393 K. Heym et al. studied the rate of vaporization and the thermal decomposition of high-boiling ILs, including [C<sub>2</sub>C<sub>1</sub>Im][EtOSO<sub>3</sub>], by means of thermal gravimetric analysis performed in an N<sub>2</sub>/He atmosphere. In the temperature range from 513 – 613 K, they found that [C<sub>2</sub>C<sub>1</sub>Im][EtOSO<sub>3</sub>] decomposes without measurable amounts of the IL evaporating as intact ion pairs.<sup>67</sup> In contrast, evaporation of intact [C<sub>2</sub>C<sub>1</sub>Im][EtOSO<sub>3</sub>] ion pairs was observed in experiments performed by Deyko et al., in which a thin film of the IL adhering to the surface of a dipstick was heated in UHV atmosphere. The vapor was analyzed by MS and

surprisingly, no indication for decomposition was found.<sup>68</sup> In this work, MS was applied to investigate the behavior of bulk amounts of  $[\text{C}_2\text{C}_1\text{Im}][\text{EtOSO}_3]$  upon heating under UHV conditions, in order to study the apparent decomposition of the IL during the PVD process manifesting in the detected drastic increase in pressure. Mass spectra were taken in the temperature range from 360 to 520 K in steps of 10 K (for the experimental setup, see section 2.4.). Up to a temperature of 400 K, all detected masses can be attributed to residual gas species. Therefore, only relevant spectra recorded at temperatures above 400 K are depicted in Figure 4.10. Starting at 400 K, the formation of ethanol (EtOH) and above 440 K, the formation of methanol (MeOH) is deduced from the MS data due to the presence of the coinciding main MS peak<sup>153</sup> of EtOH and MeOH at  $m/z = 31$  and their characteristic second most intense peaks at  $m/z = 32$  and 45 for MeOH and EtOH, respectively. The intensity of the main peak at  $m/z = 31$  increases by the factor of ten when the temperature rises from 400 to 440 K and by a factor of about 1000 when increasing further to 520 K. The intensity at  $m/z = 45$  (EtOH) increases more strongly up to a temperature of 500 K than that of  $m/z = 32$  (MeOH). Moreover, the relative intensity of the respective characteristic peaks compared to the coinciding main peak at  $m/z = 31$  is 75 % for MeOH (32) compared to only 50 % for EtOH (45). Hence, it can be concluded, that EtOH is produced to a much larger extent than MeOH. At temperatures above 480 K, the appearance of further fragments in MS indicates the formation of other – high boiling point ( $T_B$ ) – decomposition products, namely 1-methylimidazole (1-MeIm;  $T_B = 470$  K,  $m/z = 82$ ) and 1-ethylimidazole (1-EtIm;  $T_B = 379$  K,  $m/z = 96$ ). Above 480 K, also characteristic MS peaks of intact cations ( $m/z = 111$ ) and anions ( $m/z = 125$ ) are observed, indicating the simultaneous evaporation of intact ion pairs alongside decomposition products. Notably, the fragmentation pattern of the  $[\text{C}_2\text{C}_1\text{Im}]^+$  cation has its highest contribution at  $m/z = 82$ , i.e. at the same  $m/z$  value where the only strong intensity of 1-MeIm is observed. By comparing the relative intensities at  $m/z = 111$  and 82, it becomes apparent that 1-MeIm contributes to a minor extent to the overall intensity measured at  $m/z = 82$ , as most of the intensity derives from the  $[\text{C}_2\text{C}_1\text{Im}]^+$  cation. Thus, the formation of 1-EtIm seems to be highly favored over the formation of 1-MeIm. Table 4.3 summarizes the most prominent  $m/z$  values and the relative intensities for both intact IL ions and the main decomposition products.<sup>153, 154</sup>

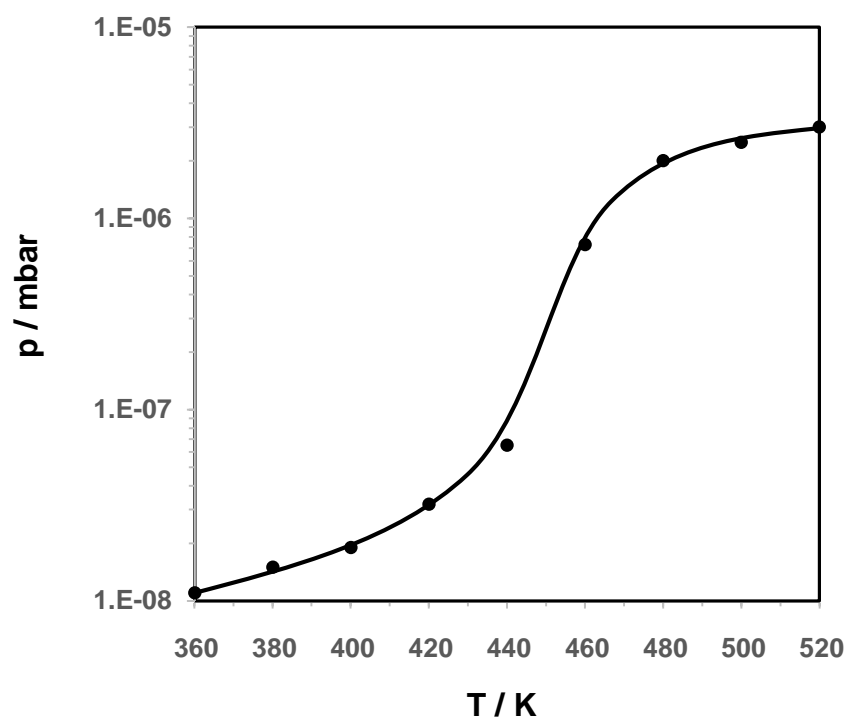


Figure 4.9: Background pressure increase upon heating  $[C_2C_1Im][EtOSO_3]$  in the Knudsen cell of the PVD apparatus (with open shutter). Note the logarithmic scale on the pressure axis!

$[C_2C_1Im]^+$	$EtOSO_3^-$	EtOH	MeOH	1-EtIm	1-MeIm
82 (100 %)	64	31 (100 %)	31 (100 %)	96 (100 %)	82
111 (36 %)	125	45 (52 %)	32 (74 %)	81 (52 %)	
81 (16 %)	126		29 (44 %)	68 (33 %)	

Table 4.3: High intensity  $m/z$  values for the intact IL ions and the main decomposition products: ethanol (EtOH), methanol (MeOH), 1-EtIm (1-ethylimidazole), and 1-MeIm (1-methyl-imidazole) with relative intensities from MS-databases given in brackets.<sup>153, 154</sup>

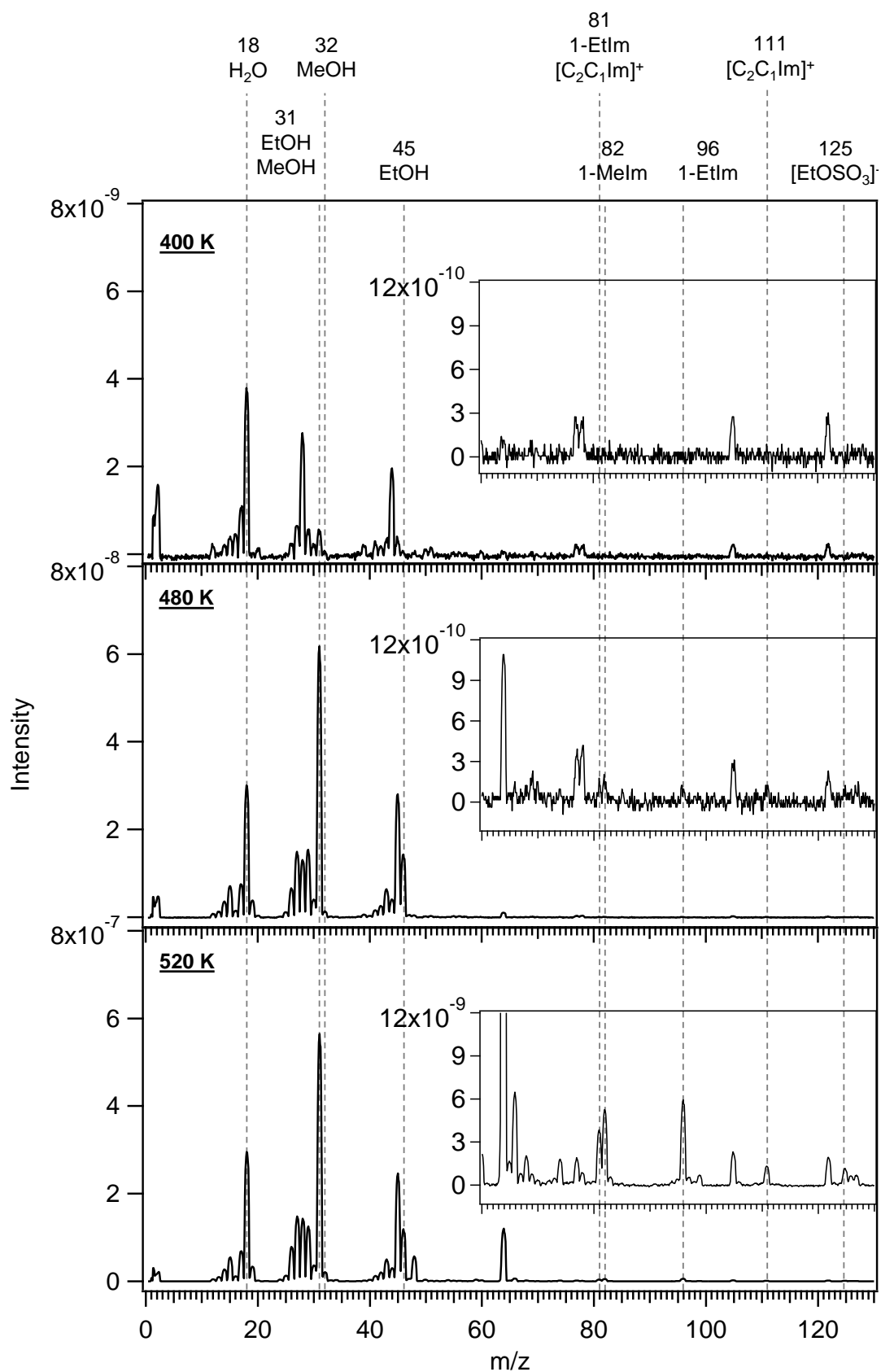


Figure 4.10: Mass spectra of  $[\text{C}_2\text{C}_1\text{Im}][\text{EtOSO}_3]$  heated in UHV to temperatures of 400, 480 and 520 K. (Note: The peaks at  $m/z = 77, 78, 105$  and  $122$  can be assigned to tenacious benzoic acid, which was used in previous experiments).

In the following, pathways for the thermal decomposition of  $[\text{C}_2\text{C}_1\text{Im}][\text{EtOSO}_3]$  are suggested, which are based on mechanisms found in literature for similar ILs and which are suitable to explain the formation of the main decomposition products deduced from the MS data. The first proposed decomposition mechanism involves both, the anion and the cation, and is based on a study by Kroon et al. who found that the thermal decomposition of  $[\text{C}_2\text{C}_1\text{Im}]\text{Cl}$  follows a nucleophilic substitution mechanism.<sup>155</sup>

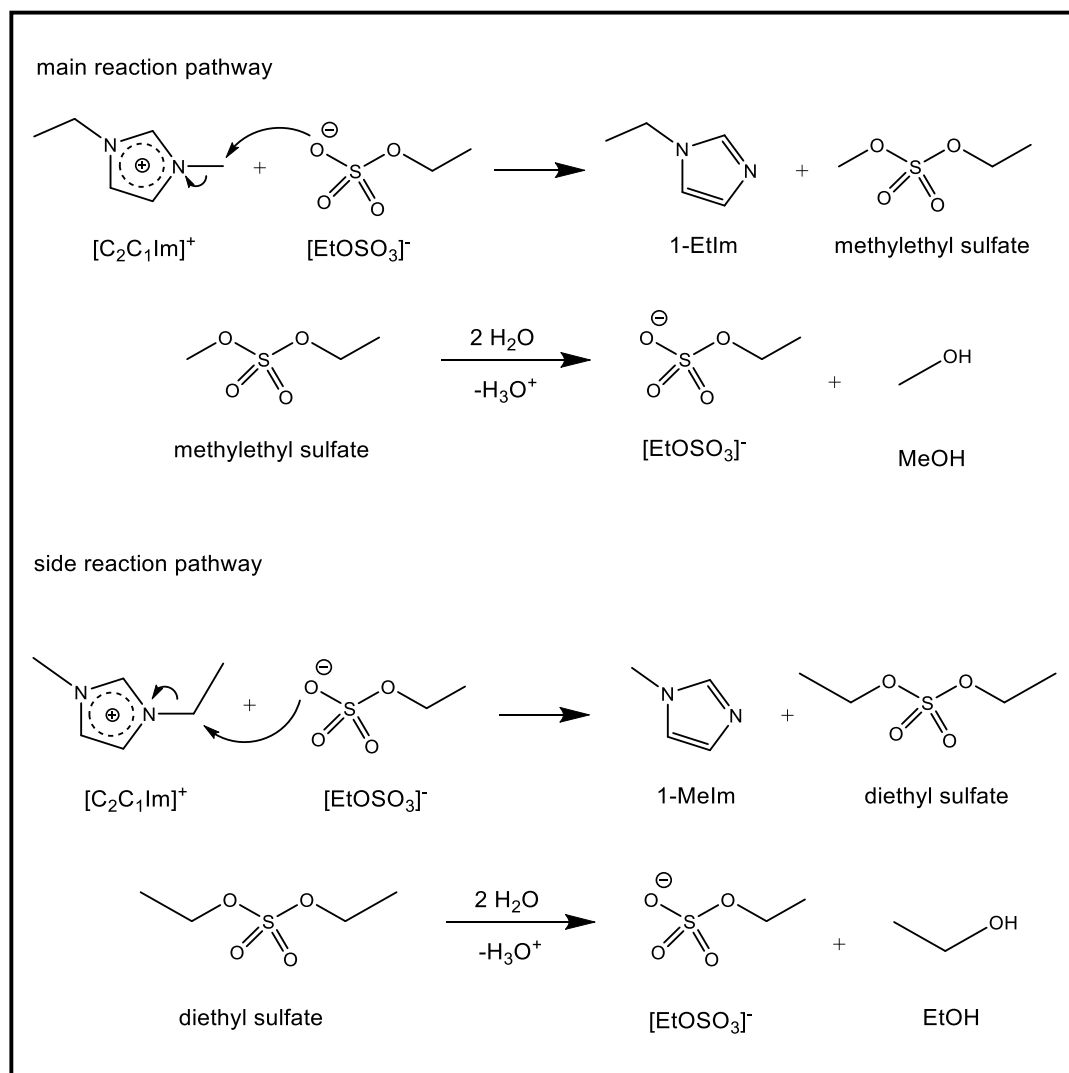


Figure 4.11: Proposed pathway 1 for the thermal decomposition of  $[\text{C}_2\text{C}_1\text{Im}][\text{EtOSO}_3]$ .

This mechanism was applied to  $[\text{C}_2\text{C}_1\text{Im}][\text{EtOSO}_3]$  and is depicted in Figure 4.11. The first step is the nucleophilic attack of one of the negatively charged oxygen atoms of the  $[\text{EtOSO}_3]^-$  anion on one of the  $[\text{C}_2\text{C}_1\text{Im}]^+$  alkyl chains, following an  $\text{S}_{\text{N}}2$  type reaction mechanism. This leads to the formation of either diethyl sulfate

and 1-methylimidazole (1-MeIm) or methylethyl sulfate and 1-ethylimidazole (1-EtIm). Due to the initial  $S_N2$  type attack of the anion, steric reasons are expected to lead to a preferential demethylation of the cation under formation of 1-EtIm, which was also found experimentally for  $[C_2C_1Im]^+$  ILs with  $NO_3^-$ ,  $Cl^-$ , and  $Br^-$  as the anions.<sup>156</sup>

The highly hygroscopic IL  $[C_2C_1Im][EtOSO_3]$  retains relatively large amounts of water, even after degassing the IL at elevated temperatures in UHV, as proven by the high quantities of water evaporating from the sample which are detected by MS upon heating (cf. Figure 4.10). Consequentially, the hydrolysis of the respective dialkyl sulfate is expected to be the second and final step of this decomposition pathway. Hydrolysis of the by-product diethyl sulfate results in the formation of  $H_3O^+$ , EtOH and  $[EtOSO_3]^-$ . The main product methylethyl sulfate is expected to predominantly hydrolyze under formation of MeOH and  $[EtOSO_3]^-$ , as  $[EtOSO_2OMet]$  is known to be a much stronger methylating rather than an ethylating agent.<sup>157</sup>

Reaction pathway 1 gives an explanation for all main decomposition products observed by MS. However, it cannot explain the formation of EtOH at temperatures just above 400 K, at which no other decomposition products are detected. Moreover, the large excess of EtOH over MeOH detected by MS is inconsistent with the proposed sequence of an initial preferential  $S_N2$  attack on the cation's methyl group and the subsequent hydrolysis step, resulting mainly in the formation of MeOH rather than EtOH. Thus, a competing second decomposition pathway is suggested. Jacquemin et al. investigated the stability of alkyl sulfate based ILs in the presence of water and alcohols. It could be shown that the cation plays a negligible role concerning the ILs hydrolytic stability and consequentially, no decomposition of any IL cation alongside the ongoing decomposition of the alkyl sulfate-based anions was observed.<sup>158</sup> The traces of water in  $[C_2C_1Im][EtOSO_3]$  that are still present under UHV conditions might be sufficient to provoke the thermally induced hydrolysis of the  $[EtOSO_3]^-$  anion. The respective hydrolytic reaction mechanism based on the work of Wolfenden et al.,<sup>159</sup> who investigated the hydrolysis of  $[MeOSO_3]^-$  in aqueous solutions under formation of MeOH and hydrogen sulfate ( $[HOSO_3]^-$ ) is depicted in Figure 4.12.

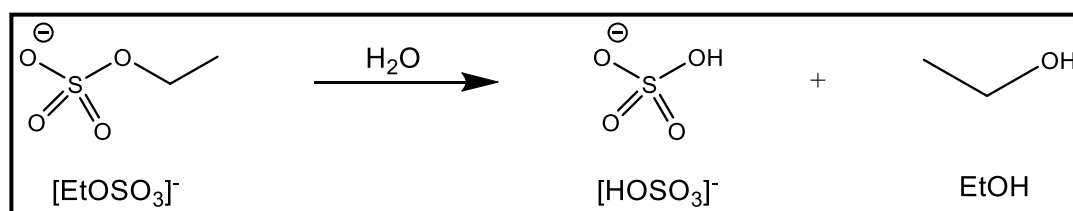


Figure 4.12: Proposed pathway 2 for the thermal decomposition of  $[C_2C_1Im][EtOSO_3]$ : Hydrolysis of the anion by traces of water.

In summary, thermal decomposition of  $[C_2C_1Im][EtOSO_3]$  already starts at temperatures of around 400 K, at which hydrolysis of the anion results in the formation of EtOH and  $[HOSO_3]^-$ . At higher temperatures, starting at approx. 440 K, a second decomposition mechanism sets in, involving the  $S_N2$  attack of the anion on one of the cation's alkyl group (preferentially on the methyl group) under formation of 1-EtIm/1-MeIm and methylethyl sulfate/diethyl sulfate. The latter species consecutively hydrolyze under formation of MeOH/EtOH and  $[EtOSO_3]^-$ . For temperatures above 480 K, evaporation of intact ion pairs is observed alongside the ongoing decomposition. As mentioned above, evaporation of intact  $[C_2C_1Im][EtOSO_3]$  ion pairs was found by Deyko et al. for thin IL films heated under UHV conditions.<sup>68</sup> This result was opposed to a study of Heym et al., in which only decomposition and no evaporation of intact ion pairs was observed when heating bulk amounts of  $[C_2C_1Im][EtOSO_3]$  in a He/N atmosphere.<sup>67</sup> In this work, both decomposition and simultaneous evaporation of intact ion pairs is observed when heating bulk amounts of the IL in UHV. Accordingly, UHV conditions seem to be required for successful evaporation of intact ion pairs. Further, complete evaporation of  $[C_2C_1Im][EtOSO_3]$  without noticeable decomposition is only feasible for very thin IL films with a high surface/bulk ratio allowing for a rapid total evaporation. When bulk amounts of the IL are used, the surface/bulk ratio is low and consequentially, the rate of evaporation is drastically reduced. Thus, decomposition will set in before the evaporation of the IL has completed.

In the following, thin films of the IL prepared by PVD are compared to IL films prepared by ESID in order to study the potential influence of the volatile decomposition products on the thin film formation.

#### 4.2.2. PVD vs. ESID [ $C_2C_1Im$ ][EtOSO<sub>3</sub>] Thin Films

For better comparison to former studies on the IL/solid interface, a Au(111) substrate was used for the first [ $C_2C_1Im$ ][EtOSO<sub>3</sub>] thin film investigations. As shown in chapter 4.1, ESID can be used to fabricate IL thin films with comparable quality to films prepared by thermal evaporation. As a drawback, ESID is a time consuming process. Thus, only ESID films up to coverages of  $\sim 1.5$  ML were produced. Higher coverages were obtained by PVD only. A comparison of normal emission C 1s and O 1s spectra of ESID and PVD deposited films with comparable coverages is depicted in Figure 4.13. Here, the focus is set on the differences between PVD- and ESID-deposited IL films. A detailed description and interpretation of the spectra concerning the IL adsorption behavior will be given in the next section.

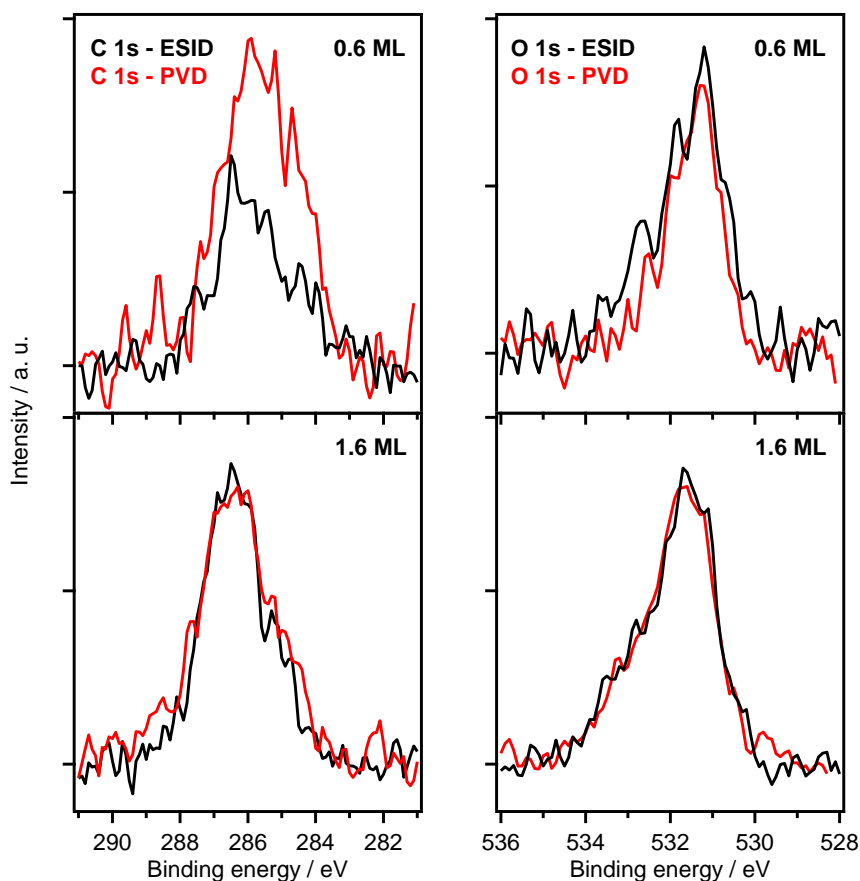


Figure 4.13: High resolution normal emission XP spectra of the C 1s and the O 1s region of [ $C_2C_1Im$ ][EtOSO<sub>3</sub>] thin films deposited via ESID (black) and PVD (red) onto a Au(111) substrate. The coverage in ML is given in the top right corner.

Figure 4.13 shows that for all coverages, O 1s spectra look similar for both techniques, whereas the C 1s peak of the 0.6 ML PVD film is strongly enhanced compared to the corresponding ESID film. Only at higher coverages, also the C 1s spectra exhibit a comparable shape for both techniques as seen in Figure 4.13 in case of the 1.6 ML films. An excess of C being present at the surface after PVD deposition of  $[C_2C_1Im][EtOSO_3]$  films with coverages  $< 1.0$  ML could also be clearly deduced from quantitative XPS analysis (see table 4.4). As the influence of orientation effects on the relative signal intensities is negligible for normal emission, the additional C 1s intensity is attributed to the codeposition of carbon-rich decomposition products – possibly 1-MeIm and 1-EtIm – alongside intact ion pairs. For higher coverages, which are still far below the information depth, quantitative XPS analysis reveals the correct stoichiometry of PVD-deposited films (see table 4.4) within the margin of error. This might be due to the expulsion of the initially co-adsorbed decomposition products from the surface due to comparatively stronger interactions of  $[C_2C_1Im][EtOSO_3]$  with the Au(111) substrate. Having lost the adherence to the substrate, the more volatile decomposition products tend to be expelled from the sample.

<b>0°/Prep.</b>	<b>Å</b>	<b>ML</b>	<b>C<sub>het</sub></b>	<b>C<sub>alk</sub></b>	<b>O<sub>s</sub></b>	<b>O<sub>Et</sub></b>	<b>N</b>	<b>S</b>
<b>nominal</b>			<b>6</b>	<b>2</b>	<b>3</b>	<b>1</b>	<b>2</b>	<b>1</b>
<b>PVD</b>	4.1	0.6	7.7	2.6	1.7	0.6	1.9	0.5
<b>ESID</b>	5.8	0.8	5.9	1.9	3.1	1.1	2.0	1.0
<b>ESID</b>	10.6	1.6	6.2	2.0	2.9	1.0	2.0	1.0
<b>PVD</b>	10.7	1.6	6.1	1.9	2.9	1.0	2.0	1.1
<b>PVD</b>	24.5	3.6	6.1	2.0	3.0	0.9	2.0	1.0
<b>PVD</b>	55.5	8.2	6.1	1.9	3.0	1.0	2.0	1.0
<b>80°/Prep.</b>								
<b>PVD</b>	4.1	0.6	7.6	2.3	2.2	0.7	1.9	0.6
<b>ESID</b>	5.8	0.8	5.7	2.1	2.9	1.4	1.9	1.0
<b>ESID</b>	10.5	1.5	6.0	2.0	2.9	1.2	2.0	1.0
<b>PVD</b>	10.6	1.5	6.0	2.0	2.8	1.2	1.9	1.1
<b>PVD</b>	15.6	2.3	6.2	2.0	2.9	1.1	1.8	1.1
<b>PVD</b>	24.2	3.6	6.1	1.9	2.9	1.1	1.9	1.1

Table 4.4: Calculated atomic ratios of ESID and PVD  $[C_2C_1Im][EtOSO_3]$  thin films in dependence of emission angle and coverage. (For the differences between the calculated thicknesses of the two highest IL coverages in normal and 80° emission, see text).

Table 4.4 shows that in line with the detailed discussion in chapter 4.1 for  $[\text{C}_8\text{C}_1\text{Im}][\text{Tf}_2\text{N}]$  and  $[\text{C}_8\text{C}_1\text{Im}]\text{Cl}$  films deposited via ESID onto Au(111), the stoichiometry of ESID deposited  $[\text{C}_2\text{C}_1\text{Im}][\text{EtOSO}_3]$  films matches the nominal values within the margin of error. This means that although the ESI process was performed in positive bias mode, no excess of cations was detected. This observation is again attributed to the large excess of neutral IL ion pairs in the initial droplets formed during the ESI process.

### 4.2.3. Initial Adsorption Behavior

No significant enrichment of signals belonging to one of the ionic species is observed in  $80^\circ$  emission for the 0.6 and 0.8 ML ESID films (cf. table 4.4). Hence, it can be concluded, that anions and cations adsorb next to each other in a checkerboard arrangement. Figure 4.14 shows high resolution XP spectra of the O 1s region of  $[\text{C}_2\text{C}_1\text{Im}][\text{EtOSO}_3]$  thin films, deposited via ESID (0.4 and 0.6 ML) or PVD (1.6 and 8.2 ML) onto a Au(111) substrate. Each spectrum consists of a main peak at  $\sim 531.5$  eV and a shoulder shifted by 1.2 eV to higher BE with respect to the main peak – in line with previous XPS studies involving macroscopic amounts of the same IL.<sup>160, 161</sup> As seen in the  $0^\circ$  spectra (black) of Figure 4.14, a ratio of 3:1 is found. This ratio matches perfectly to the anion's molecular structure, having three chemically identical oxygen atoms ( $[\text{EtOSO}_3]^-$ ,  $\text{O}_\text{S}$ ) which are bound to sulfur only, and one oxygen atom ( $[\text{EtOSO}_3]^-$ ,  $\text{O}_\text{Et}$ ) which is chemically different to the others as it is also bound to the ethyl chain.

For the very thin IL ESID films below or around 0.5 ML (i.e. one layer of IL in a checkerboard arrangement) in  $80^\circ$  emission, an enrichment of the  $\text{O}_\text{Et}$  species is found, as shown by the red spectra in Figure 4.14. Apparently, the  $[\text{EtOSO}_3]^-$  anion at the interface preferentially adsorbs with the negatively charged oxygen atoms in contact with the Au surface and with the ethyl chain pointing towards vacuum. With increasing coverage, the enrichment of the  $\text{O}_\text{Et}$  species diminishes, indicating a more random molecular orientation starting at the second molecular layer. As seen in table 4.4, in  $80^\circ$  for low coverages, there is also a slight enrichment found for C 1s (alkyl) compared to C 1s (hetero). However, this observation is more ambiguous since there are additional contributions to both C 1s species from the cation. For the

cation, no distinct enrichment effects can be observed in corresponding  $80^\circ$  XP spectra. Thus, the imidazolium ring is expected to adopt a flat-lying adsorption geometry, which was also found for other imidazolium-based ILs (with  $[\text{Tf}_2\text{N}]^-$  or  $\text{Cl}^-$  as anion) adsorbing on Au(111).<sup>46, 56</sup>

Interestingly, compared to other imidazolium-based ILs adsorbed on Au(111), a significantly lower shift in BE is detected when going from coverages in the sub-ML regime to quasi bulk-like coverages. For  $[\text{Tf}_2\text{N}]^-$  or  $\text{Cl}^-$  ILs, the shift of both anion and cation signals was found to be well above 1 eV, indicating strong electronic interactions of the IL adsorbates with the Au substrate.<sup>46, 56</sup> For  $[\text{C}_2\text{C}_1\text{Im}][\text{EtOSO}_3]$ , however, the shift in BE is significantly reduced and lies well below 0.5 eV for all measured core levels, indicating comparatively weaker electronic adsorbate-substrate interactions.

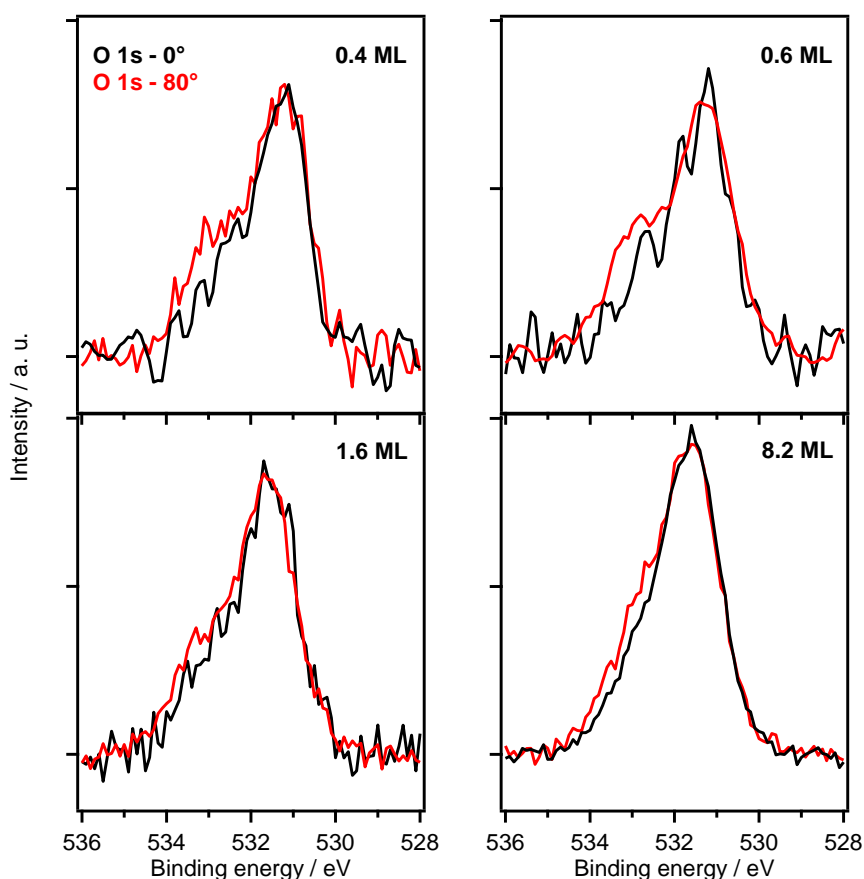


Figure 4.14: High resolution XP spectra of the O 1s region of  $[\text{C}_2\text{C}_1\text{Im}][\text{EtOSO}_3]$  thin films deposited via ESID (top spectra) or PVD (bottom spectra) onto a Au(111) substrate: black: ( $0^\circ$  emission); red: ( $80^\circ$  emission). The coverage in ML is given in the top right corner. The spectra are normalized by random factors for better comparison.

#### 4.2.4. Growth Mode

After having focused on the adsorption behavior of the first molecular layers, the consecutive growth behavior of  $[\text{C}_2\text{C}_1\text{Im}][\text{EtOSO}_3]$  on Au(111) will be discussed next. Figure 4.15 shows the Au 4f substrate signal attenuation measured under normal and  $80^\circ$  emission plotted against the calculated thickness of the IL film determined by applying equation 4 on the normal emission data.

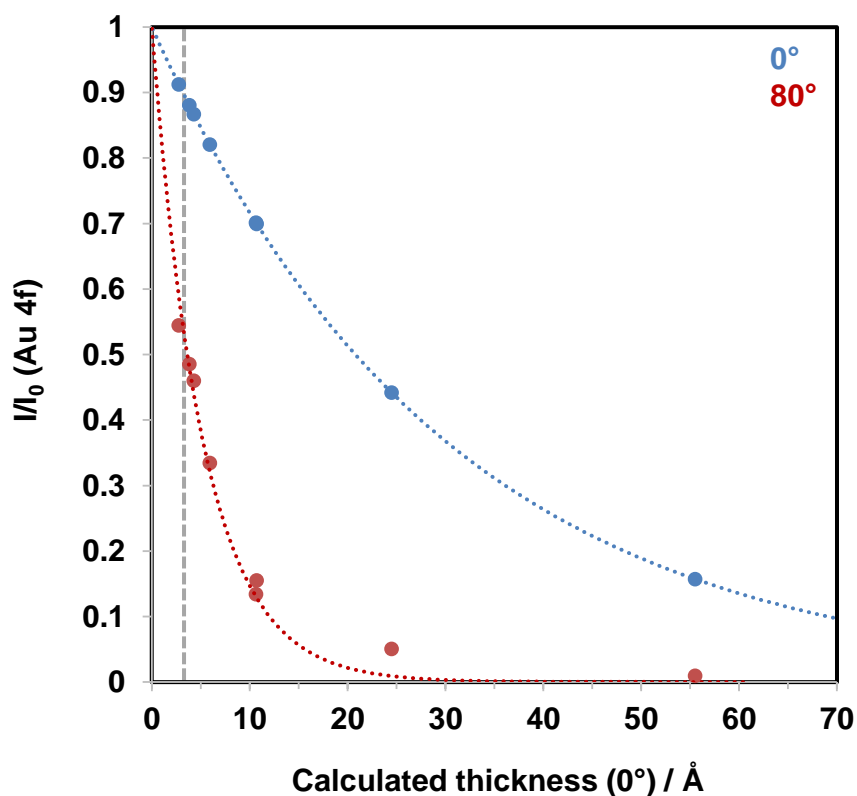


Figure 4.15: Attenuation of the Au 4f substrate signal with increasing IL coverage in  $0$  and  $80^\circ$  emission. The dashed lines represent the expected behavior for 2D layer-by-layer growth. The grey dashed line indicates a  $[\text{C}_2\text{C}_1\text{Im}][\text{EtOSO}_3]$  coverage of 1 ML (= one closed ion layer).

Upon IL deposition, stronger attenuation of substrate signals is observed in  $80^\circ$  due to the higher surface sensitivity, manifesting in a steeper exponential decrease of the red curve. For low coverages up to about 2 ML, the  $80^\circ$  data points perfectly coincide with the dashed line representing the expected behavior for 2D layer-by-layer growth. Note: For 2D growth the attenuation of the Au 4f signals should evolve in a sectionwise linear fashion during the completion of one layer (i.e. completion of each layer before the growth of a new layer begins);<sup>46</sup> due to the small number of data points, this behavior cannot be resolved here. For higher

coverages, deviations from the dashed line are found. As discussed by Cremer et al., these slight deviations in  $80^\circ$  geometry do not necessarily indicate the onset of 3D growth, but can most likely be explained by non-negligible elastic scattering contributions in  $80^\circ$  emission.<sup>46</sup> For systems with pronounced 3D growth, like  $[\text{C}_1\text{C}_1\text{Im}][\text{Tf}_2\text{N}]$  on carbonaceous supports (cf. chapter 3) or  $[\text{C}_8\text{C}_1\text{Im}]\text{Cl}$  on Au(111) (cf. chapter 4.1), the deviations in  $80^\circ$  of the measured attenuation of substrate signals from the expected behavior for 2D growth are observed already at lower coverages and are additionally much stronger. Thus, for  $[\text{C}_2\text{C}_1\text{Im}][\text{EtOSO}_3]$  on Au(111), 2D growth up to the highest measured coverage of 8.2 ML is clearly indicated by XPS.

#### 4.2.5. Influence of Surface Carbon on $[\text{C}_2\text{C}_1\text{Im}][\text{EtOSO}_3]$ Thin Films on Au(111)

Carbonaceous species adsorbing and reacting with the catalyst surface under reaction conditions lead to the formation of amorphous carbon residues which might influence the IL adsorption and wetting behavior of a SCILL catalyst. As discussed in chapter 3 for  $[\text{C}_1\text{C}_1\text{Im}][\text{Tf}_2\text{N}]$  thin films deposited on HOPG, the IL-carbon interactions are rather weak, resulting in pronounced 3D island growth. Improved wetting – almost comparable to Ni(111) – was found for  $[\text{C}_1\text{C}_1\text{Im}][\text{Tf}_2\text{N}]$  deposited onto single layer graphene/Ni(111), which was explained by the so-called wetting transparency of graphene.<sup>114</sup>

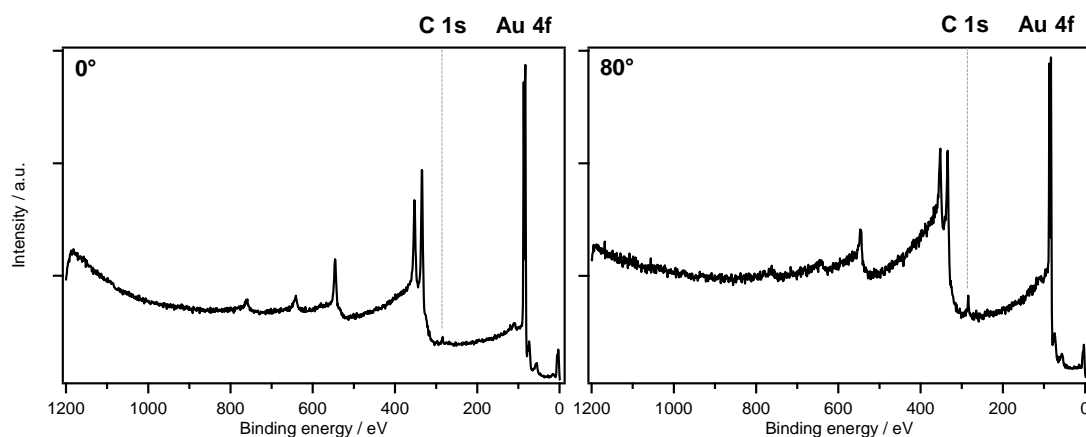


Figure 4.16:  $0$  and  $80^\circ$  overview spectra of the Au(111) surface after heating the sample with an adsorbed IL film. Besides the typical Au signals, also C 1s is clearly visible, indicating the presence of carbon at the surface.

To investigate the influence of carbon impurities on the IL growth behavior, a thin macroscopic film of  $[\text{C}_2\text{C}_1\text{Im}][\text{EtOSO}_3]$  was carbonized on a Au(111) support by heating the crystal to 900 K. After this procedure, a change in optical reflectivity could even be observed by visual inspection. As shown in Figure 4.16, the presence of carbon at the surface was confirmed by ARXPS, whereas no other IL signals could be detected. Quantitative analysis yielded an amount of 2.5 % carbon in bulk sensitive  $0^\circ$  emission. In case of a homogeneous carbon distribution at the Au surface, an enhancement of the C 1s intensity by the factor of  $\sim 6$  (i.e.,  $1/\cos(80^\circ)$ ) would be expected in surface sensitive  $80^\circ$  emission ( $\cong 15\%$  carbon). However, only a carbon content of 9 % was measured with ARXPS indicating the formation of a non-homogeneous carbon layer after the carbonization step.

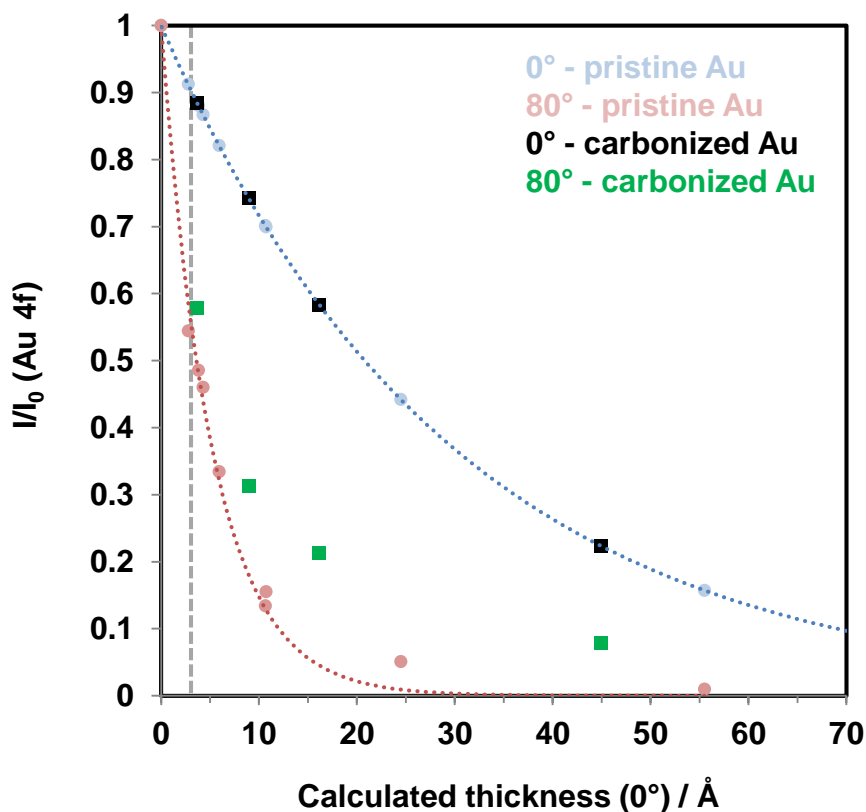


Figure 4.17: Attenuation of the Au 4f substrate signal with increasing IL coverage in 0 and  $80^\circ$  emission for IL deposition onto a carbonized Au surface compared to deposition onto pristine Au(111). The dashed lines represent the expected behavior for 2D layer-by-layer growth. The grey dashed line indicates a  $[\text{C}_2\text{C}_1\text{Im}][\text{EtOSO}_3]$  coverage of 0.5 ML (= one closed ion layer).

$[\text{C}_2\text{C}_1\text{Im}][\text{EtOSO}_3]$  thin films were deposited onto the carbonized Au surface by means of IL-PVD. Due to the observed co-adsorption of decomposition product at low coverages, only films with heights  $> 0.5$  ML were prepared to analyze the IL

growth behavior on the modified surface. As shown in Figure 4.17, the attenuation of the Au 4f signal upon IL deposition is obviously influenced by the surface carbon contamination. Upon IL deposition, strong deviations of the measured  $80^\circ$  attenuation of the Au 4f substrate signal from the expected behavior in case of ideal 2D growth are observed. As this holds true already for relatively low coverages for which elastic scattering should not play a decisive role, the discrepancies can only be explained by pronounced 3D island growth.

Another important question in the context of SCILL catalysis is, whether and how the adsorption and wetting behavior of ILs on different substrates can be modified, e.g., by the pre- or postadsorption of a catalytically active metal. One example for a molecular adsorbate is cyclohexane on Ni(111), which can be switched from wetting to non-wetting by preadsorption of 0.34 ML potassium.<sup>162</sup> Similarly important is the reverse influence of the IL layer on the catalytic properties of the solid catalyst surface in SCILL systems, particularly, when near-surface alloys<sup>163</sup> of noble metal / transition metal catalysts such as Au/Pd alloys are involved. Ensemble effects (that is, a specific geometric configuration at the alloy surface, required for facilitating a particular catalytic process) and ligand effects (that is, the electronic modification of the catalytically active surface atoms by their environment)<sup>164</sup> can be influenced by additional interactions of the metal atoms with the IL layer. Pd is known to form surface alloys with Au preferentially at enriched in the surface<sup>165</sup> even at RT<sup>93</sup>. In case of Pd and imidazolium-based ILs, as employed in this work, one might envision carbene-type attractive interactions between Pd and imidazolium cations that could lead to a stabilization of Pd at the solid-liquid interface, and thus, to an interface-enrichment compared to the system without IL. In the extreme case, it is furthermore well possible under certain reaction conditions, that these attractive interactions even transform a SCILL catalyst to a SILP-like system by dissolution of active species from the solid surface into the IL film.<sup>166</sup>

After the basic PVD and ESID studies on ultrathin  $[\text{C}_2\text{C}_1\text{Im}][\text{EtOSO}_3]$  films on Au(111), the following detailed PVD experiments in combination with Pd deposition were performed with the thermally more stable IL  $[\text{C}_2\text{C}_1\text{Im}][\text{OTf}]$ . To obtain a better understanding of the factors driving the initial adsorption and wetting properties and in the search for possible ways for switching between different

behaviors, the influence of Pd on the adsorption and growth behavior of ultrathin  $[\text{C}_2\text{C}_1\text{Im}][\text{OTf}]$  films deposited on Au(111) was investigated. This material combination also is of interest for real hydrogenation SCILL catalysts, with high activity and selectivity.<sup>167, 168</sup> Both Pd and the IL were thermally deposited onto the gold substrate by means of PVD. Au(111) was chosen for best comparability with previous studies on the IL/metal interface.<sup>46, 56</sup> The influence of Pd on the adsorption and growth properties of the IL were studied with two different experimental approaches, that is, Pd was either deposited prior or subsequent to the deposition of the IL.

#### 4.2.6. Growth and Adsorption of $[\text{C}_2\text{C}_1\text{Im}][\text{OTf}]$ Thin Films on Pristine Au(111)

In Figure 4.18, the attenuation of the Au 4f substrate signals ( $I/I_0$ ) at  $0^\circ$  and  $80^\circ$  upon deposition of  $[\text{C}_2\text{C}_1\text{Im}][\text{OTf}]$  onto Au(111) is plotted versus nominal thickness, which was calculated from the calibrated flux of the PVD apparatus (see chapter 2.4.). The blue ( $0^\circ$ ) and red ( $80^\circ$ ) dotted lines indicate the attenuation for a homogeneously growing two-dimensional film according to Equation 1. Up to a nominal coverage of around 0.5 ML ( $3.4 \text{ \AA}$ ; dashed black vertical line), at both emission angles, the attenuation of the Au 4f signal follows the dotted lines (blue for  $0^\circ$  and red for  $80^\circ$ ), indicating a 2D layer-by-layer growth. This behavior indicates the formation of one closed ion layer in a checkerboard structure, with cations and anions adsorbed next to each other, with a coverage of 0.5 ML. Moreover, the atomic ratios of the measured IL signals (S 2p, C 1s, N 1s, O 1s, F 1s) determined by quantitative XPS analysis match the nominal IL stoichiometry within the margin of error ( $\pm 10 \%$ ), at  $0^\circ$  and also in surface sensitive  $80^\circ$  emission, ruling out the enrichment of one of the ionic species at the IL/vacuum interface. These findings imply the formation of a homogeneous wetting layer with a thickness of 0.5 ML, composed of anions and cations adsorbing next to each other in a checkerboard arrangement directly on Au(111).

For higher IL coverages, that is, above  $\sim 0.5$  ML, a drastic change of the wetting behavior is observed. As seen in Figure 4.18, the measured attenuation of the Au 4f

signal is much less pronounced than for the ideal 2D behavior, that is, the data points lie significantly above the blue ( $0^\circ$ ) and red ( $80^\circ$ ) dotted lines. This behavior clearly indicates the formation of 3D islands, probably on top of the initially formed wetting layer. From the ARXPS data, however, it cannot be completely ruled out that the wetting layer breaks apart with increasing amount of IL, and three dimensional IL islands are formed exposing partially the bare Au(111) surface. This growth behavior is very different to imidazolium [Tf<sub>2</sub>N] ILs, for which ideal layer-by-layer growth was observed for coverages up to at least 10 ML,<sup>46, 56</sup> but resembles the growth of [C<sub>8</sub>C<sub>1</sub>Im]Cl on the same substrate.<sup>56</sup>

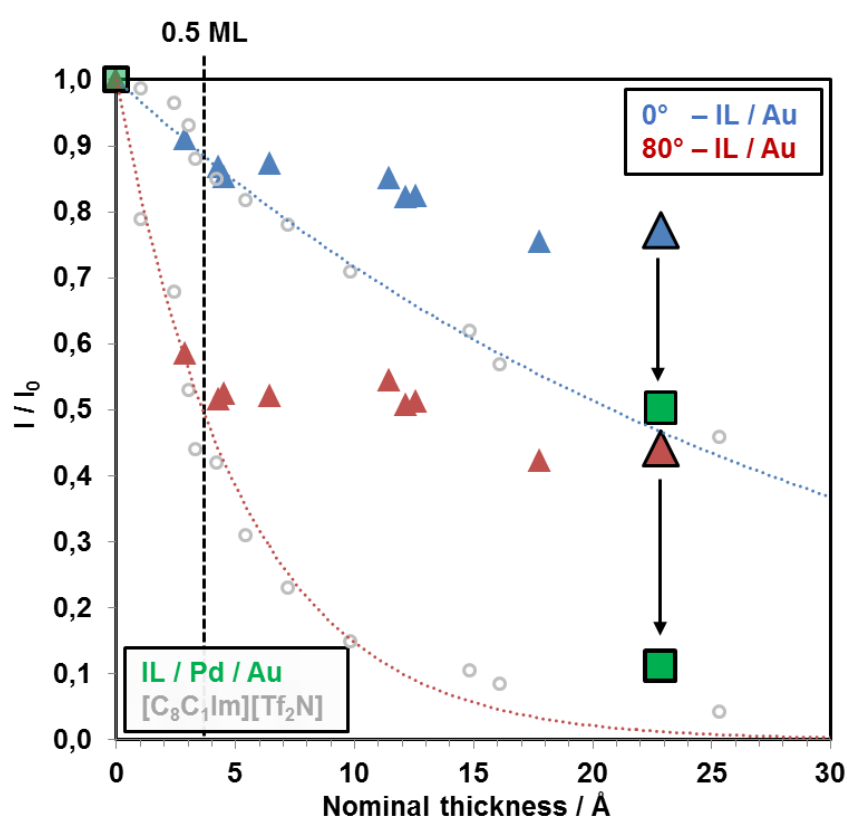


Figure 4.18: Attenuation of the Au 4f substrate signal with increasing nominal [C<sub>2</sub>C<sub>1</sub>Im][OTf] film thickness in 0 and 80° emission. The dashed lines represent the expected behavior for 2D layer-by-layer growth. 1 ML of [C<sub>2</sub>C<sub>1</sub>Im][OTf] ion pairs corresponds to ~6.8 Å. The dashed line indicates an [C<sub>2</sub>C<sub>1</sub>Im][OTf] coverage of 0.5 ML (=one closed ion layer in the checkerboard arrangement). For comparison, ARXPS data for the IL [C<sub>8</sub>C<sub>1</sub>Im][Tf<sub>2</sub>N] are also shown; this IL is known to grow in a layer-by-layer mode on Au(111).<sup>46</sup> Green squares show the attenuation of Au 4f intensity after deposition of ~23 Å [C<sub>2</sub>C<sub>1</sub>Im][OTf] on Au(111) that was pre-covered with 1.6 Å (0.7 ML) Pd. All deposition steps were performed at RT.

A detailed discussion on factors such as interionic interaction strength influencing the growth mode of an IL was given in chapter 4.1. in order to explain

the different morphologies of  $[\text{C}_8\text{C}_1\text{Im}][\text{Tf}_2\text{N}]$  and  $[\text{C}_8\text{C}_1\text{Im}]\text{Cl}$  thin films deposited on Au(111). At first glance, the molecular structures of  $[\text{OTf}]^-$  and  $[\text{Tf}_2\text{N}]^-$  anions share obvious similarities. However, their corresponding interaction energies with a dialkylimidazolium cation differ drastically, as evaluated by Fernandes et al. in an ESI-MS-MS and quantum chemical calculation study. The dissociation energy of  $[\text{C}_4\text{C}_1\text{Im}][\text{OTf}]$  was found to be 3.42 eV, which lies just in between the values determined for  $[\text{C}_4\text{C}_1\text{Im}]\text{Cl}$  (3.85 eV) and  $[\text{C}_4\text{C}_1\text{Im}][\text{Tf}_2\text{N}]$  (2.96 eV).<sup>150</sup> One reason for the higher dissociation energy of the  $[\text{OTf}]^-$  anion compared to  $[\text{Tf}_2\text{N}]^-$  is the smaller anion size, leading to an increase in hydrogen-bonding ability<sup>151</sup> and Coulomb interaction energy<sup>169</sup>. Hence, the relatively strong interionic interactions of  $[\text{C}_2\text{C}_1\text{Im}][\text{OTf}]$  might lead to reduced IL-substrate interactions and consequentially provoke the observed 3D growth behavior on Au(111).

#### 4.2.7. Influence of Pd Deposition on $[\text{C}_2\text{C}_1\text{Im}][\text{OTf}]$ Thin Films on Au(111)

In order to be able to study interfacial interactions of  $[\text{C}_2\text{C}_1\text{Im}][\text{OTf}]$  with Pd by means of surface-sensitive XPS, only thin IL films with a nominal coverage of  $\sim 3$  ML (which would correspond to a homogeneous film of 23 Å thickness) were deposited by PVD. Moreover, only very small nominal amounts of Pd in the sub-monolayer range were deposited by electron beam evaporation (1 ML Pd corresponds to  $\sim 2.3$  Å). In the following, two experiments will be discussed with a different order of deposition.

In the first experiment, nominally 1.6 Å ( $\sim 0.7$  ML) of Pd were deposited onto clean Au(111) and subsequently 23 Å ( $\sim 3$  ML) of  $[\text{C}_2\text{C}_1\text{Im}][\text{OTf}]$  on top (referenced to as “IL/Pd/Au”). In the second experiment, first nominally 23 Å of  $[\text{C}_2\text{C}_1\text{Im}][\text{OTf}]$  were deposited onto clean Au(111) and subsequently 1.6 Å of Pd on top (“Pd/IL/Au”). Note that the normalized Au 4f signals at  $0^\circ$  and  $80^\circ$  in Figure 4.18 after deposition of  $\sim 3$  ML IL (23 Å; enlarged blue and red triangles, respectively) onto clean Au(111) lie significantly above the dashed lines for ideal 2D growth due to pronounced island formation.

For simplicity, the discussion on the Pd and Au signals will focus on the overlapping Pd 3d and Au 4d regions. Additional analysis of the separated Au 4f region was conducted (see appendix) and was in perfect agreement with the results obtained for Au 4d. Furthermore, as the Au 4d<sub>5/2</sub> signal coincides with the Pd 3d<sub>5/2</sub> signal (~335 eV BE), only the Au 4d<sub>3/2</sub> (~352 eV BE) and Pd 3d<sub>3/2</sub> signals (~340.5 eV BE) will be discussed.

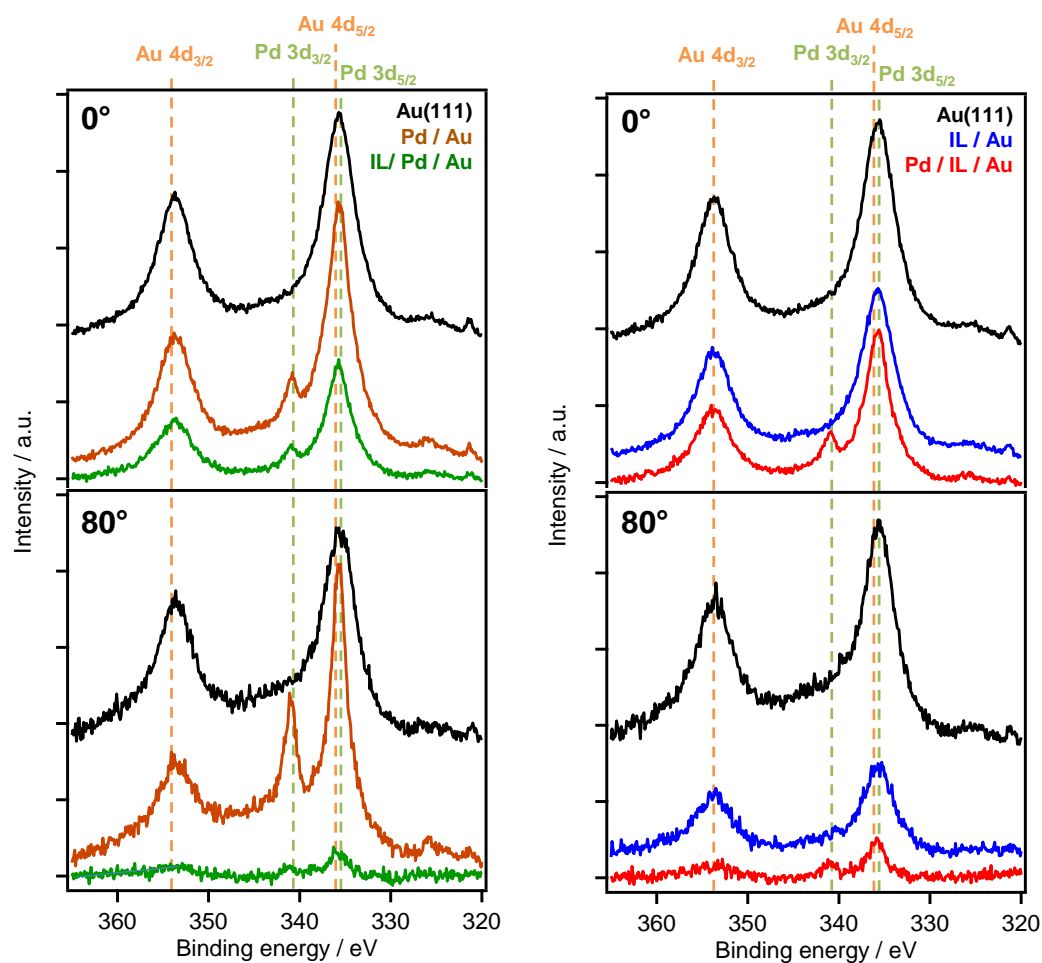


Figure 4.19: Bulk sensitive 0° (first row) and surface sensitive 80° (second row) spectra of the Au 4d/Pd 3d region for the sequence 1.6 Å (0.7 ML) Pd on Au(111) followed by deposition of nominally 23 Å (~3 ML) [C<sub>2</sub>C<sub>1</sub>Im][OTf] (left column) and the sequence 23 Å [C<sub>2</sub>C<sub>1</sub>Im][OTf] on Au(111) followed by the deposition of 1.6 Å Pd (right column). All experiments were carried out at RT. Note that the Pd 3d<sub>5/2</sub> signal superimposes with the Au 4d<sub>5/2</sub> signal; thus, only the corresponding discriminable d<sub>3/2</sub> signals are discussed.

Figure 4.19 shows 0° and 80° XP spectra of the Au 4d/Pd 3d region for the two deposition series. The black spectra correspond to the clean Au(111) surface. Upon the deposition of Pd onto clean Au(111) of the sequence “IL/Pd/Au”, a decrease of the Au 4d<sub>3/2</sub> intensity at 352 eV by ~9 % is observed in normal emission, which is accompanied by the appearance of the Pd 3d<sub>3/2</sub> signal at 340.5 eV in the orange

spectra in Figure 4.19 (left). Application of Equation 4 to the attenuation of the Au 4d<sub>3/2</sub> signal at 0° yields the expected thickness of the Pd layer of ~1.6 Å. In contrast, for the 80° data a nominal Pd layer thickness of only ~1.0 Å is calculated, resulting from a significantly lower attenuation than expected for a homogenous Pd adlayer. This effect is attributed to pronounced surface alloy formation of Pd with Au already discussed above, which was observed in a combined LEIS, XPS and AES study on PVD-deposited Pd on Au(111) in UHV.<sup>93</sup> Segregation of Au to the surface or diffusion of Pd into the subsurface results in pseudomorphic growth of a Pd-Au alloy on Au(111).<sup>93</sup>

The subsequent deposition of nominally 23 Å IL onto the Pd-Au surface alloy leads to a pronounced attenuation of both Au 4d and Pd 3d intensity, as is evident from the green spectra in Figure 4.19 (left), and the corresponding green squares in Figure 4.18. The measured attenuation is very close to that expected for two-dimensional growth (dotted lines), which is attributed to strong interactions of the IL with Pd surface atoms. This contrasts the behavior upon deposition of 23 Å [C<sub>2</sub>C<sub>1</sub>Im][OTf] onto the pristine Au(111) surface; see blue spectra in Figure 4.19 (right). This change is also evident from Figure 4.18, where the black vertical arrows indicate the enhanced attenuation in case of predeposited Pd.

An overall similar behavior, confirming an attractive interaction between [C<sub>2</sub>C<sub>1</sub>Im][OTf] and Pd, is observed in the reverse experiment “Pd/IL/Au”, in which first the IL is deposited onto clean Au(111), forming 3D islands on the surface; see blue spectra in Figure 4.19 (right). Upon subsequent evaporation of Pd, the attenuation of Au substrate signals in the red spectra in Figure 4.19 (right), in particular at 80°, is significantly stronger than expected from the deposition of only 1.6 Å of Pd on top of the IL. This stronger attenuation is attributed to an increased wetting of the substrate with the IL, induced by the additional presence of Pd.

The transition from 3D islands towards a homogeneous IL film is further supported by an increase of IL signals after Pd deposition, as is exemplarily shown in Figure 4.20 for the imidazolium N 1s peak (red vs. blue spectra). The IL signal increase upon Pd deposition is more pronounced in the surface-sensitive 80° emission. The red spectrum at 0° shows a shoulder, shifted to lower BE by 1.8 eV relative to the main peak, which is absent at 80°. It therefore originates not from the IL/vacuum interface but from the buried IL/Au-Pd interface region. The peak could

be due to a charge transfer between the  $[\text{C}_2\text{C}_1\text{Im}]^+$  cation and Pd, leading to a more neutral – possibly carbene-like – species. Interestingly, this low BE shoulder present for imidazolium cations at the IL-metal interface is only detectable in the sequence “Pd/IL/Au” and is absent for “IL/Pd/Au” when the IL is deposited onto the Pd/Au alloy (Figure 4.20, green spectra). Apparently, isolated Pd atoms that are only available upon deposition of Pd in the “Pd/IL/Au” experiment are more reactive than Pd atoms already incorporated in the alloy surface.

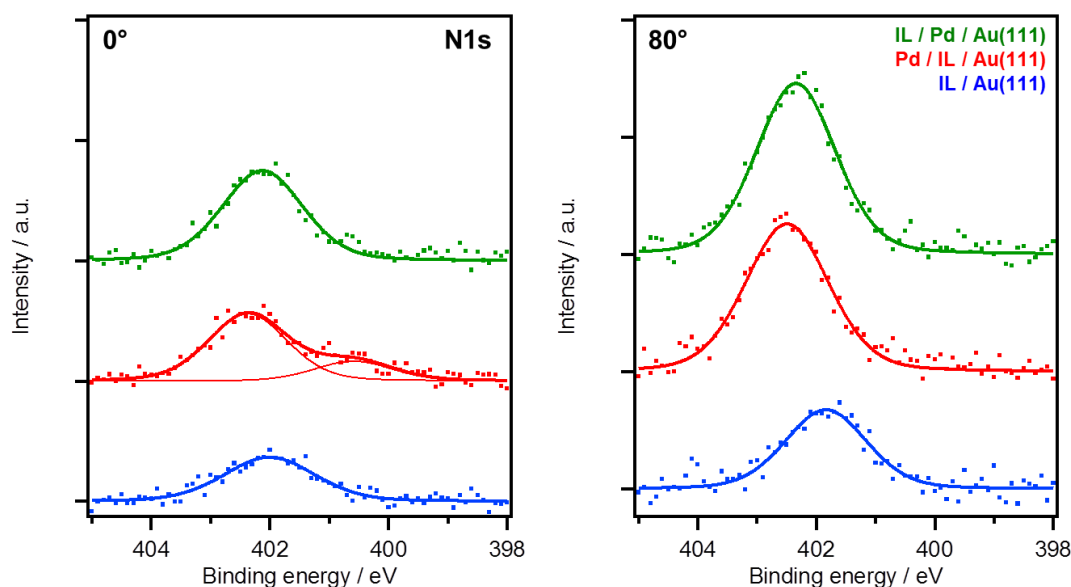


Figure 4.20:  $0^\circ$  (left) and  $80^\circ$  (right) N 1s spectra of the imidazolium ring N atoms of the two series. Colors correspond to spectra of Figure 4.19: deposition of 23 Å IL on Au(111) (blue), followed by Pd deposition (red) in comparison of 23 Å IL deposited onto 1.6 Å Pd/Au(111) (green).

Notably, for both sequences, that is, “IL/Pd/Au” and “Pd/IL/Au”, quantitative XPS analysis on the IL-related signals did not reveal any significant enrichment of any of the measured IL species in surface sensitive  $80^\circ$  emission (not shown), indicating a random distribution of both, anions and cations at the IL/vacuum interface.

In Figure 4.21, a direct comparison of the  $0^\circ$  and  $80^\circ$  spectra of the Au 4d/Pd 3d region after the deposition sequences IL/Pd/Au (green) and Pd/IL/Au (red) is shown. At  $0^\circ$ , the overall intensity of both metal substrate signals is somewhat larger for Pd/IL/Au, due to a less pronounced 2D film formation (wetting) for this deposition sequence. At  $80^\circ$ , in line with the  $0^\circ$  data, the overall intensity is also larger for the Pd/IL/Au sequence, but for the Pd  $3d_{3/2}$  signal at 340.5 eV this effect

is significantly more pronounced. This enhanced Pd intensity could be an indication for the partial suppression of surface alloying in the presence of the IL for the Pd/IL/Au sequence, possibly due to the strong interactions of single Pd atoms with  $[C_2C_1Im]^+$  cations discussed above. In the context of heterogeneous catalysis using the SCILL concept, these results directly provide a possible explanation on the molecular level for the beneficial influence of the IL layer in case of heterogeneous metal alloy catalysts.

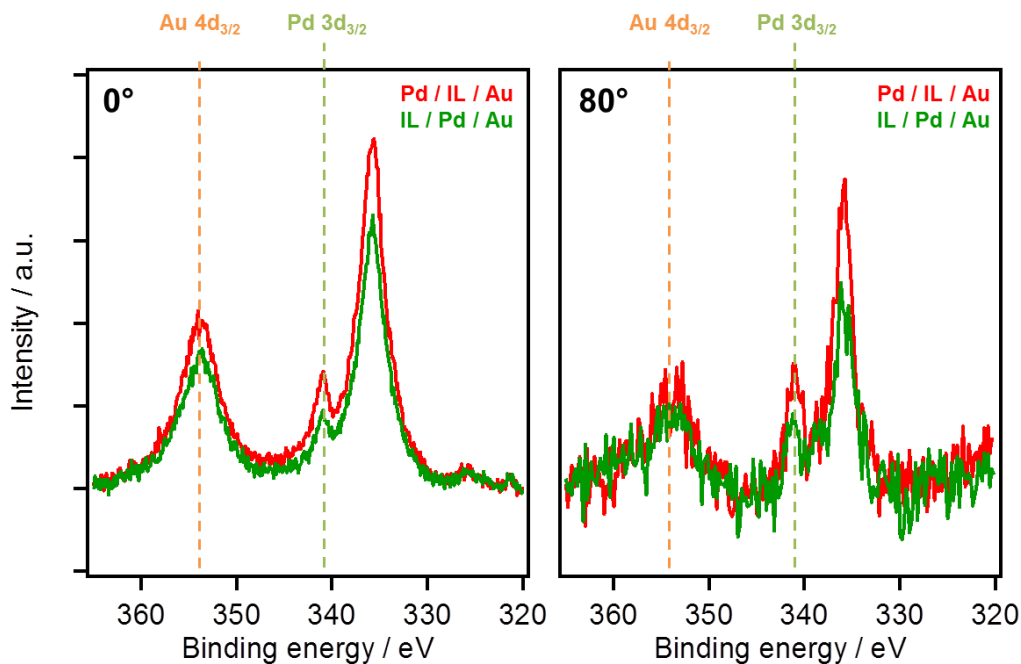


Figure 4.21: Direct comparison of the  $0^\circ$  and  $80^\circ$  spectra of the Au 4d/Pd 3d region after the final deposition steps of both sequences, that is, IL/Pd/Au (red) and Pd/IL/Au (green); only core levels unambiguously attributed to Au and Pd are marked and discussed in the text. Note: The  $80^\circ$  spectra have been modified by averaging over two data points to improve signal-to-noise ratio.

The different scenarios upon IL deposition on Au(111) and for pre- and postdeposition of Pd are summarized in Figure 4.22. The left panel a shows the pronounced 3D growth, that is, non-wetting of the IL on Au(111). The center panel b indicates the 2D layer-by-layer growth, that is, wetting the IL, induced by predeposited Pd, that is, on a PdAu surface alloy. The right panel c shows the situation after postdeposition of Pd onto the IL film a. As for predeposited Pd, a transition towards 2D growth is observed, albeit less pronounced. In addition, upon Pd postdeposition, surface alloying of Pd and Au seems to be suppressed, most likely due to a significant interaction of the IL cations with more reactive surface Pd atoms.

An interesting question in this context is, whether surface alloying in the here studied SCILL-type model system is also hindered by an IL film at elevated temperatures, that is, closer to the operation conditions of a real catalyst; this is however out of the scope of the present study, and will be addressed in future experiments. Notably, for the catalytic dehydrogenation of liquid organic hydrogen carriers, it could already be shown that UHV model IL systems can come very close to real reaction conditions.<sup>170</sup>

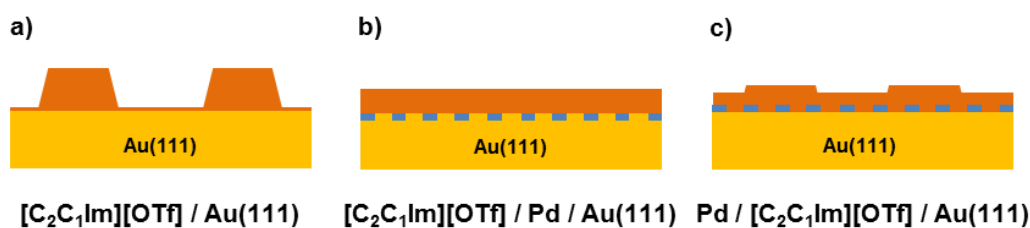


Figure 4.22: Scheme of the suggested interface morphologies of a)  $[C_2C_1Im][OTf]$  deposited onto pristine Au(111), b)  $[C_2C_1Im][OTf]$  deposited onto a Pd-Au surface alloy (sequence IL/Pd/Au, and c) deposition of Pd onto the predeposited IL film (sequence Pd/IL/Au). Color code: yellow = Au(111) substrate, orange =  $[C_2C_1Im][OTf]$ , blue = Pd atoms.

#### 4.2.8. Summary and Conclusions

In the context of surface science studies on model systems for SCILL catalysts, the interaction of a model IL adsorbed on clean and modified Au(111) by ARXPS was investigated and evaluated potential routes to switch the growth behavior by pre- or postdeposition of Pd atoms. On clean Au(111), it was found that upon thermal deposition of  $[C_2C_1Im][OTf]$  in the submonolayer range, the IL adsorbs in a checkerboard arrangement with cations and anions located next to each other. This initial behavior is similar to that observed for [dialkylimidazolium][Tf<sub>2</sub>N] ILs on the same substrate, where a 2D wetting layer with a thickness of up to 0.5 ML is formed.<sup>46 56</sup> For coverages above 0.5 ML, the onset of pronounced 3D growth occurs. This behavior contrasts the layerwise growth found for [dialkylimidazolium][Tf<sub>2</sub>N] ILs on Au(111), and is attributed to stronger cation-anion interactions in case of the smaller  $[OTf]^-$  anion. By depositing small amounts of Pd before or after the deposition of the IL, a strongly improved wetting behavior was observed. This finding is attributed to attractive interactions between  $[C_2C_1Im][OTf]$  and Pd surface atoms that allow for switching the growth mode

from 3D to 2D. For Pd deposition subsequent to the deposition of the IL, the ARXPS data revealed particularly strong interactions between the dialkylimidazolium cation and single Pd atoms, which seem even to be strong enough to prevent surface alloying of Pd and Au, which occurs at RT in absence of the IL.<sup>93</sup> This stabilization mechanism might be one key player in the catalytic cycles of corresponding Pd containing SCILL catalysts.





## 5. Surface Properties of Pd-Ga and Pt-Ga Alloys

Besides IL-based systems such as SILP or SCILL, there are other promising catalytic concepts involving liquids of negligible vapor pressure, including highly stable and selective intermetallic compounds, whose functionality is not fully understood yet. One catalytically active class of intermetallics are Pd-Ga species, which have shown to be particularly active in regards of catalyzing hydrogenation and dehydrogenation reactions, as for instance the selective hydrogenation of  $C_2H_2$  to  $C_2H_4$ , or methanol steam reforming.<sup>171</sup> Allam et al. could show that the enthalpy of formation for Pd-Ga compounds is negative<sup>172</sup> and – as Pd and Ga are chemically very different metals – the reaction between both results in the formation of pronounced covalent bonds. In contrast to alloys, which mainly exhibit metallic bonding, covalent bonds strongly alter the crystal and the electronic structure<sup>171</sup> giving rise to rather complex phase diagrams<sup>173</sup> (cf. Figure 5.1). Investigating the surface properties of Pd-Ga intermetallic compounds is of vital interest for understanding related catalytic reactions. A combined FTIR, XPS and SEM study by Kovnir et al. revealed the presence of very stable catalytically active isolated Pd atoms on the surface of PdGa, which form the basis for the high selectivity and long-term stability of PdGa in the semi-hydrogenation of  $C_2H_2$  to  $C_2H_4$ . Moreover, the Pd d-states were found to be highly modified due to covalent bonding between Pd and Ga.<sup>172</sup> A study by Wowsnick et al. focused on the surface stability of Pd<sub>2</sub>Ga, another Pd-Ga intermetallic compound, showing high selectivity in the hydrogenation of  $C_2H_2$ . This work shows that the covalent bonds between Pd and Ga are not strong enough to protect the material's surface from oxidation. Independent of the degree of oxidation, formation of metallic Pd at the surface was found, which explains the material's ability to activate hydrogen.<sup>171</sup>

A novel approach is based on the concepts described above but differs on the Pd-Ga ratio: Conventional porous carriers (like  $Al_2O_3$ ,  $SiO_2$  or carbonaceous supports) are coated with a low-melting-point metal Ga containing only small amounts of the catalytically active noble metal Pd. Besides the economic advantage of a precious catalyst being dispersed in the inexpensive Ga layer, the high mobility

of the liquid Ga phase in the temperature range during operation might be beneficial, too. The mobility of the liquid Ga layer might function as a self-cleaning mechanism, leading to an enhanced lifespan of the catalyst. As seen in the phase diagram depicted in Figure 5.1, for catalytically active Pd-Ga intermetallic compounds known from literature, such as GaPd or GaPd<sub>2</sub>, the melting point is drastically increased compared to pure Ga. Prototype catalysts based on this novel concept have been developed for the dehydrogenation of the liquid organic hydrogen carrier (LOHC) dodecahydro-N-ethylcarbazole (12H-NEC) by the chair of Chemical Reaction Engineering at the University of Erlangen-Nürnberg.<sup>174-176</sup> The main disadvantages of the “green” fuel hydrogen are its low energy density and safety issues. One idea to solve these problems is the LOHC concept, based on organic molecules, which can be loaded and unloaded with hydrogen. But before LOHC’s can become a serious alternative to conventional fuels, efficient catalysts are required for loading and unloading hydrogen under relatively mild conditions.<sup>173</sup>

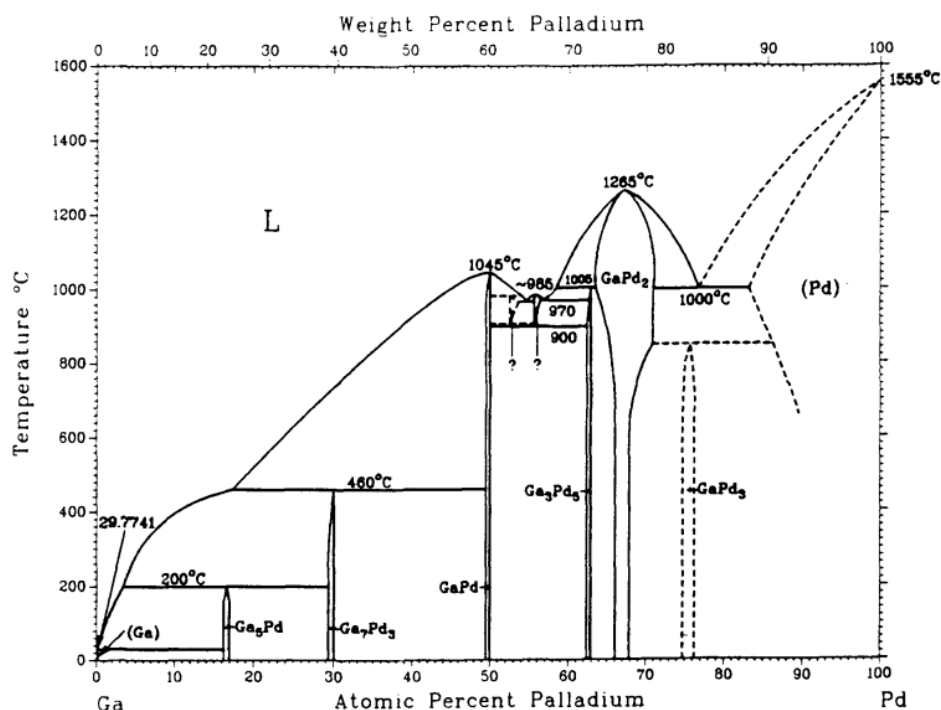


Figure 5.1: Pd-Ga phase diagram. Taken from reference<sup>177</sup>.

Besides Pd-Ga intermetallic compounds, also Pt-Ga systems are investigated with respect to their catalytic activity. The phase diagram of the binary system is depicted in Figure 5.2. As for Pd-Ga also for Pt-Ga the enthalpy of formation of the intermetallic compounds is negative.<sup>156</sup> In literature, Ga<sub>2</sub>O<sub>3</sub> is reported to promote

the catalytic activity of a Pt/WO<sub>3</sub>/ZrO<sub>2</sub> catalyst used for the isomerization of n-heptane. The effect was attributed to an enhancement of Brønsted acidity and a changed ratio of Brønsted to Lewis acidity.<sup>157</sup> Several studies focus on the promotion of alumina-supported Pt based dehydrogenation catalysts by the addition of Ga. These catalysts are used for the selective dehydrogenation of propane (C<sub>3</sub>H<sub>8</sub>) to propylene (C<sub>3</sub>H<sub>6</sub>). It could be shown that the selectivity to C<sub>3</sub>H<sub>6</sub> is enhanced by the addition of Ga. Further, catalyst deactivation and carbon formation is reduced with increasing Ga content. Ga appeared to have a very low effect on the acidity function of the alumina support, but it modifies the structure of the metallic phase.<sup>75, 81, 82</sup> Another study by Sattler et al. described an alumina-supported Pt-Ga based catalyst for the selective dehydrogenation of C<sub>3</sub>H<sub>8</sub>. The authors also reported on synergetic catalytic effects between Ga and Pt, resulting in a highly active and stable catalyst. Moreover, they found an inverse bifunctional active phase in which coordinately unsaturated Ga<sup>3+</sup> ions are the active species and Pt acts as a promoter.<sup>98</sup>

The XPS experiments presented in this work aim at a fundamental understanding of the surface composition of low Pd content Pd-Ga alloys. Also the effect of oxidation on the surface composition might play a decisive role, as the presence of oxidizing agents cannot be prevented completely under real reaction conditions. For this purpose, Pd was deposited onto a Ga film with a native oxide layer and analyzed by XPS (chapter 5.1). Further, the surface composition of an ex-situ prepared Pd-Ga alloy with 0.25 at% Pd was analyzed by XPS (chapter 5.2). In chapter 5.3., XP spectra of porous carbon and SiO<sub>2</sub>-supported Pd-Ga coated catalysts, developed for the dehydrogenation of 12H-NEC, are discussed. Moreover, first experiments towards a fundamental understanding of the surface properties and the effect of oxidation on the surface composition of Pt-Ga intermetallic compounds were performed (chapter 5.4). For the quantitative analysis of the XPS data, adapted literature ASF values determined by Wagner<sup>98</sup> were applied (Ga 2p<sub>3/2</sub>: 6.35, Ga 3d: 0.22, Pd 3d: 3.9; cf. section 2.4 for details).

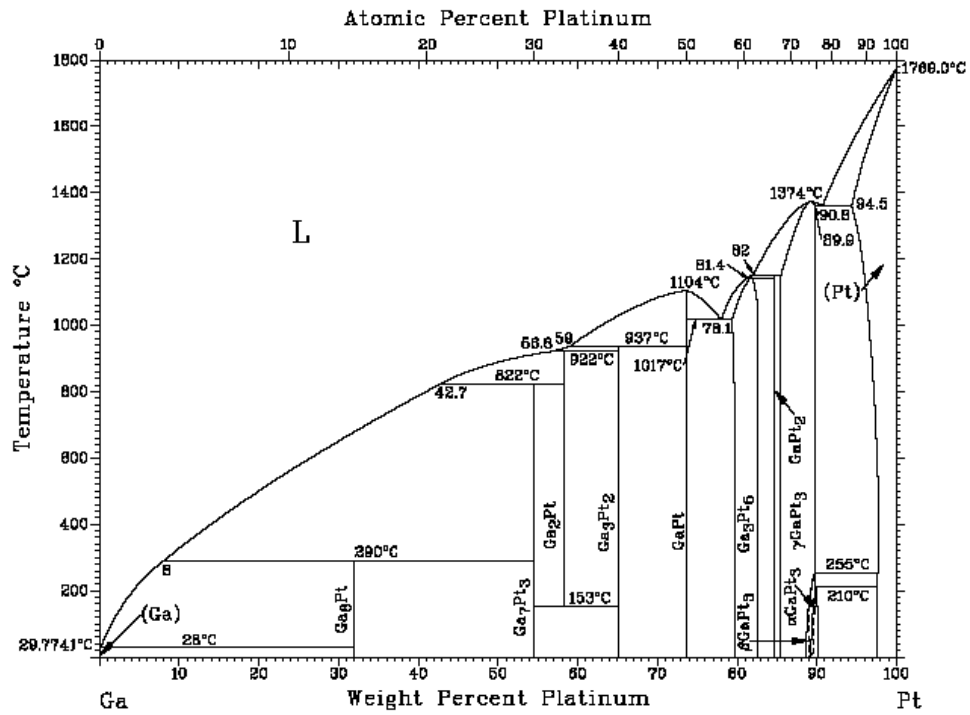


Figure 5.2: Pt-Ga phase diagram. Taken from reference<sup>177</sup>.

## 5.1. Pd Deposition onto Ga<sub>2</sub>O<sub>3</sub> / Ga

To obtain an understanding of the Pd/Ga<sub>2</sub>O<sub>3</sub>/Ga interface and to examine the stability of Pd on an oxidized Ga surface, ultrathin Pd films were deposited by physical vapor deposition onto a macroscopic Ga film with a thickness of roughly 0.5 mm spread ex-situ on a Suprasil quartz glass support. The Ga film was only hardly wetting the glass surface, leading to a corrugated film morphology. After introduction into the UHV chamber, XPS revealed the presence of traces of carbonaceous impurities, which were removed by sputtering the sample with Ar<sup>+</sup> ions for 10 min at a temperature of 320 K to ensure maintaining the liquid state of the Ga film ( $p_{\text{Ar}} = 5 \times 10^{-6}$  mbar;  $I_{\text{emis}} = 10$  mA). After this mild sputtering procedure, XPS could validate the persistent presence of a thin native oxide layer at the sample surface. Besides gallium and oxygen no more other elements were visible in the 0 and 80° overview spectra (not shown). Besides O 1s, two Ga core levels have been analyzed by XPS: Ga 2p and Ga 3d. Due to the large doublet separation of 27 eV for Ga 2p, only the Ga 2p<sub>3/2</sub> contribution at around 1120 eV was recorded throughout this work. The doublet separation of Ga 3d at around 20 eV binding energy, however, is only 0.5 eV and cannot be resolved with the experimental setup. The two signals, observed in both of the Ga regions (cf. black spectra in Figure 5.3), is therefore attributed to a chemical shift, namely the presence of metallic Ga (1117 and 19 eV for Ga 2p<sub>3/2</sub> and Ga 3d, respectively) and Ga<sup>3+</sup> in Ga<sub>2</sub>O<sub>3</sub> (1119 and 21 eV for Ga 2p<sub>3/2</sub> and Ga 3d, respectively). The large difference in BE between Ga 2p and Ga 3d of nearly 1100 eV allows for interesting conclusions on the depth profile of a Ga film, even without changing the emission angle, as required for ARXPS. The IMFP of low BE, that is, high kinetic energy Ga 3d photoelectrons is about three times larger than that of electrons originating from the high BE Ga 2p<sub>3/2</sub> orbital (30.7 vs. 11.2 Å).<sup>178</sup> By comparing the ratios of the metallic to the oxidic contributions of the Ga 3d and Ga 2p core levels, the influence of the strongly differing IMFPs becomes clearly evident: Whereas Ga<sup>0</sup> is expected to be found in the bulk, Ga<sup>3+</sup> should be located at the surficial oxide layer. Consequentially, compared to Ga 3d, in both emission angles strong enhancements of the oxidic relative to the metallic contributions are observed for Ga 2p<sub>3/2</sub> electrons originating from the first atomic layers only.

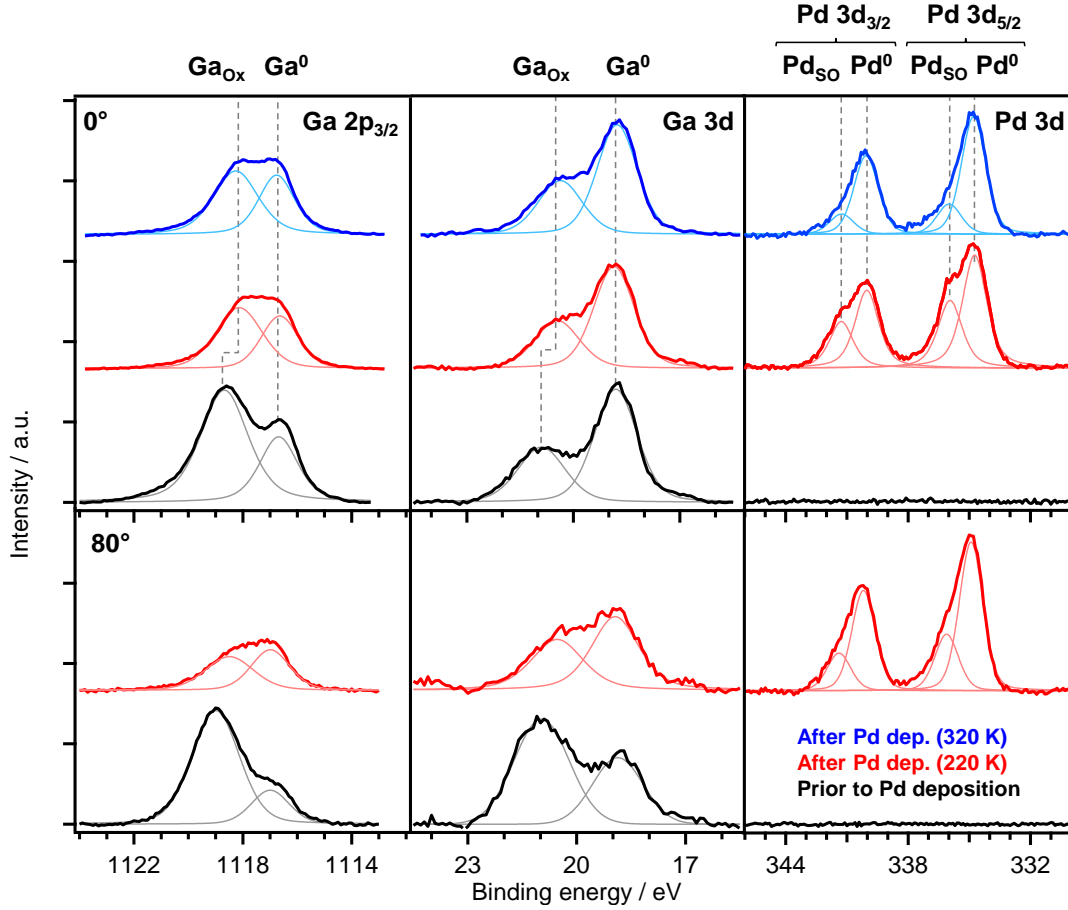


Figure 5.3: Normal and 80° emission spectra of a 1 mm thick Ga film spread on quartz glass (covered by an oxide layer): Prior to Pd deposition (recorded at  $T = 320$  K; black), after Pd deposition at 220 K (recorded at  $T = 220$  K; red) and after mild heating (recorded at  $T = 320$  K; blue). Blue 80° spectra are missing due to complete dewetting when tilting the molten sample in grazing emission.

Quantitative XPS analysis (utilizing the  $\text{Ga}_{\text{Ox}}$  3d and O 1s intensities) confirms the composition of the oxide layer being  $\text{Ga}_2\text{O}_3$  (calculated composition:  $\text{Ga}_2\text{O}_{2.9}$ ). The thickness  $d$  of the oxide layer was estimated by equation 6,<sup>179</sup>

$$d = \lambda_{i,\text{Ga}_2\text{O}_3} \cdot \cos \vartheta \cdot \ln \left[ \frac{I_{i,\text{ox}} \cdot \lambda_{i,\text{Ga}} \cdot N(\text{Ga})_{\text{Ga}}}{I_{i,\text{met}} \cdot \lambda_{i,\text{Ga}_2\text{O}_3} \cdot N(\text{Ga})_{\text{Ga}_2\text{O}_3}} + 1 \right] \quad (6)$$

based on the XPS intensities  $I_i$  of the metallic and the oxidic components in the Ga 2p<sub>3/2</sub> and Ga 3d region (cf. Figure 5.3, black spectra); with  $\lambda_i$  being the IMFP of the respective photoelectrons and  $N(\text{Ga})$  being the Ga atom density in pristine Ga and  $\beta\text{-Ga}_2\text{O}_3$ , respectively. For the 0° data, application of equation 6 yields similar thicknesses of 12.4 and 15.1 Å of the oxide layer derived from Ga 2p<sub>3/2</sub> and Ga 3d, respectively. For the 80° data, significantly lower values of 3.0 and 5.7 Å are obtained. As equation 6 is only applicable to flat and homogeneous layer systems, the deviations are ascribed to the corrugated morphology of the Ga film, falsifying

the values calculated from the 80° data. Despite these uncertainties impeding an absolute quantitative analysis, a trend towards higher surface sensitivity in the 80° data is proven by the higher ratio of the oxidic components of the Ga 2p and Ga 3d signals. Therefore, the discussion will include some observations of the 80° data, however, will mainly focus on the 0° measurements.

Prior to the deposition of Pd, the sample was cooled with liquid N<sub>2</sub> to 220 K. According to the calibration, performed by depositing small amounts of Pd onto a clean Au(111) single crystal (cf. section 2.4 for details), the thickness of the Pd layer after 15 min of evaporation was expected to be around 5 Å. When making a rough estimate of the thickness of one atomic layer of Pd by considering the molar volume according to equation 5, 5 Å correlate to a coverage of roughly two layers of Pd. Calculation of the thickness by monitoring the attenuation of the total Ga 3d and Ga 2p<sub>3/2</sub> intensities (according to equation 4) yielded values of 5.5 and 5.8 Å, respectively. The small difference can be explained by additional C species, adsorbed on the cooled and also more reactive Pd surface. The resulting additional substrate attenuation leads to the slightly larger calculated Pd thickness. Interestingly, a significant decrease of the Ga<sup>3+</sup> component is observed in the XP spectra after Pd deposition, particularly in the surface sensitive Ga 2p<sub>3/2</sub> and in the 80° Ga 3d spectra, i.e. at the Pd/Ga<sub>2</sub>O<sub>3</sub> interface. Additionally, a clear shift of the oxidic components of the Ga 2p and Ga 3d peaks by - 0.4 eV towards lower BE is observed, indicating a partial reduction of Ga<sup>3+</sup> upon Pd deposition. Vice versa there are two chemically inequivalent Pd species visible in the Pd 3d region in 0° emission, i.e. in the more bulk sensitive geometry: a main peak at low binding energy and a small shoulder at higher BE. The chemical shift between the main Pd 3d<sub>5/2</sub> peak at 335 eV, which can be assigned to metallic Pd, is + 1.1 eV. This value lies below the 1.4 – 1.5 eV shift, known from literature for bulk PdO,<sup>180, 181</sup> but matches the BE shift for surface Pd in contact with oxygen (Pd<sub>SO</sub>), as reported in a study by Titkov et al.<sup>181</sup> The shift of the second Pd species is therefore assigned to interfacial Pd atoms, which are interacting – and apparently also partly reducing the topmost Ga<sup>3+</sup> ions of the Ga<sub>2</sub>O<sub>3</sub> layer, as deduced from the surface sensitive Ga 2p<sub>3/2</sub> and 80° Ga 3d spectra. Unfortunately, complementary interpretation of the O 1s region is difficult, as there is an overlap of the O 1s peak at 531.6 eV and the Pd 3p<sub>3/2</sub> peak at 533.6 eV.

When heating the sample from 220 to 320 K where the Ga film becomes liquid, in accordance with the XPS data, the formation of Pd clusters is proposed, probably driven by an increased mobility of the deposited Pd atoms at the higher temperature. Data analysis (cf. blue spectra in Figure 5.3) revealed a decrease of the overall Pd 3d intensity of 18 %, but an increase of the overall Ga 3d intensity by 11 %. These findings can be explained by the agglomeration of Pd to clusters and the consequent uncovering of certain surface areas from Pd. Surprisingly, no distinct changes are observed with respect to the Ga 2p and Ga 3d peak shapes, i.e. the interfacial reduction of  $\text{Ga}^{3+}$ , initiated by the deposition of Pd, seems to be stable – at least in the reducing situation of the UHV environment. Despite the enduring presence of reduced Ga species at the surface, the  $\text{Pd}_{\text{SO}}$  intensity decreases significantly after heating to 320 K as shown by the disappearance of the high BE-shoulder in the Pd 3d core levels. Thus, the corresponding  $\text{PdO}_x$  species seems to remain at the interface after the cluster formation. However, with larger  $\text{Pd}^0$  islands on top, the  $\text{PdO}_x$  signal is attenuated more strongly. After heating the sample to 320 K, no  $80^\circ$  measurements could be performed due to complete dewetting of the Suprasil sample occurring when tilting the molten sample.

The scheme in Figure 5.4 illustrates the suggested structures of the interfacial region directly after Pd deposition at 220 K and after heating the sample to 320 K.

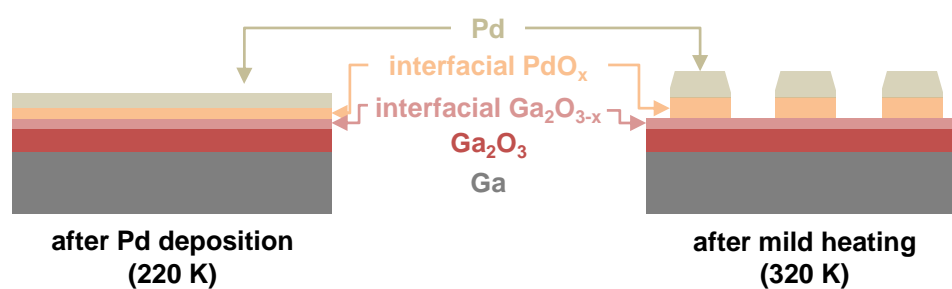
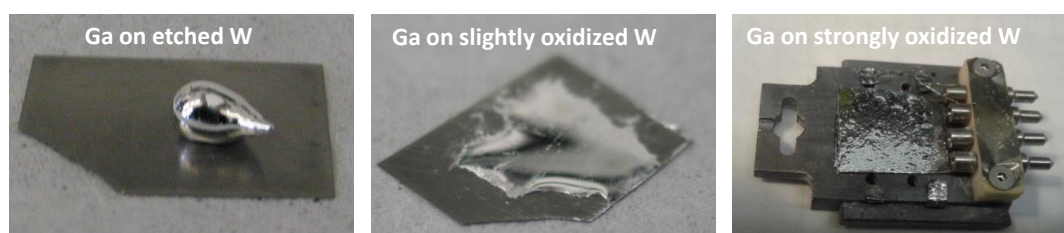


Figure 5.4: Scheme of the suggested structures of the interfacial Pd / Ga<sub>2</sub>O<sub>3</sub> region directly after Pd deposition at 220 K (left) and after heating the sample to 320 K (right).

## 5.2. Surface Composition of a Low Pd Content

### Pd-Ga Alloy

Having found that PVD-deposited Pd is stabilized on top of Ga<sub>2</sub>O<sub>3</sub> covered Ga – i.e. no pronounced diffusion of Pd into bulk Ga occurs – the surface composition of an ex-situ prepared low Pd content Pd-Ga alloy should be investigated for comparison. For this purpose, a Pd-Ga alloy with 0.25 at% Pd was prepared by sintering accurately weighed quantities of both metals under inert atmosphere in a flask. In a second step, a W foil heated in air was coated with the alloy by spreading it across the surface in the liquid state. Surface oxidation by treating the W foil with the hot air stream emitted from a heat gun, lead to an improvement concerning the wettability of the alloy compared to freshly etched W foil (see Figure 5.5 for pure Ga on W, which is showing the same behavior). Nevertheless, no completely homogeneous flat film could be prepared. The average height of the corrugated film was estimated to be in the order of 0.5 mm.



*Figure 5.5: Photographs of Ga on W foil. Left: No wetting of Ga on freshly etched W. Center: After oxidizing the substrate with the hot air stream emitted from a heat gun, improved wettability is observed. Right: After prolonged oxidation, further improved wettability allows for the preparation of a corrugated Ga film.*

The XP spectra shown in Figure 5.6 were recorded without any pretreatment like sputtering and at a sample temperature of 335 K to ensure the liquid state of the Pd-Ga alloy (cf. Figure 5.1). The surface-sensitive Ga 2p signal shows a stronger contribution of Ga<sup>3+</sup> relative to Ga(0) compared to the more bulk-sensitive Ga 3d level (cf. Figure 5.6), indicating the presence of a Ga<sub>2</sub>O<sub>3</sub> layer at the sample surface. The thickness of the oxide layer calculated by application of equation 6 was found to be 11.4 Å or 9.6 Å for Ga 2p<sub>3/2</sub> and Ga 3d, respectively. The Pd 3d BE is 336.6 eV, indicating the presence of bulk PdO according to literature.<sup>180, 181</sup>

Quantitative XPS analysis revealed a much higher Pd content than the nominal 0.25 at% in the bulk: 1.8 at% Pd were detected when comparing the bulk-sensitive Ga 3d intensity (Ga<sup>0</sup> and Ga<sub>Ox</sub>) to Pd 3d and a Pd content of 0.8 at% when

comparing the surface-sensitive Ga  $2p_{3/2}$  intensity ( $\text{Ga}^0$  and  $\text{Ga}_{\text{Ox}}$ ) to Pd 3d. In an unpublished near ambient pressure ( $p_0 = 1$  mbar) XPS study performed by Grabau at the Chair of Physical Chemistry II in Erlangen, it was shown that upon in-situ oxidation of Pd-Ga alloys with various Pd concentrations at elevated temperatures, with increasing  $\text{Ga}_2\text{O}_3$  layer thickness, Pd vanishes from the near surface region accessible by XPS. These results suggest that Pd is virtually absent in the growing surface oxide of the alloy. The significant enhancement of Pd signals observed in case of the native oxide presented in this work is therefore attributed to the enrichment of Pd at the  $\text{Ga}^0/\text{Ga}_2\text{O}_3$  interface. This assumption is confirmed by the comparison of the Pd 3d intensity with the corresponding  $\text{Ga}^0$  and  $\text{Ga}_{\text{Ox}}$  contributions of the Ga  $2p_{3/2}$  and Ga 3d signals, respectively. For the more bulk-sensitive  $\text{Ga}^0$  3d intensity, a Pd content of 1.2 at% is obtained, whereas in case of the more surface-sensitive  $\text{Ga}^0$   $2p_{3/2}$  intensity, the Pd content adds up to 4.5 at%. This observation implies an enrichment of Pd in the near surface region, i.e. within or close to the surficial  $\text{Ga}_2\text{O}_3$  layer. As in addition, the  $\text{Ga}_{\text{Ox}}/\text{Pd}$  ratio is higher for the surface sensitive  $\text{Ga}_{\text{Ox}}$  2p level compared to bulk-sensitive  $\text{Ga}_{\text{Ox}}$  3d, the enrichment of Pd within the  $\text{Ga}_2\text{O}_3$  surface layer can be ruled out. Hence, the XPS data clearly indicate an accumulation of Pd at the  $\text{Ga}^0/\text{Ga}_2\text{O}_3$  interface.

Surprisingly, a completely different surface activity behavior upon oxidation was revealed for Ga alloys with the similar noble metal Pt: Here, a drastic, continuous enrichment of Pt at the near surface region was observed with increasing degree of oxidation. These results are presented and discussed in chapter 5.4.

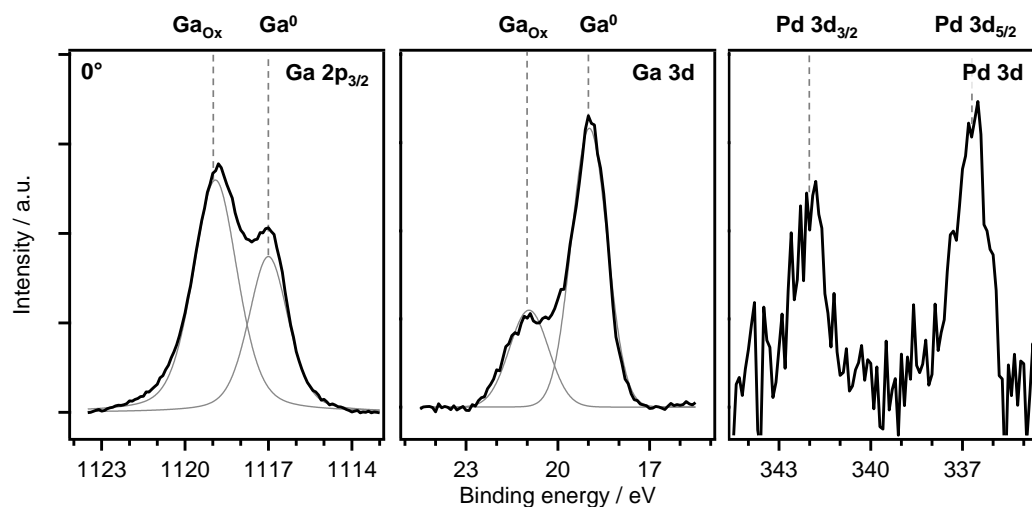


Figure 5.6: Normal emission spectra of the Pd / Ga alloy with native oxide layer at 330 K.

### 5.3. Surface Composition of Pd-Ga-Based Catalysts

Besides the more fundamental experiments on model systems discussed in chapters 5.1 and 5.2, Ga-based prototype catalysts have been analyzed by XPS. The three dimensional structure of the corresponding porous spherical supports did not allow for measurements in grazing emission. Hence, only normal emission data were recorded. One promising candidate for the dehydrogenation of 12H-NEC is a Pd-Ga alloy-based catalyst, which showed excellent performance in first test runs. The catalyst was prepared by impregnating porous carbon microspheres (Blücher, diameter 100 – 150  $\mu\text{m}$ , pores size 3 – 6 nm, pores volume 1.2 mL/g; surface 3000  $\text{m}^2/\text{g}$ ) with  $\text{LiGaH}_4$  and then refluxing the Ga-precovered microspheres in a Palladium(II)-hexafluoroacetylacetonato toluene solution. Inductively coupled plasma atomic emission spectroscopy (ICP-AES) was applied to determine the bulk composition of the catalyst and yielded a Ga content of 5 wt%, 0.8 wt% of Pd and 0.6 wt% of Li. For the XPS analysis, the catalyst was dried but no further preparation steps such as grinding were performed. The microspheres were distributed on a carbon adhesive tab to ensure sufficient grounding to minimize charging effects.

Figure 5.7 shows Ga  $2p_{3/2}$  and Pd 3d XP spectra of the catalyst, recorded in normal emission. Due to the smaller cross section of the Ga 3d core level compared to Ga  $2p_{3/2}$  and the consequently much lower signal to noise ratio, unfortunately no information could be obtained from this, more bulk sensitive, XPS region. Due to minor positive sample charging during the measurements, the spectra were shifted back by - 1.8 eV towards lower BE (with C 1s taken as reference, BE = 285 eV). From the highly surface sensitive Ga  $2p_{3/2}$  signal, the ratio of Ga(0) to Ga(III) at the very surface of the catalyst was found to be 2:1. Thus, despite of the long-term storage of the catalyst in air, surprisingly, the fraction of metallic Ga in the catalyst coating is larger than the fraction of oxidized Ga, even at the very surface. The shift of 1.5 eV found for the two Pd species fits to the chemical shift expected for Pd(II) in bulk PdO to Pd(0).<sup>67</sup> Therefore, the presence of both metallic Pd at the outer surface, and PdO, probably located at the Pd/Ga<sub>2</sub>O<sub>3</sub>, interface is suggested. Accordingly, the catalyst's coating seems to resemble the structure of Pd deposited onto Ga<sub>2</sub>O<sub>3</sub>/Ga as presented in chapter 5.1.

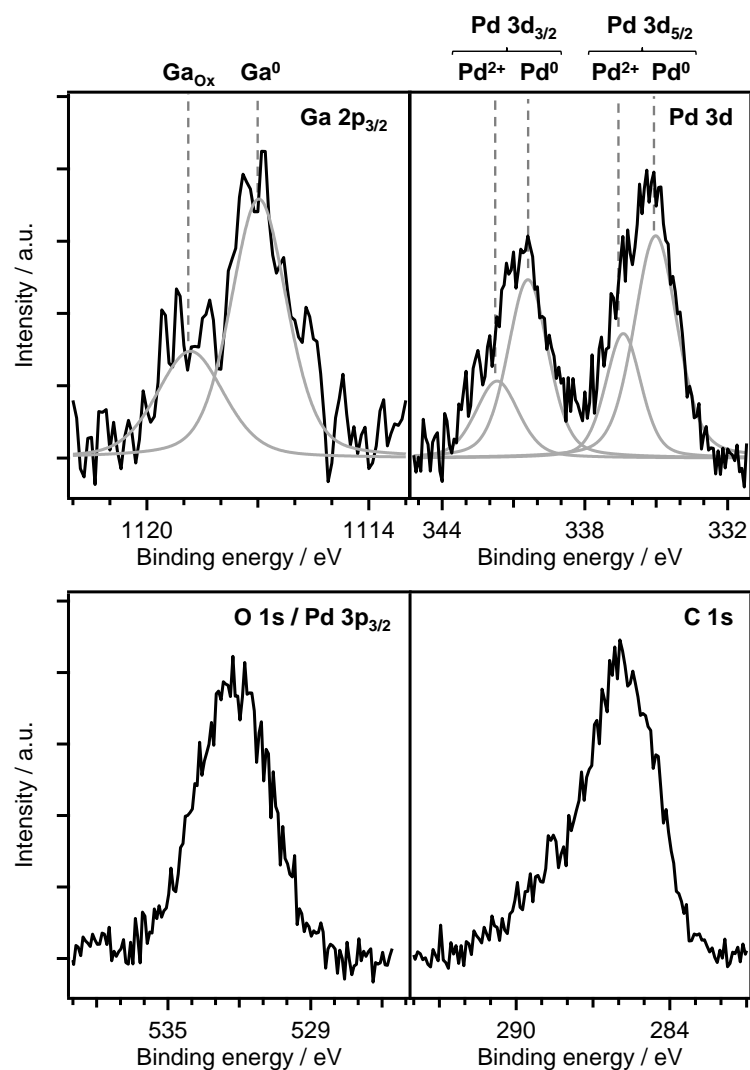


Figure 5.7: Normal emission Ga 2p<sub>3/2</sub>, Pd 3d, O 1s / Pd 3p and C 1s spectra of a Pd-Ga alloy coated carbon microsphere catalyst sample with nominally 5 wt% Ga and 0.8 wt% Pd (bulk values according to ICP-AES). Fitted lines indicate metallic and oxidic contributions to the overall peak intensities. For both Ga 2p<sub>3/2</sub> and Pd 3d core levels a met/ ox. ratio of approx. 2:1 is found.

The atomic ratio of Pd/Ga calculated from the XPS data (by taking into account the cumulative intensity of the oxidic and the metallic components for each signal) is 16.8, compared to 0.10 for the bulk composition as determined by ICP-AES. The small IMFP of low energetic Ga 2p<sub>3/2</sub> photoelectrons implies a comparably strong attenuation of the corresponding XPS signal. Nevertheless, the considerably higher Pd/Ga ratio derived from XPS compared to the bulk ratio determined by ICP-AES indicates a significant enrichment of Pd at the near surface region accessible by XPS. These results are in accordance with the stable Pd clusters, forming upon the in-situ deposition of Pd onto an oxidized Ga film as presented in chapter 5.1 and might be an explanation for the excellent performance of the catalyst.

However, more than 90 % of the atoms detected by XPS can be attributed to the carbon support (or carbonaceous impurities). This can be seen as an indication for extensive dewetting and large surface areas being not covered by the Pd-Ga alloy. However, XPS only reflects the situation on the outer parts of the catalyst, not inside the pores. Thus, no substantiated statements can be made on the catalyst's composition inside the complex morphology of the support. It is very likely that the liquid metal film is drawn into the porous structures of the catalyst by capillary forces, which might be one explanation for the observed dewetting occurring at the outer surface accessible by XPS.

Besides carbon microspheres, also porous SiO<sub>2</sub> glass microsphere carriers (Triospor 1400, diameter 70 – 140 μm, pores size 144 nm, pores volume 1.2 mL/g; surface 35 m<sup>2</sup>/g) were coated with Ga and Pd to check for catalytic activity concerning the dehydrogenation of 12H-NEC. In a first step, Ga was introduced by suspending the overnight dried carrier under argon in dry diethyl ether and adding an ethereal solution of the gallane Et<sub>3</sub>NGaH<sub>3</sub>. After complete removal of the solvent, the flask was quickly heated up to 250°C and held at this temperature until no gaseous products were developed. Once the gallane decomposition terminated, the resulting grey solid was held at this temperature under vacuum overnight and then cooled and stored under argon. The bulk Ga content as determined by ICP-AES was 21 wt%. The black spectra in Figure 5.8 shows all relevant XPS regions recorded in normal emission of the as-prepared Ga coated SiO<sub>2</sub> support. Both, the Ga 2p<sub>3/2</sub> and the Ga 3d regions show only one peak at 1119 eV and 21 eV, respectively, which can be assigned to Ga(III). The second peak arising at around 25 eV in the Ga 3d region originates from the O 2s level. The appearance of this core level can be traced back to the strong XPS contribution of the SiO<sub>2</sub> support, as also Si signals are clearly visible in XPS. In fact, about 70 % of the atoms detected by XPS can be assigned to SiO<sub>2</sub>, meaning that wetting of Ga on this support is slightly improved compared to the carbon microspheres discussed above, but the coating is still far from a homogeneous layer covering the entire outer surface, which is accessible by XPS. This observation is in accordance with the results presented in section 5.1 for a Ga film spread on Suprasil quartz glass. Compared to the case “Ga prepared on carbon microspheres” with both, metallic Ga and Ga<sub>2</sub>O<sub>3</sub>, found in XPS, only fully oxidized Ga was found for the coated SiO<sub>2</sub> microspheres –

at least in the surface region accessible by XPS (as discussed above, XPS might not reflect the situation inside the porous network adequately). Possibly, the SiO<sub>2</sub> support promotes the oxidation of Ga and consequentially, the thickness of the Ga<sub>2</sub>O<sub>3</sub> layer is increased. Similar observations were made during the investigation of liquid Ga films with a native oxide layer on Suprasil glass. Sputtering of these films under relatively mild conditions did only lead to the removal of carbon, whereas the amount of oxygen at the surface was hardly affected (cf. chapter 5.1).

To introduce Pd onto the Ga pre-coated support, the carrier was suspended in distilled water and a solution of (NH<sub>4</sub>)<sub>2</sub>[PdCl<sub>4</sub>] in distilled water was added. The reaction mixture was held under stirring until the reaction completed. After filtering and washing steps with distilled water and acetone, the spheres were dried under vacuum. After this second preparation step, ICP-AES revealed a bulk composition of 15 wt% Ga and 1.1 wt% Pd. As seen in the blue Ga 2p<sub>3/2</sub> and Ga 3d XP spectra in Figure 5.8, the addition of Pd did not lead to significant changes in the non-Pd core levels. Particularly, only Ga(III) at the catalyst's surface is detected in XPS. Interestingly, with the addition of Pd, the amount of carbon impurities at the catalyst surface decreases by 75 % and in return the intensities of SiO<sub>2</sub> and Ga core levels increase. XPS could further confirm the presence of Pd at the surface (cf. Figure 5.8, blue spectrum). The atomic ratio of Pd/Ga calculated from the XPS data (Pd 3d vs. Ga 3d) is 0.08, i.e., a clear enrichment of Pd at the outer catalyst surface compared to the bulk composition determined by ICP-AES (0.05) is observed. However, the Pd/Ga ratio is significantly lower compared to the Pd-Ga impregnated carbon microspheres discussed above. Accordingly, the BE of 336.1 eV fits to surficial Pd<sub>SO</sub><sup>181</sup> (see also chapter 5.1) and not to the BE of bulk PdO at 336.5 eV, indicating a rather low Pd content. Thus, the Pd density on SiO<sub>2</sub> at the outer surface accessible by XPS is expected to be considerably lower compared to Pd-Ga on C microspheres. The difference concerning the Pd concentration at the surface might be a consequence of the interactions of the Pd-Ga alloy coatings with the respective support. Moreover, the different reaction pathways and reaction recipes applied to produce the coatings on the two different supports might play a decisive role, but for a detailed understanding further investigation will be necessary.

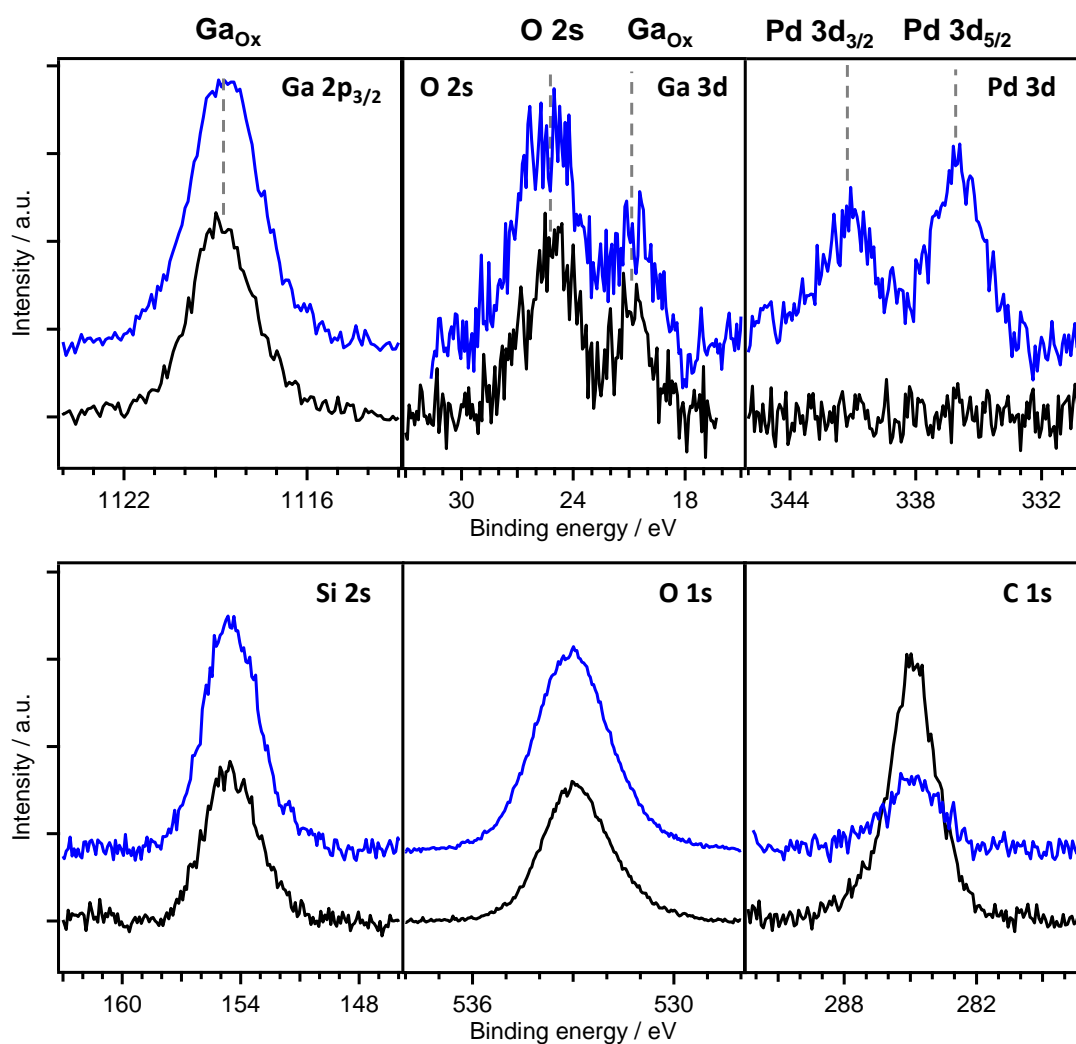


Figure 5.8:  $0^\circ$  Ga 2p<sub>3/2</sub>, Ga 3p, Pd 3d, Si 2s, O 1s and C 1s XP spectra of Ga impregnated porous SiO<sub>2</sub> carriers. Black spectra: after first impregnation step using LiGaH<sub>4</sub>. Blue spectra: After second preparation step with Palladium(II)-hexafluoroacetylacetonato to introduce Pd.

## 5.4. Oxidation of Pt-Ga Alloys

In sections 5.1 and 5.2 liquid Ga or Ga alloy films were spread across planar W foil or Suprasil glass supports in order to create films with thicknesses of roughly 0.5 nm covered by a native thin oxide film. For the oxidation of Pt-Ga alloys, the preparation of the samples was performed in an entirely different manner. A W crucible with a height of 5 mm and a width of 12 mm was filled with 1.6 g of liquid Ga. At the top of the crucible, a W mesh was installed to prevent the Ga to spill over the edges of the vessel during positioning. As the mesh was completely covered with Ga, no W signals were observed during the XPS measurements. The sample was sputtered for 15 h at 500 K until no more traces of carbon and oxygen could be observed in XPS (see Figure 5.9, bottom black spectra). Please note, that this kind of sample preparation did not allow for 80° measurements. All data shown in this section were thus measured in normal emission. To produce the Pt-Ga alloy, the sample was first moved into the loadlock, which was vented with N<sub>2</sub> to minimize oxidation. Then, an H-flame annealed Pt wire ( $m = 83 \text{ mg} \triangleq 2.0 \text{ at\% Pt}$ ) was inserted into the still liquid Ga sample. After the transfer back into the UHV chamber, XP spectra from this type of sample were recorded after different in-situ / ex-situ preparation steps. It should be mentioned at this point, that this experiment was only a proof-of-concept series. Later, a more elaborated near ambient pressure XPS study was performed by Grabau et al. in the same research group.<sup>178</sup>

Spectra after the first ex-situ preparation step (liquid Ga containing the still visible Pt wire) are shown in Figure 5.9 (red spectra). As can be seen by the presence of the strong O 1s signal and the oxidic contributions of the Ga 3d and Ga 2p<sub>3/2</sub> peaks, the formation of a surface oxide could not be prevented despite the N<sub>2</sub> atmosphere in the loadlock. Also the Pt 4f doublet signal is showing two contributions. The contribution at lower BE can easily be assigned to metallic Pt. The Pt 4f BE shifts known from literature are +1.1 – 1.3 eV for PtO, and +2.9 eV for Pt<sub>2</sub>O<sub>4</sub>.<sup>182-184</sup> The observed BE shift of +1.8 eV for the second contribution does not fit to any of these known Pt oxides. Hence, this peak is assigned to Pt atoms located inside a Ga<sub>2</sub>O<sub>3</sub> environment. This finding implies that the incorporation of Pt into Ga<sub>2</sub>O<sub>3</sub> partly already occurs at RT. After sputtering followed by heating to 900 K for 12 hours, the blue spectra in Figure 5.9 were recorded. Both the small

O 1s signal and the virtual absence of the oxidic contributions in the Ga 3d and Ga 2p regions indicate that the surface oxide has almost completely vanished. Interestingly, with no oxide being present at the surface of the Pt-Ga alloy, the very low Pt 4f intensity reveals that there is also hardly any Pt located in the near surface region.

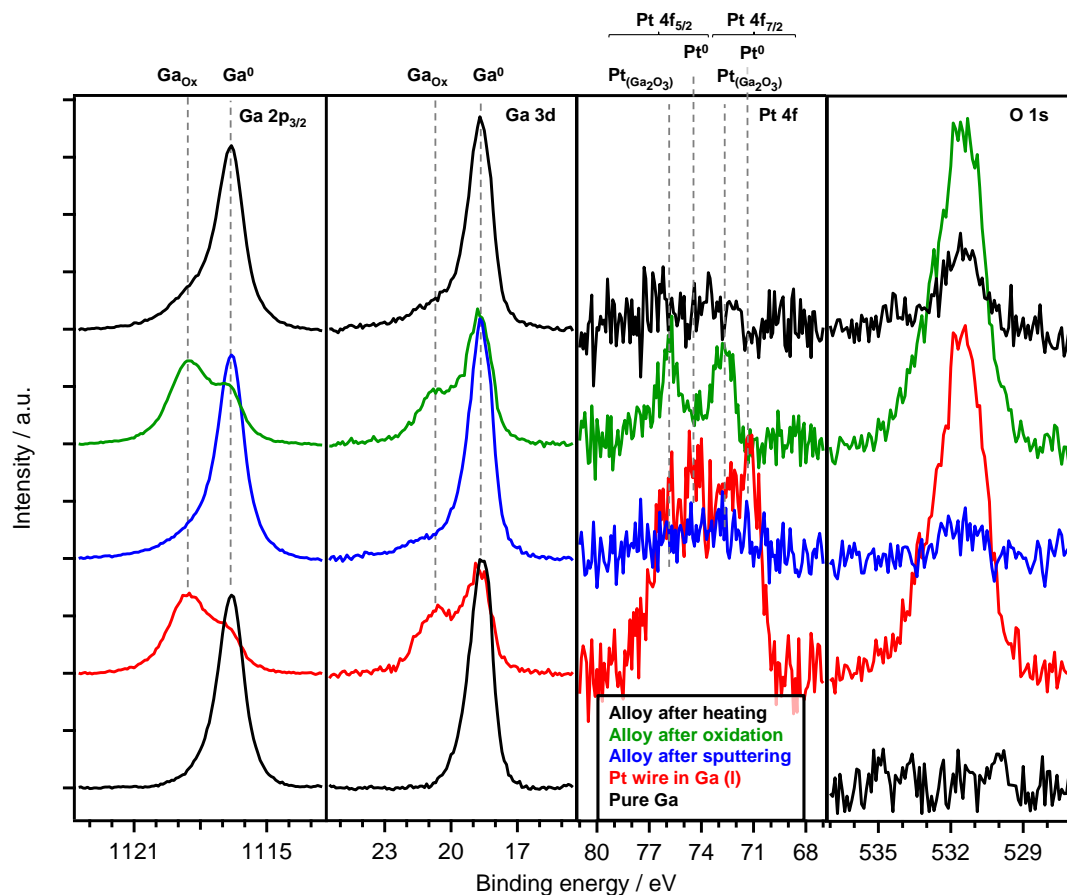


Figure 5.9: Normal emission spectra of a Pt-Ga alloy with 2.0 at.% Pt: Pure Ga after extensive sputtering (black, bottom); liquid Ga with the added Pt wire (red); Pt-Ga alloy after sputtering at 900 K for 10 h (blue); Pt-Ga alloy after oxidation in air for 1 min (green); oxidized Pt-Ga alloy after heating to 750 K for 1 h (black, top).

The situation changes drastically when the sample is oxidized. For this purpose, the sample was moved into the loadlock which was then vented with air for 1 min. As proven by the green spectra in Figure 5.9, an oxide layer has been formed at the surface of the Pt-Ga alloy. Along with the increase of the O 1s intensity – accompanied by the formation of the oxidic contributions in the two Ga 3d and Ga 2p regions – the Pt 4f intensity also increased. Quantitative analysis of the fitted Ga 3d and O 1s peak areas yields a stoichiometry of  $\text{Ga}_2\text{O}_{3.4}$  for the formed oxide. When calculating the thicknesses of the oxide layer, application of equation 6 yields

values of 13.3 Å for Ga 3d and 12.1 Å for Ga 2p. As the thickness of the native oxide of the Ga-Pt alloy does not differ significantly from the thickness obtained for pure Ga in chapter 6.1, the influence of Pt on the formation of the oxide surface layer seems to be negligible. Heating the sample in UHV at 750 K for 10 min again reduces the surface (thermal decomposition of Ga<sub>2</sub>O<sub>3</sub>) as witnessed by decrease of O 1s and Ga-oxide signals in XPS, which is accompanied by a decrease in Pt (Figure 5.9, top black spectra). Apparently, Pt is enriched within the surface gallium oxide.

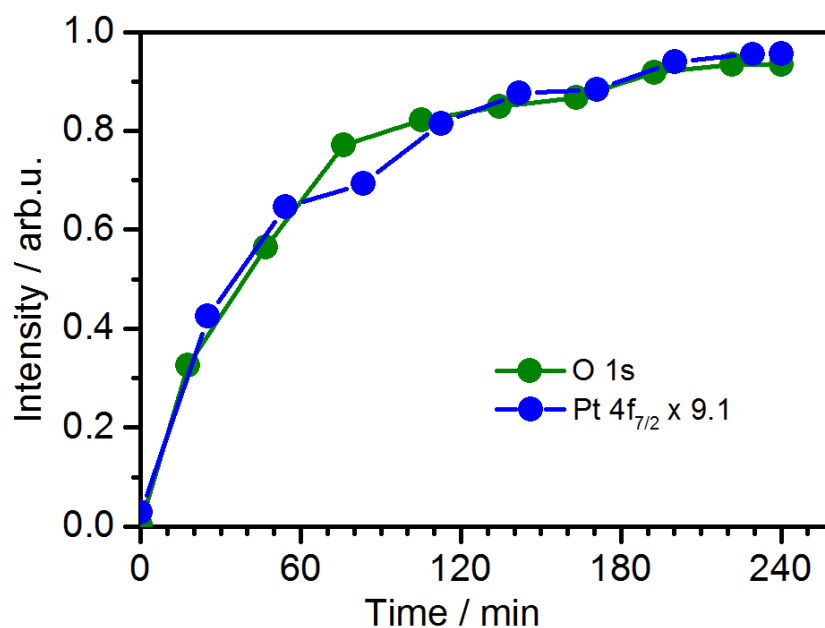


Figure 5.10: O 1s (green) and Pt 4f<sub>7/2</sub> intensities (blue) of a liquid Pt-Ga alloy with 1.8 at.% Pt during the dosage of oxygen ( $3 \times 10^{-7}$  mbar) at 550 K. Taken from reference<sup>178</sup>.

After the initial measurements presented in this work, the surface enrichment and depletion of Pt during the oxidation of Pt-Ga alloys were investigated in greater detail by Grabau et al. in a near-ambient pressure XPS study. As seen in Figure 5.10, which was adapted from reference<sup>178</sup>, for a Pt-Ga alloy with 1.8 at.% Pt, the Pt 4f<sub>7/2</sub> signal increases proportional with the increase of the O 1s signal during the in-situ oxidation ( $T = 550$  K;  $p_{\text{O}} = 3 \times 10^{-7}$  mbar). Without any surface oxide, hardly any Pt signals could be detected in the XPS by Grabau et al., confirming the findings shown here.

---

## 5.5. Summary and Conclusions

Pd-Ga and Pt-Ga intermetallic compounds exhibit excellent catalytic activity, particularly in methanol steam reforming or hydrogenation and dehydrogenation reactions.<sup>75, 81, 82, 171</sup> In this context, structure and composition of the surface of different types of Pd-Ga and Pt-Ga systems were analyzed by means of XPS. Upon the thermal deposition of Pd onto the native oxide layer of a macroscopic thin Ga film spread on Suprasil quartz glass and cooled with N<sub>2</sub> (l), the formation of a more or less homogeneous Pd layer on the Ga oxide layer was found. Analysis of the XPS data further revealed a partial reduction of Ga<sub>2</sub>O<sub>3</sub> by deposited Pd. When temperature was increased, melting of the Ga film provoked the formation of Pd clusters on the partially reduced Ga oxide layer, which seemed to be stable under reducing UHV conditions. Next, the surface composition of a natively oxidized low Pd content Pd-Ga alloy spread on W foil was investigated. For this system, an enrichment of Pd – apparently being present as Pd(II) – was found underneath the surficial Ga<sub>2</sub>O<sub>3</sub> layer. In addition, real experimental catalysts were analyzed by XPS. For porous carbon microspheres chemically impregnated with Ga and Pd, a strong relative increase of Pd compared to Ga XPS signal intensity was observed, indicating an enrichment of Pd at the very outer surface of the catalyst accessible by XPS. From the structure of both Ga and Pd XPS peaks, the presence of metallic and oxidized species is deduced with a ratio of 2:1 for both of the metals. For porous SiO<sub>2</sub> catalysts chemically impregnated with Ga and Pd, XPS peak positions revealed the presence of oxidized Ga and Pd species only. Moreover, the amount of Pd at the detectable surface area was lower compared to the system with a carbon carrier. As a final experiment, the surface composition of a sample containing bulk amounts of a low Pt content Pt-Ga alloy was analyzed by XPS before and after oxidation. Whereas Pt was found to be virtually absent at the unoxidized alloy surface, a drastic increase of Pt signals was observed upon oxidation, which was explained by the enrichment of Pt within surface gallium oxide.

With respect to catalytic systems based on Pd-Ga intermetallics, the observed stabilization of surface Pd by the native Ga oxide layer might be a crucial factor for the high activity of the catalysts – at least under oxidative conditions. The same holds true for the enrichment of Pt in the near surface region upon oxidation in case

of Pt-Ga intermetallic compounds applied in catalysis. The situation might be different under the reductive conditions of hydrogenation reactions. Model reaction studies such as near ambient pressure XPS investigations will address these questions in the future.





---

## 6. Summary and Outlook

Due to their entirely ionic nature, ionic liquids (ILs) exhibit some outstanding physicochemical properties and since the turn of the millennium, ILs have received growing attention in many research fields. In this thesis, angle-resolved X-ray photoelectron spectroscopy (ARXPS) under ultrahigh vacuum (UHV) conditions was applied to investigate the interface properties of ILs in contact with solid support materials. Beyond ILs, surface and interface properties of pristine and oxidized Pd and Pt alloys of the low melting point metal Ga were analyzed by ARXPS with respect to their potential application in catalysis.

In the context of IL-carbon based electrochemical applications, thin films of the IL  $[\text{C}_1\text{C}_1\text{Im}][\text{Tf}_2\text{N}]$  were thermally deposited onto different carbonaceous supports, that is, highly oriented pyrolytic graphite (HOPG) and Ni(111)-supported graphene with two different graphene coverages, namely, 0.6 and 1.0 layers. These studies revealed some major differences of the initial adsorption behavior and further growth of the IL depending on the substrate. On HOPG, cations and anions were found to adsorb next to each other in a so-called checkerboard arrangement. Initially a wetting layer with a maximum coverage of 0.5 monolayers was formed, that is, one closed ionic layer according to the definition of one IL monolayer applied in this thesis. Further IL deposition led to pronounced growth of 3D islands. On Ni(111)-supported single layer graphene, a stable IL wetting layer, twice as thick as on HOPG, was formed, consisting most likely of neighboring ion pairs with anions on top of cations and cations on top of anions in a checkerboard configuration. For higher IL coverages, 3D growth was less pronounced compared to HOPG, which was attributed to the so-called wetting transparency of graphene. On Ni(111) covered with a fractional graphene layer of 0.6 layers,  $[\text{C}_1\text{C}_1\text{Im}][\text{Tf}_2\text{N}]$  was found to preferentially adsorb on bare Ni surface areas. Moreover, ARXPS revealed the sandwich configuration of the IL ions known from the bare Ni(111) surface, that is, anions initially adsorbing on top of cations. Further, the preferential IL adsorption on bare Ni surface areas caused more pronounced 3D growth compared to the fully graphene-covered Ni(111) surface.

With respect to IL based catalytic concepts, namely, solid catalyst with ionic liquid layer (SCILL) and supported ionic liquid phase (SILP), the IL-metal interface was investigated with ARXPS. Due to the limitation of conventional IL physical vapor deposition (IL-PVD) to thermally stable ILs, electrospray ionization deposition of ILs (IL-ESID) was established as an alternative technique for the in-situ preparation of ultrathin IL films. As a proof of concept, a well-studied system was chosen for the first IL-ESID experiments: Analysis of ESID  $[\text{C}_8\text{C}_1\text{Im}][\text{Tf}_2\text{N}]$  thin films prepared on Au(111) revealed that these films were virtually identical to films grown by standard PVD. Although the ESID process was performed in positive bias mode, quantitative XPS analysis did not show a measurable excess of cations. This finding is attributed to the large excess of neutral IL ion pairs in the initial droplets formed during the ESI process. The main drawback of IL-ESID is the low deposition rate, which was found to be more than one order of magnitude smaller than in case of IL-PVD. In a second step, the thermally unstable IL  $[\text{C}_8\text{C}_1\text{Im}]\text{Cl}$  was applied for thin film preparation on Au(111) by IL-ESID. By means of ARXPS, it was shown that for low coverages up to 0.5 monolayers, the IL initially forms a wetting layer with the cationic imidazolium ring and the chloride anion adsorbed next to each other in a checkerboard configuration, similar to  $[\text{C}_8\text{C}_1\text{Im}][\text{Tf}_2\text{N}]$ . One difference was found concerning the orientation of the octyl chains toward vacuum, which was more pronounced in case of  $[\text{C}_8\text{C}_1\text{Im}]\text{Cl}$  than for  $[\text{C}_8\text{C}_1\text{Im}][\text{Tf}_2\text{N}]$ , indicating a higher degree of order in the  $[\text{C}_8\text{C}_1\text{Im}]\text{Cl}$  wetting layer. For higher IL coverages, pronounced 3D island growth was observed on top of the initial wetting layer. This was in harsh contrast to the 2D layer-by-layer growth, found for  $[\text{C}_8\text{C}_1\text{Im}][\text{Tf}_2\text{N}]$  for coverages up to at least ten monolayers.

Furthermore, IL-PVD and IL-ESID were used alternatively to produce thin  $[\text{C}_2\text{C}_1\text{Im}][\text{EtOSO}_3]$  and  $[\text{C}_2\text{C}_1\text{Im}][\text{OTf}]$  films on pristine and modified Au(111). Under the applied conditions,  $[\text{C}_2\text{C}_1\text{Im}][\text{EtOSO}_3]$  was found to thermally decompose during PVD. As deduced from mass spectrometry measurements, the main decomposition product was ethanol. Besides, significant amounts of methanol and 1-alkyl imidazole species were detected. For thicknesses in the sub-monolayer regime of the PVD films, ARXPS revealed co-adsorbed decomposition products alongside the adsorption of intact  $[\text{C}_2\text{C}_1\text{Im}][\text{EtOSO}_3]$  ion pairs. In contrast, no indications for contamination of corresponding IL films were observed at higher

coverages. Hence, solely ESID was applied for IL coverages in the sub-monolayer regime, whereas PVD was applied for larger IL coverages. Via ARXPS,  $[\text{C}_2\text{C}_1\text{Im}][\text{EtOSO}_3]$  was found to initially adsorb on Au(111) in a checkerboard arrangement with the ring of the dialkylimidazolium cation lying flat and the anion's ethyl group pointing towards vacuum. For higher IL coverages, 2D layer-by-layer growth was observed on pristine Au(111). In contrast, for  $[\text{C}_2\text{C}_1\text{Im}][\text{EtOSO}_3]$  films deposited on a carbon contaminated Au surface, ARXPS revealed the onset of 3D island growth after the initial formation of a wetting layer with a thickness of 0.5 monolayers. For  $[\text{C}_2\text{C}_1\text{Im}][\text{OTf}]$ , a similar initial adsorption behavior with cations and anions adsorbing in a checkerboard arrangement was observed at low coverages. Unexpectedly, for higher coverages, the ARXPS data clearly indicated the onset of pronounced 3D growth on top of the initially formed 2D wetting layer of a maximum thickness of 0.5 monolayers. Strongly improved wettability of the Au substrate with  $[\text{C}_2\text{C}_1\text{Im}][\text{OTf}]$  was obtained by depositing small amounts of Pd prior or subsequent to the deposition of the IL – indicating attractive interactions between  $[\text{C}_2\text{C}_1\text{Im}][\text{OTf}]$  and Pd. Further, in case of Pd deposition subsequent to the deposition of the IL, the ARXPS data revealed particularly strong interactions between the dialkylimidazolium cation and single Pd atoms. Apparently, these interactions even inhibit the otherwise occurring surface alloying of Pd with the Au substrate.

In the context of catalytically active Pd-Ga and Pt-Ga intermetallic systems, surface structure and composition of corresponding pristine and oxidized samples were analyzed by means of XPS. Upon oxidation, the Pt-Ga and Pd-Ga samples, surprisingly, showed a completely different behavior. Whereas Pt was found to accumulate in the growing  $\text{Ga}_2\text{O}_3$  layer, Pd vanished from the oxidized near surface area and enriched at the buried bulk Ga<sup>0</sup>/surface  $\text{Ga}_2\text{O}_3$  interface. In another experiment, stabilization of surficial Pd could be achieved by the thermal evaporation of Pd onto the native oxide layer of a thin Ga film. Analysis of the XPS data further revealed a partial reduction of  $\text{Ga}_2\text{O}_3$  by deposited Pd. Besides, carbon and  $\text{SiO}_2$  microsphere catalysts chemically impregnated with a Pd-Ga coating were investigated. At the outer surface of the catalyst accessible by XPS, an enrichment of Pd was found on both supports – particularly on the carbon carrier.

In the future, investigations on the IL/metal interface will be expanded on Ag(111), as a first approach towards industrially applied Ag-based catalysts. In the same context, real SCILL catalysts will be investigated with XPS in order to analyze their surface composition, also with respect to potential changes depending on the IL loading.

In addition, with the new dual electron analyzer ARXPS instrument, which was set into operation during the work on this thesis, in future work, additional information on the IL/solid interface can be obtained due to better energy resolution and faster data recording without the need of sample tilting. By combining photoelectron spectroscopy with a microscopic technique, such as scanning probe microscopy in a new scanning tunneling microscopy/atomic force microscopy (STM/AFM) vacuum instrument, interpretation of ambiguous XPS results should be facilitated even further.

For thermally unstable ILs, IL-ESID turned out to be a suitable alternative for IL-PVD. However, the fluctuating and comparatively slow deposition rate demands for further improvements concerning the experimental setup. Due to problems concerning long-term stability, also the PVD apparatus is currently subject to a major overhaul, including a completely new design of the main Knudsen cell.

Finally, further ideas for future experiments involve the successive deposition of multiple ILs to investigate the resulting layering behavior and a completely new field could be opened with in-situ electrochemical reactions monitored via XPS.





## 7. Zusammenfassung und Ausblick

Aufgrund ihres vollständig ionischen Charakters weisen ionische Flüssigkeiten (engl. ionic liquids, ILs) diverse bemerkenswerte physikochemische Eigenschaften auf und gewinnen seit der Jahrtausendwende in vielen Forschungsbereichen zunehmend an Bedeutung. In dieser Arbeit wurden mittels winkelaufgelöster Röntgenphotoelektronenspektroskopie (engl. angle-resolved X-ray photoelectron spectroscopy, ARXPS) unter Ultrahochvakuumbedingungen (UHV) Grenzflächeneigenschaften ionischer Flüssigkeiten in Kontakt mit festen Trägermaterialien untersucht. Einen zweiten Schwerpunkt, außerhalb des Bereichs der ILs, stellte die ARXPS-Analyse von Ober- und Grenzflächeneigenschaften reiner und oxidierter Pd-Ga- bzw. Pt-Ga-Legierungen in Hinblick auf deren potentiellen Einsatz in katalytischen Systemen dar.

Im Rahmen IL-kohlenstoffbasierter elektrochemischer Anwendungen wurden dünne Filme der IL  $[\text{C}_1\text{C}_1\text{Im}][\text{Tf}_2\text{N}]$  mittels thermischer Verdampfung auf verschiedene kohlenstoffhaltige Substrate abgeschieden, nämlich auf hochgeordneten pyrolytischen Graphit (engl. highly oriented pyrolytic graphite, HOPG) und zweierlei Graphen/Ni(111)-Systeme mit Graphenbedeckungen von 0,6 bzw. 1,0 Lagen. Hierbei zeigten sich in Abhängigkeit des Substrates grundlegende Unterschiede bezüglich des Adsorptionsverhaltens im Submonolagenbereich sowie bezüglich des weiteren Wachstums der IL für höhere Bedeckungen. Im Falle von HOPG offenbarten die ARXPS-Daten die Ausbildung einer Benetzungsschicht mit einer maximalen Dicke von 0,5 Monolagen (entsprechend einer geschlossenen Ionenlage nach der in dieser Arbeit verwendeten Definition einer IL-Monolage) unter direkter Adsorption von Kat- und Anionen in einer sogenannten Schachbrett-Anordnung. Die weitere Abscheidung der IL führte zu ausgeprägtem 3D-Inselwachstum. Im Falle des Einschicht-Graphen/Ni(111)-Systems konnte die Ausbildung einer stabilen Benetzungsschicht mit einer, im Vergleich zu HOPG, doppelten maximalen IL-Bedeckung beobachtet werden, die sich sehr wahrscheinlich aus benachbarten, alternierenden Ionenpaaren zusammensetzte. Das bei höheren Bedeckungen ebenfalls einsetzende 3D-Wachstum erwies sich im

Vergleich zu HOPG als deutlich weniger stark ausgeprägt, was auf die sogenannte Benetzungstransparenz des Graphens zurückgeführt wurde. Bei unvollständiger Graphenbedeckung (0,6 Lagen Graphen) zeigte sich eine bevorzugte IL-Adsorption auf den freiliegenden Oberflächenbereichen des Ni(111)-Substrates, einschließlich der bei niedrigen IL-Bedeckungen für die reine Ni(111)-Oberfläche bekannte „Sandwich-Anordnung“, d. h. der übereinander erfolgenden Adsorption von Anionen auf Kationen. Die bevorzugte IL-Adsorption auf freiliegenden Oberflächenbereichen des Ni(111)-Substrates führte ferner zu stärker ausgeprägtem 3D-Wachstum als im Falle des Einschicht-Graphen/Ni(111)-Systems.

Feststoffkatalysatoren beschichtet mit ionischer Flüssigkeit (engl. solid catalyst with ionic liquid layer, SCILL) sowie geträgerte ionische Flüssigkeitsphasen (engl. supported ionic liquid phase, SILP) stellen vielversprechende IL-basierte Katalysekonzepte dar, vor deren Hintergrund die IL-Metall-Grenzfläche mittels ARXPS untersucht wurde. Aufgrund der Beschränkung der physikalischen Gasphasenabscheidung ionischer Flüssigkeiten (engl. IL physical vapor deposition, IL-PVD) auf ausschließlich thermisch stabile ILs, wurde im Zuge dieser Arbeit die Elektrospray-Ionisationsabscheidung ionischer Flüssigkeiten (engl. IL electrospray ionization deposition, IL-ESID) als Alternativmethode zur in-situ Herstellung ultradünner IL-Filme entwickelt. Im Sinne eines Machbarkeitsnachweises wurde für die ersten IL-ESID-Experimente ein gut erforschtes System ausgewählt. Hierbei erwiesen sich mittels ESID auf Au(111) abgeschiedene  $[\text{C}_8\text{C}_1\text{Im}][\text{Tf}_2\text{N}]$ -Filme als praktisch identisch mit Filmen, die mittels der PVD-Standardmethode erzeugt wurden. Trotz der Durchführung des ESID-Prozesses unter positiver Vorspannung zeigte sich in der quantitativen Auswertung der XPS-Daten kein messbarer Überschuss an Kationen. Dies wurde auf den großen Überschuss neutraler IL-Ionenpaare in den zu Beginn des ESI-Prozesses gebildeten Tropfen zurückgeführt. Als großer Nachteil des IL-ESID-Verfahrens erwies sich die im Vergleich zu IL-PVD um mehr als eine Größenordnung geringere Abscheidungsrate. Im nächsten Schritt wurden dünne Filme der thermisch instabilen IL  $[\text{C}_8\text{C}_1\text{Im}]\text{Cl}$  mithilfe von IL-ESID auf Au(111) abgeschieden. Bei niedrigen IL-Bedeckungen von bis zu 0,5 Monolagen ergab die Untersuchung mittels ARXPS – analog zu  $[\text{C}_8\text{C}_1\text{Im}][\text{Tf}_2\text{N}]$  – die Ausbildung einer Benetzungsschicht und ferner die direkte Adsorption von Imidazolium- und Chlorid-Ionen in einer Schachbrett-Anordnung. Ein Unterschied

fand sich bezüglich der Orientierung der Oktylketten in Richtung Vakuum. Die stärkere Orientierung im Falle von  $[\text{C}_8\text{C}_1\text{Im}]\text{Cl}$  gegenüber  $[\text{C}_8\text{C}_1\text{Im}][\text{Tf}_2\text{N}]$  deutete auf einen höheren Ordnungsgrad der  $[\text{C}_8\text{C}_1\text{Im}]\text{Cl}$ -Benetzungsschicht hin. Bei höheren IL-Bedeckungen zeigte sich ein ausgeprägtes 3D-Inselwachstum auf der anfänglichen Benetzungsschicht. Dies stellte einen starken Gegensatz zum 2D-Schichtwachstum im Falle von  $[\text{C}_8\text{C}_1\text{Im}]\text{Tf}_2\text{N}$  dar, welches hier für Bedeckungen von mindestens zehn Monolagen beobachtet wurde.

Im weiteren Verlauf dieser Arbeit wurden IL-PVD und IL-ESID abwechselnd zur Erzeugung dünner Filme der ILs  $[\text{C}_2\text{C}_1\text{Im}][\text{EtOSO}_3]$  und  $[\text{C}_2\text{C}_1\text{Im}][\text{OTf}]$  auf reinem und modifiziertem Au(111) eingesetzt. Unter den angewandten Bedingungen wurde die thermische Zersetzung von  $[\text{C}_2\text{C}_1\text{Im}][\text{EtOSO}_3]$  während deren Verwendung im IL-PVD-Verfahren beobachtet. In massenspektrometrischen Untersuchungen konnte Ethanol als Hauptzerfallsprodukt identifiziert werden. Zudem wurde die Bildung erheblicher Mengen an Methanol und 1-Alkylimidazol-Verbindungen festgestellt. Im Submonolagenbereich zeigte die ARXPS-Analyse von  $[\text{C}_2\text{C}_1\text{Im}][\text{EtOSO}_3]$ -PVD-Filmen die Adsorption von intakten Ionenpaaren sowie die Koadsorption von Zerfallsprodukten. Hingegen wurde bei höheren Bedeckungen kein Hinweis auf Kontamination entsprechender IL-Filme gefunden. Demzufolge wurde für IL-Bedeckungen im Submonolagenbereich ausschließlich ESID eingesetzt, während höhere Bedeckungen mittels PVD erzeugt wurden. Mittels ARXPS konnte für Bedeckungen bis zu einer geschlossenen Ionenlage eine Schachbrett-Anordnung nachgewiesen werden. Ferner wurden als bevorzugte Adsorptionsgeometrien im Falle des Dialkylimidazoliumions eine Orientierung des Rings parallel zur Goldoberfläche und im Falle des Anions eine Orientierung der Ethylgruppe in Richtung Vakuum beobachtet. Durch die ARXPS-Analyse von höheren IL-Bedeckungen konnte für das reine Au(111)-Substrat ein 2D-Schichtwachstum ermittelt werden. Dahingegen wurde für  $[\text{C}_2\text{C}_1\text{Im}][\text{EtOSO}_3]$ -Filme, die auf eine kontaminierte Au Oberfläche abgeschieden wurden, nach der anfänglichen Bildung einer Benetzungsschicht in Höhe einer halben Monolage, das Einsetzen von 3D-Inselwachstum festgestellt. Bei geringen Bedeckungen wurde im Falle von  $[\text{C}_2\text{C}_1\text{Im}][\text{OTf}]$  ein ähnliches Adsorptionsverhalten mit einer Schachbrett-Anordnung von An- und Kationen beobachtet. Überraschenderweise wiesen die ARXPS-Daten für höhere Bedeckungen eindeutig auf das Einsetzen von

ausgeprägtem 3D-Wachstum auf der anfänglich gebildeten Benetzungsschicht in Höhe einer halben Monolage hin. Stark erhöhte Benetzbarkeit des Au-Substrates in Kombination mit  $[C_2C_1Im][OTf]$  konnte durch die vorangehende oder nachfolgende Abscheidung von Pd erzielt werden. Dies wurde durch attraktive Wechselwirkungen zwischen  $[C_2C_1Im][OTf]$  und Pd erklärt. Die beobachteten Effekte im Fall der Pd-Abscheidung nach vorausgehender IL-Filmpräparation deuteten auf besonders starke Wechselwirkungen zwischen einzelnen Pd-Atomen und Dialkylimidazoliumionen hin, welche augenscheinlich sogar zur Unterbindung der andernfalls erfolgenden Oberflächenlegierungsbildung von Pd mit dem Au-Substrat führten.

Im Rahmen katalytisch aktiver intermetallischer Pd-Ga- und Pt-Ga-Verbindungen, wurden Oberflächenstruktur und -zusammensetzung entsprechender reiner und oxidierten Proben mittels XPS analysiert. In Abhängigkeit des Legierungspartners zeigten sich während der Oxidation der Ga-Legierungen gänzlich unterschiedliche Effekte. Während für Pt eine Anreicherung in der wachsenden  $Ga_2O_3$ -Schicht beobachtet wurde, konnte im Falle von Pd keine nennenswerte Einlagerung in der Oxidschicht festgestellt werden. Stattdessen wurden Anzeichen für die Bildung einer Pd-reichen Phase an der vergrabenen  $Ga^0/Ga_2O_3$  Grenzfläche gefunden. In einem weiteren Experiment konnte eine Stabilisierung von Oberflächen-Pd durch die thermische Abscheidung von Pd auf die native Oxidschicht eines dünnen Ga-Films erreicht werden. Die Analyse der XPS-Daten ergab ferner die partielle Reduktion von  $Ga_2O_3$  durch abgeschiedenes Pd. Darüber hinaus wurden Kohlenstoff- und  $SiO_2$ -Mikrokugelskatalysatoren nach chemischer Beschichtung mit Pd-Ga-Legierungen untersucht. Am äußersten Rand der Katalysatoren, also innerhalb des für XPS messbaren Bereichs, wurde für beide Trägermaterialien eine deutliche Anreicherung von Pd festgestellt, insbesondere im Falle des Kohlenstoffträgers.

In Zukunft sollen die Untersuchungen zur IL/Metall-Grenzfläche auf Ag(111) ausgedehnt werden. Dies würde einen ersten Schritt in Richtung Ag-basierter Katalysatoren darstellen, wie sie in der Industrie verwendet werden. In diesem Zusammenhang sollen ferner die Oberflächenzusammensetzungen angewandter SCILL-Katalysatoren mit XPS analysiert werden, auch in Hinblick auf mögliche Veränderungen in Abhängigkeit der IL-Imprägnierung.

---

Dank eines neuen, mit zwei Elektronenanalysatoren ausgestatteten ARXPS-Instrumentes, können zukünftig aufgrund dessen besserer Energieauflösung sowie der schnelleren Messgeschwindigkeit (das Kippen der Probe entfällt) ergänzende Informationen zur IL/Feststoff-Grenzfläche gewonnen werden. Die Kombination mit einem künftigen Großgerät für Rastertunnel- und Rasterkraftmikroskopie (engl. scanning tunneling microscopy, STM und atomic force microscopy, AFM) sollte die Interpretation mehrdeutiger XPS-Ergebnisse zusätzlich erleichtern.

Im Falle thermisch instabiler ILs erwies sich IL-ESID als geeignete Alternative für das herkömmliche IL-PVD-Verfahren. Jedoch sollte wegen der ungleichmäßigen und vergleichsweise langsamen Abscheidungsrate der experimentelle Aufbau weiter optimiert werden. Aufgrund von Problemen hinsichtlich der Langzeitstabilität des PVD-Verdampfers wird auch dieser derzeit einer Generalüberholung unterzogen, die ein komplettes Neudesign der zentralen Knudsenzelle beinhaltet.

Abschließend seien als Ideen für zukünftige Experimente zum einen die aufeinanderfolgende Abscheidung verschiedener ILs zur Untersuchung des sich ergebenden Schichtungsverhaltens, sowie als gänzlich neues Feld die XPS-Beobachtung von in-situ durchgeführten elektrochemischen Reaktionen genannt.



## 8. Appendix

### 8.1. [C<sub>1</sub>C<sub>1</sub>Im][Tf<sub>2</sub>N] on 1.7 L Graphene

In addition to the results presented in chapter 3.2 on [C<sub>1</sub>C<sub>1</sub>Im][Tf<sub>2</sub>N] thermally deposited onto Ni(111)-supported fractional and single layer graphene, one further experiment was performed involving Ni(111)-supported multilayer (1.7 L) graphene. The results provide some interesting information on the IL/graphene interface. However, due to the difficulties concerning the grazing emission data, which have been addressed in chapter 3.2, the observations could not be interpreted with absolute certainty. Consequentially, these results were left out in the discussion in the main part of the thesis and will be presented in the following pages instead.

Figure 8.1 shows the 0° Ni 2p and C 1s spectra of clean Ni(111), Ni(111) covered with 0.6, 1.0, and 1.7 layers of graphene, and the benzene/Ni(111) reference spectrum. The graphene C 1s BE was  $285.0 \pm 0.1$  eV, in agreement with previous studies.<sup>113</sup> Note that with the given energy resolution of 0.9 eV the bridge-top and top-fcc graphene adsorption geometries<sup>113</sup> cannot be resolved.

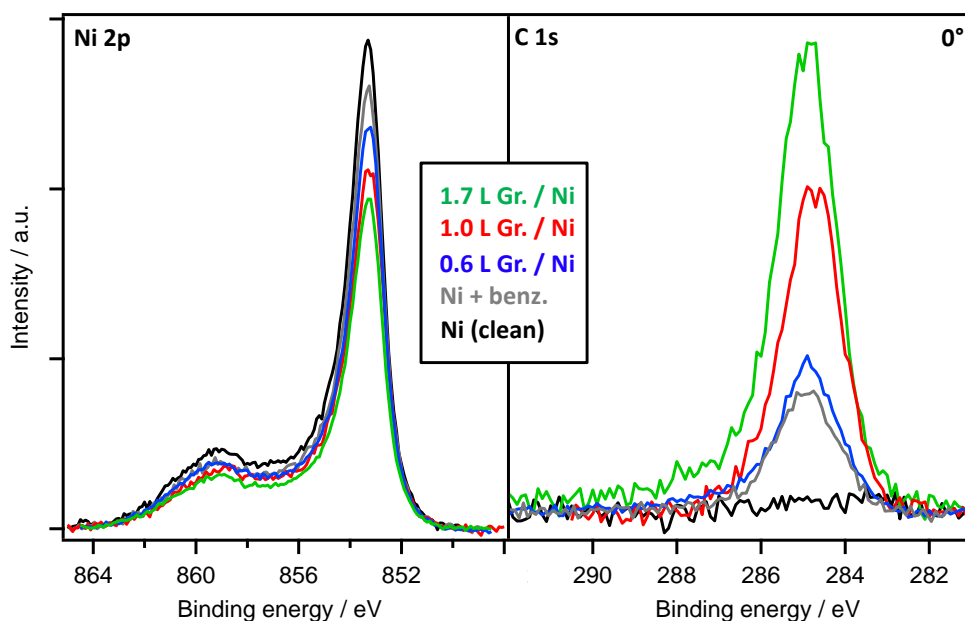


Figure 8.1: Ni 2p and C 1s spectra of clean Ni(111) and Ni(111) supported graphene with coverages of 0.6, 1.0, and 1.7 L; All data collected at normal emission.

In Figure 8.2, normal and 80° C 1s spectra of  $[C_1C_1Im][Tf_2N]$  films on Ni(111)-supported graphene (0.6, 1.0, and 1.7 L) with increasing IL coverages are depicted. The spectra show that for comparable amounts (indicated by the same colors) of deposited IL, pronounced intensity differences of the IL signals and of the damping of the graphene signals are found for the three substrates. This behavior demonstrates that initial adsorption behavior and further IL growth strongly depend on the coverage of the underlying graphene layer. The IL adsorption and growth behavior for 0.6 and 1.0 L graphene was discussed in detail in chapter 3.1. Hence, only the situation for 1.7 L graphene will be described in the following.

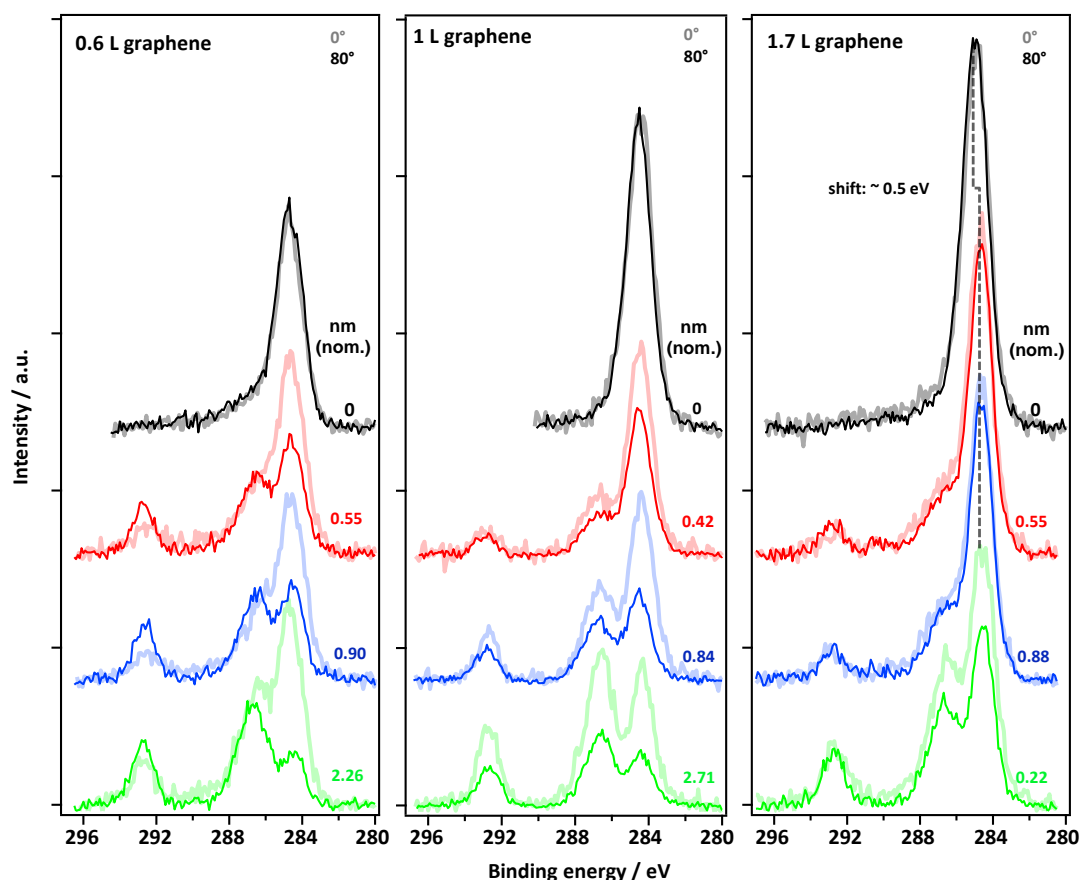


Figure 8.2: 0° (dark color) and 80° (light color) C 1s spectra of  $[C_1C_1Im][Tf_2N]$  thin films deposited on graphene / Ni(111). Graphene coverage (in layers) is given in the top left corner. Nominal IL film thickness (in nm) is given on the right hand side of each diagram.

The red curves in Figure 8.3 shows that for 1.7 layers graphene/Ni(111), the Ni 2p attenuation at 0° is strongly reduced, whereas the graphene C 1s attenuation initially follows the expected behavior for 2D growth. The attenuation by overlaying graphene results in a higher amount of Ni 2p photoelectrons reaching the analyzer, that only have to travel through one layer of graphene. Due to the small

IMFP of the low energy Ni 2p photoelectrons, this effect is not negligible for the investigated system. The discrepancy between Ni 2p and C 1s attenuation suggests that the deposited IL is mainly located at surface areas covered with double layer graphene. In this case, the large Ni 2p contribution stemming from areas covered with just one layer of graphene would not be affected, which could explain the weaker attenuation of the Ni 2p signal compared to graphene C 1s. Additionally, as shown in Figure 8.4, for 1.7 L graphene/Ni(111) the graphene C 1s peak experiences a significantly larger shift towards lower BE ( $\sim 0.5$  eV vs.  $\sim 0.2$  eV for 1.0 L graphene). Figure 8.4 also shows that the increase of IL related signals in surface sensitive  $80^\circ$  emission is much lower compared to the systems with lower graphene coverage.

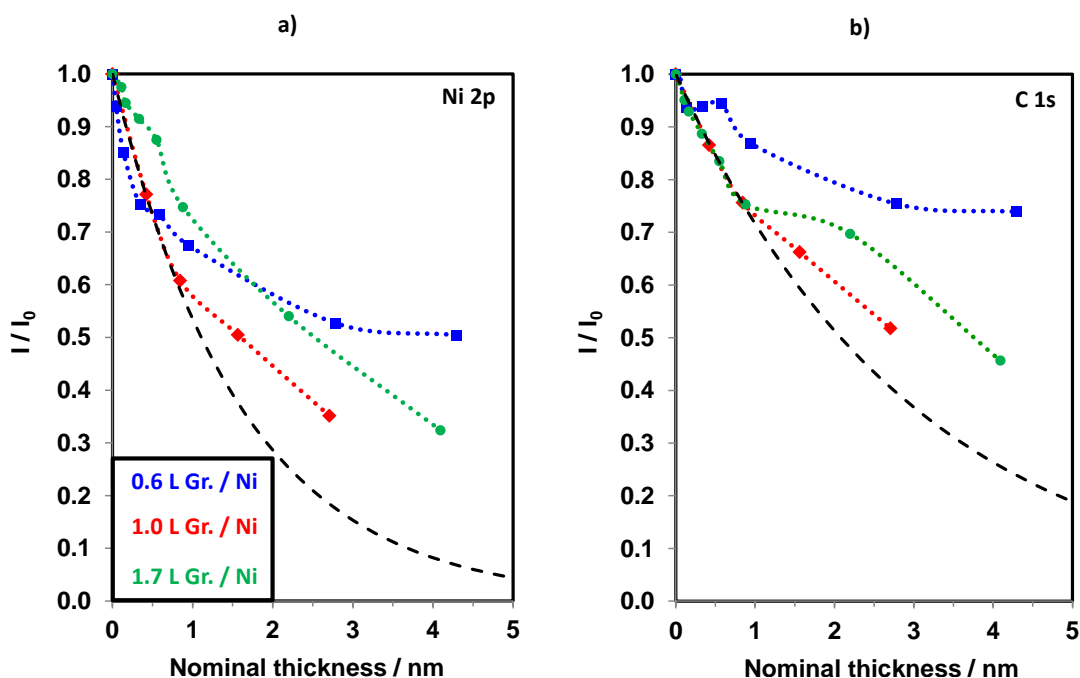


Figure 8.3: Attenuation of the Ni 2p and the C 1s substrate signals upon IL deposition in  $0^\circ$  emission compared to the expected theoretical attenuation for 2D layer-by-layer growth (dashed lines).

One possible explanation for these findings could be the intercalation of IL ions in between the graphene layers. With the IL located underneath a graphene layer, reduced intensity for IL-related XPS signals is expected due to attenuation. Intercalation in between the Ni(111) surface and the first layer of graphene does not seem to be likely as there is no accordant indication for the one layer graphene system. Also the strong interaction<sup>185</sup> of graphene on Ni(111) would most likely prevent this type of intercalation. As known from literature, solvated graphene

flakes can be produced by ultra-sonication of graphite in ILs.<sup>186</sup> Here, the expected rather small size of the second layer graphene patches, as well as the strong interaction of the first graphene layer with the Ni substrate might facilitate the intercalation of the IL without ultra-sonication.

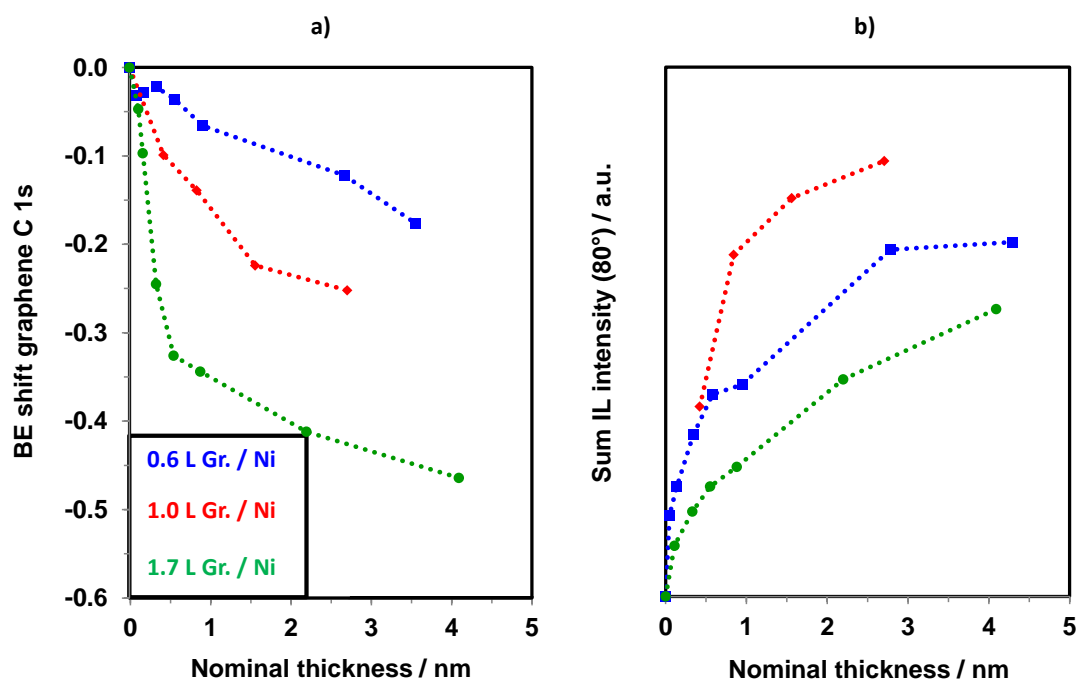


Figure 8.4: a) Graphene C 1s BE shift upon IL deposition with increasing IL coverage. b) Sum of the 80° intensity of all measured IL related XPS signals with increasing IL coverage.

## 8.2. Au 4f Data – [C<sub>2</sub>C<sub>1</sub>Im][OTf] / Pd / Au(111)

Figure 8.5. shows the complementary Au 4f spectra in addition to the Au 4d / Pd 3d spectra shown in section 4.2.7. (Figure 4.19).

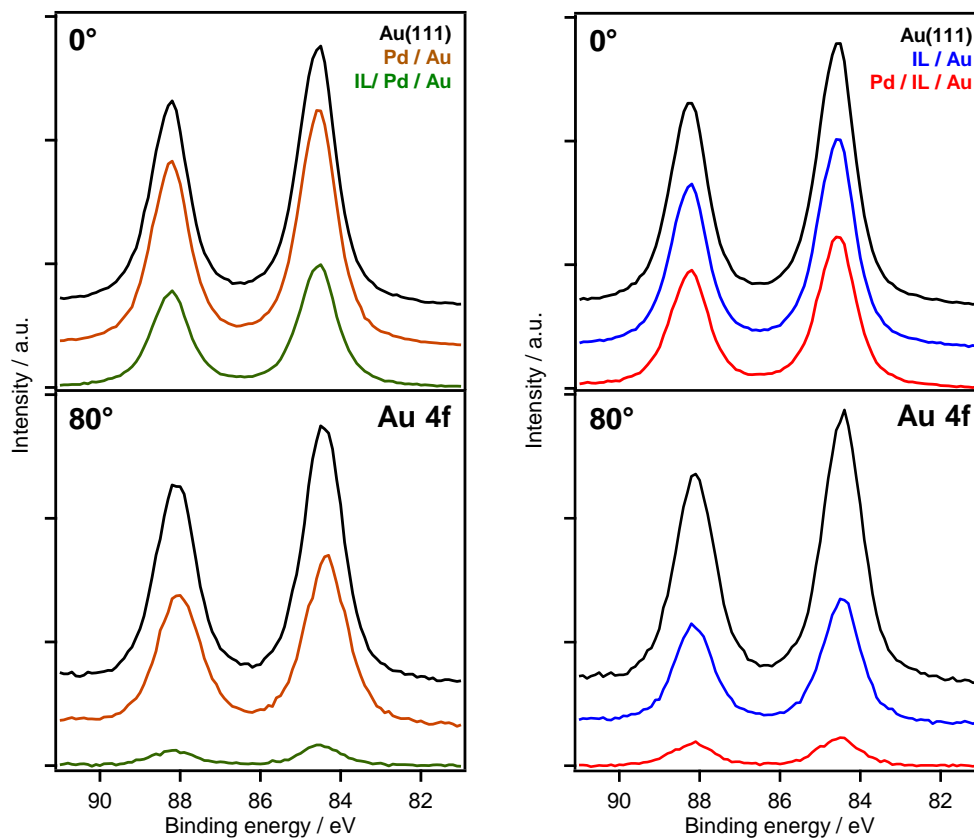


Figure 8.5: Bulk sensitive 0° (first row) and surface sensitive 80° (second row) spectra of the Au 4f region for the sequence 1.6 Å (0.7 ML) Pd on Au(111) followed by deposition of nominally 23 Å (~3 ML) [C<sub>2</sub>C<sub>1</sub>Im][OTf] (left column) and the sequence 23 Å [C<sub>2</sub>C<sub>1</sub>Im][OTf] on Au(111) followed by the deposition of 1.6 Å Pd (right column). All experiments were carried out at RT.

## 9. Bibliography

1. Freemantle, M., *An Introduction to Ionic Liquids*. Royal Society of Chemistry: 2010.
2. Walden, P., *Bull. Acad. Imp. Sci. St. Petersburg* **1914**, 1800.
3. Web of Science. <https://webofknowledge.com> (04/04/2016),
4. Welton, T., Ionic liquids in catalysis. *Coordination Chemistry Reviews* **2004**, 248, (21–24), 2459-2477.
5. Welton, T., Room-Temperature Ionic Liquids. Solvents for Synthesis and Catalysis. *Chem. Rev.* **1999**, 99, (8), 2071-2084.
6. Susan, M. A. B. H.; Noda, A.; Mitsushima, S.; Watanabe, M., Bronsted acid-base ionic liquids and their use as new materials for anhydrous proton conductors. *Chem Commun* **2003**, (8), 938-939.
7. Belieres, J.-P.; Gervasio, D.; Angell, C. A., Binary inorganic salt mixtures as high conductivity liquid electrolytes for >100 [degree]C fuel cells. *Chem Commun* **2006**, (46), 4799-4801.
8. Endres, F.; MacFarlane, D.; Abbott, A., *Electrodeposition from Ionic Liquids*. Wiley: 2008.
9. Abbott, A. P.; Frisch, G.; Ryder, K. S., Electroplating Using Ionic Liquids. In *Annual Review of Materials Research, Vol 43*, Clarke, D. R., Ed. Annual Reviews: Palo Alto, 2013; Vol. 43, pp 335-358.
10. Liu, Z.; Abedin, S. Z. E.; Endres, F., Electrodeposition of zinc films from ionic liquids and ionic liquid/water mixtures. *Electrochim. Acta* **2013**, 89, 635-643.
11. Ujjain, S. K.; Sahu, V.; Sharma, R. K.; Singh, G., High performance, All solid state, flexible Supercapacitor based on Ionic liquid functionalized Graphene. *Electrochim. Acta* **2015**, 157, 245-251.
12. Romann, T.; Oll, O.; Pikma, P.; Kirsimäe, K.; Lust, E., 4–10 V capacitors with graphene-based electrodes and ionic liquid electrolyte. *Journal of Power Sources* **2015**, 280, 606-611.
13. Sato, T.; Masuda, G.; Takagi, K., Electrochemical properties of novel ionic liquids for electric double layer capacitor applications. *Electrochim. Acta* **2004**, 49, (21), 3603-3611.
14. Lockett, V.; Sedev, R.; Ralston, J.; Horne, M.; Rodopoulos, T., Differential Capacitance of the Electrical Double Layer in Imidazolium-Based Ionic Liquids: Influence of Potential, Cation Size, and Temperature. *The Journal of Physical Chemistry C* **2008**, 112, (19), 7486-7495.

15. Fedorov, M. V.; Kornyshev, A. A., Towards understanding the structure and capacitance of electrical double layer in ionic liquids. *Electrochim. Acta* **2008**, 53, (23), 6835-6840.
16. Silva, F.; Gomes, C.; Figueiredo, M.; Costa, R.; Martins, A.; Pereira, C. M., The electrical double layer at the [BMIM][PF<sub>6</sub>] ionic liquid/electrode interface – Effect of temperature on the differential capacitance. *Journal of Electroanalytical Chemistry* **2008**, 622, (2), 153-160.
17. Wang, P.; Zakeeruddin, S. M.; Moser, J.-E.; Grätzel, M., A New Ionic Liquid Electrolyte Enhances the Conversion Efficiency of Dye-Sensitized Solar Cells. *The Journal of Physical Chemistry B* **2003**, 107, (48), 13280-13285.
18. Kawano, R.; Matsui, H.; Matsuyama, C.; Sato, A.; Susan, M. A. B. H.; Tanabe, N.; Watanabe, M., High performance dye-sensitized solar cells using ionic liquids as their electrolytes. *Journal of Photochemistry and Photobiology A: Chemistry* **2004**, 164, (1–3), 87-92.
19. Wang, P.; Zakeeruddin, S. M.; Comte, P.; Exnar, I.; Grätzel, M., Gelation of Ionic Liquid-Based Electrolytes with Silica Nanoparticles for Quasi-Solid-State Dye-Sensitized Solar Cells. *J. Am. Chem. Soc.* **2003**, 125, (5), 1166-1167.
20. Fabregat-Santiago, F.; Bisquert, J.; Palomares, E.; Otero, L.; Kuang, D.; Zakeeruddin, S. M.; Grätzel, M., Correlation between Photovoltaic Performance and Impedance Spectroscopy of Dye-Sensitized Solar Cells Based on Ionic Liquids. *The Journal of Physical Chemistry C* **2007**, 111, (17), 6550-6560.
21. Kernchen, U.; Etzold, B.; Korth, W.; Jess, A., Solid Catalyst with Ionic Liquid Layer (SCILL) – A New Concept to Improve Selectivity Illustrated by Hydrogenation of Cyclooctadiene. *Chemical Engineering & Technology* **2007**, 30, (8), 985-994.
22. Werner, S.; Szesni, N.; Kaiser, M.; Haumann, M.; Wasserscheid, P., A Scalable Preparation Method for SILP and SCILL Ionic Liquid Thin-Film Materials. *Chemical Engineering & Technology* **2012**, 35, (11), 1962-1967.
23. Steinrück, H. P.; Libuda, J.; Wasserscheid, P.; Cremer, T.; Kolbeck, C.; Laurin, M.; Maier, F.; Sobota, M.; Schulz, P. S.; Stark, M., Surface Science and Model Catalysis with Ionic Liquid-Modified Materials. *Adv. Mater.* **2011**, 23, (22-23), 2571-2587.
24. Steinrück, H.-P., Recent developments in the study of ionic liquid interfaces using X-ray photoelectron spectroscopy and potential future directions. *Phys Chem Chem Phys* **2012**, 14, (15), 5010-5029.
25. Kolbeck, C.; Killian, M.; Maier, F.; Paape, N.; Wasserscheid, P.; Steinrück, H. P., Surface characterization of functionalized imidazolium-based ionic liquids. *Langmuir* **2008**, 24, (17), 9500-9507.
26. Maier, F.; Cremer, T.; Kolbeck, C.; Lovelock, K. R. J.; Paape, N.; Schulz, P. S.; Wasserscheid, P.; Steinrück, H.-P., Insights into the surface composition and enrichment effects of ionic liquids and ionic liquids mixtures. *Phys Chem Chem Phys* **2010**, 12, 1905 - 1915.

27. Steinruck, H. P.; Libuda, J.; Wasserscheid, P.; Cremer, T.; Kolbeck, C.; Laurin, M.; Maier, F.; Sobota, M.; Schulz, P. S.; Stark, M., Surface science and model catalysis with ionic liquid-modified materials. *Adv Mater* **2011**, *23*, (22-23), 2571-87.
28. Hofft, O.; Bahr, S.; Himmerlich, M.; Krischok, S.; Schaefer, J. A.; Kempter, V., Electronic structure of the surface of the ionic liquid [EMIM][Tf<sub>2</sub>N] studied by metastable impact electron spectroscopy (MIES), UPS, and XPS. *Langmuir* **2006**, *22*, (17), 7120-7123.
29. Krischok, S.; Eremtchenko, M.; Himmerlich, M.; Lorenz, P.; Uhlig, J.; Neumann, A.; Ötting, R.; Beenken, W. J. D.; Höfft, O.; Bahr, S.; Kempter, V.; Schaefer, J. A., Temperature-Dependent Electronic and Vibrational Structure of the 1-Ethyl-3-methylimidazolium Bis(trifluoromethylsulfonyl)amide Room-Temperature Ionic Liquid Surface: A Study with XPS, UPS, MIES, and HREELS. *The Journal of Physical Chemistry B* **2007**, *111*, (18), 4801-4806.
30. Nishi, T.; Iwahashi, T.; Yamane, H.; Ouchi, Y.; Kanai, K.; Seki, K., Electronic structures of ionic liquids and studied by ultraviolet photoemission, inverse photoemission, and near-edge X-ray absorption fine structure spectroscopies. *Chem. Phys. Lett.* **2008**, *455*, (4-6), 213-217.
31. Yoshimura, D.; Yokoyama, T.; Nishi, T.; Ishii, H.; Ozawa, R.; Hamaguchi, H.; Seki, K., Electronic structure of ionic liquids at the surface studied by UV photoemission. *J Electron Spectrosc* **2005**, *144*, 319-322.
32. Ehlert, C.; Holzweber, M.; Lippitz, A.; Unger, W. E. S.; Saalfrank, P., A detailed assignment of NEXAFS resonances of imidazolium based ionic liquids. *Phys Chem Chem Phys* **2016**.
33. Rodrigues, F.; do Nascimento, G. M.; Santos, P. S., Studies of ionic liquid solutions by soft X-ray absorption spectroscopy. *J Electron Spectrosc* **2007**, *155*, (1-3), 148-154.
34. Caporali, S.; Bardi, U.; Lavacchi, A., X-ray photoelectron spectroscopy and low energy ion scattering studies on 1-butyl-3-methyl-imidazolium bis(trifluoromethane) sulfonimide. *J Electron Spectrosc* **2006**, *151*, (1), 4-8.
35. Minami, I.; Kita, M.; Kubo, T.; Nanao, H.; Mori, S., The Tribological Properties of Ionic Liquids Composed of Trifluorotris(pentafluoroethyl) Phosphate as a Hydrophobic Anion. *Tribol. Lett.* **2008**, *30*, (3), 215-223.
36. Souda, R., Glass-Liquid Transition, Crystallization, and Melting of a Room Temperature Ionic Liquid: Thin Films of 1-Ethyl-3-methylimidazolium Bis[trifluoromethanesulfonyl]imide Studied with TOF-SIMS. *The Journal of Physical Chemistry B* **2008**, *112*, (48), 15349-15354.
37. Kamimura, H.; Kubo, T.; Minami, I.; Mori, S., Effect and mechanism of additives for ionic liquids as new lubricants. *Tribol. Int.* **2007**, *40*, (4), 620-625.
38. Baldelli, S., Surface Structure at the Ionic Liquid-Electrified Metal Interface. *Accounts Chem. Res.* **2008**, *41*, (3), 421-431.

39. Baldelli, S., Interfacial Structure of Room-Temperature Ionic Liquids at the Solid–Liquid Interface as Probed by Sum Frequency Generation Spectroscopy. *The Journal of Physical Chemistry Letters* **2013**, 4, (2), 244-252.
40. Uhl, B.; Cremer, T.; Roos, M.; Maier, F.; Steinrueck, H.-P.; Behm, R. J., At the ionic liquid|metal interface: structure formation and temperature dependent behavior of an ionic liquid adlayer on Au(111). *Phys Chem Chem Phys* **2013**, 15, (40), 17295-17302.
41. Druschler, M.; Borisenko, N.; Wallauer, J.; Winter, C.; Huber, B.; Endres, F.; Roling, B., New insights into the interface between a single-crystalline metal electrode and an extremely pure ionic liquid: slow interfacial processes and the influence of temperature on interfacial dynamics. *Phys Chem Chem Phys* **2012**, 14, (15), 5090-5099.
42. Wen, R.; Rahn, B.; Magnussen, O. M., Potential-Dependent Adlayer Structure and Dynamics at the Ionic Liquid/Au(111) Interface: A Molecular-Scale In Situ Video-STM Study. *Angewandte Chemie International Edition* **2015**, 54, (20), 6062-6066.
43. Li, H.; Endres, F.; Atkin, R., Effect of alkyl chain length and anion species on the interfacial nanostructure of ionic liquids at the Au(111)-ionic liquid interface as a function of potential. *Phys Chem Chem Phys* **2013**, 15, (35), 14624-14633.
44. Lauw, Y.; Horne, M. D.; Rodopoulos, T.; Lockett, V.; Akgun, B.; Hamilton, W. A.; Nelson, A. R. J., Structure of [C4mpyr][NTf2] Room-Temperature Ionic Liquid at Charged Gold Interfaces. *Langmuir* **2012**, 28, (19), 7374-7381.
45. Cremer, T.; Killian, M.; Gottfried, J. M.; Paape, N.; Wasserscheid, P.; Maier, F.; Steinrueck, H. P., Physical Vapor Deposition of [EMIM][Tf2N]: A New Approach to the Modification of Surface Properties with Ultrathin Ionic Liquid Films. *ChemPhysChem* **2008**, 9, 2185-2190.
46. Cremer, T.; Stark, M.; Deyko, A.; Steinrueck, H. P.; Maier, F., Liquid/Solid Interface of Ultrathin Ionic Liquid Films: [C1C1Im][Tf2N] and [C8C1Im][Tf2N] on Au(111). *Langmuir* **2011**, 27, (7), 3662-3671.
47. Cremer, T.; Wibmer, L.; Calderon, S. K.; Deyko, A.; Maier, F.; Steinrueck, H. P., Interfaces of ionic liquids and transition metal surfaces-adsorption, growth, and thermal reactions of ultrathin [C1C1Im][Tf2N] films on metallic and oxidised Ni(111) surfaces. *Phys Chem Chem Phys* **2012**, 14, (15), 5153-5163.
48. Deyko, A.; Cremer, T.; Rietzler, F.; Perkin, S.; Crowhurst, L.; Welton, T.; Steinrueck, H.-P.; Maier, F., Interfacial Behavior of Thin Ionic Liquid Films on Mica. *The Journal of Physical Chemistry C* **2013**, 117, (10), 5101-5111.
49. Kirchner, B.; Clare, B., *Ionic Liquids*. Springer: 2009.
50. Scrosati, B.; Abraham, K. M.; van Schalkwijk, W. A.; Hassoun, J., *Lithium Batteries: Advanced Technologies and Applications*. Wiley: 2013.
51. Saha, B.; Fan, M.; Wang, J., *Sustainable Catalytic Processes*. Elsevier Science: 2015.

52. Abedin, S. Z. E.; Polleth, M.; Meiss, S. A.; Janek, J.; Endres, F., Ionic liquids as green electrolytes for the electrodeposition of nanomaterials. *Green Chem.* **2007**, 9, (6), 549-553.
53. Zaitsau, D. H.; Kabo, G. J.; Strechan, A. A.; Paulechka, Y. U.; Tschersich, A.; Verevkin, S. P.; Heintz, A., Experimental vapor pressures of 1-alkyl-3-methylimidazolium bis(trifluoromethylsulfonyl) imides and a correlation scheme for estimation of vaporization enthalpies of ionic liquids. *J. Phys. Chem. A* **2006**, 110, (22), 7303-7306.
54. Kosmulski, M.; Gustafsson, J.; Rosenholm, J. B., Thermal stability of low temperature ionic liquids revisited. *Thermochim. Acta* **2004**, 412, (1-2), 47-53.
55. Ngo, H. L.; LeCompte, K.; Hargens, L.; McEwen, A. B., Thermal properties of imidazolium ionic liquids. *Thermochim. Acta* **2000**, 357-358, 97-102.
56. Rietzler, F.; Piermaier, M.; Deyko, A.; Steinrück, H.-P.; Maier, F., Electro spray Ionization Deposition of Ultrathin Ionic Liquid Films:  $[C_8C_1Im]Cl$  and  $[C_8C_1Im][Tf_2N]$  on Au(111). *Langmuir* **2014**, 30, (4), 1063-1071.
57. Nobuoka, K.; Kitaoka, S.; Iio, M.; Harran, T.; Ishikawa, Y., Solute-solvent interactions in imidazolium camphorsulfonate ionic liquids. *Phys Chem Chem Phys* **2007**, 9, (44), 5891-5896.
58. Xu, Y.; Li, T.; Peng, C.; Liu, H., Influence of C2-H of Imidazolium-Based Ionic Liquids on the Interaction and Vapor-Liquid Equilibrium of Ethyl Acetate + Ethanol System:  $[Bmim]BF_4$  vs  $[Bmmim]BF_4$ . *Ind Eng Chem Res* **2015**, 54, (36), 9038-9045.
59. Aggarwal, A.; Lancaster, N. L.; Sethi, A. R.; Welton, T., The role of hydrogen bonding in controlling the selectivity of Diels-Alder reactions in room-temperature ionic liquids. *Green Chem.* **2002**, 4, 517-520.
60. Znamenskiy, V.; Kobrak, M. N., Molecular Dynamics Study of Polarity in Room-Temperature Ionic Liquids. *The Journal of Physical Chemistry B* **2004**, 108, (3), 1072-1079.
61. Dieter, K. M.; Dymek, C. J.; Heimer, N. E.; Rovang, J. W.; Wilkes, J. S., Ionic structure and interactions in 1-methyl-3-ethylimidazolium chloride-aluminum chloride molten salts. *J. Am. Chem. Soc.* **1988**, 110, (9), 2722-2726.
62. Zahn, S.; Uhlig, F.; Thar, J.; Spickermann, C.; Kirchner, B., Intermolecular Forces in an Ionic Liquid ( $[Mmim][Cl]$ ) versus Those in a Typical Salt ( $NaCl$ )<sup>13</sup>. *Angewandte Chemie International Edition* **2008**, 47, (19), 3639-3641.
63. López-Martin, I.; Burello, E.; Davey, P. N.; Seddon, K. R.; Rothenberg, G., Anion and Cation Effects on Imidazolium Salt Melting Points: A Descriptor Modelling Study. *ChemPhysChem* **2007**, 8, (5), 690-695.
64. Nockemann, P.; Thijs, B.; Pittois, S.; Thoen, J.; Glorieux, C.; Van Hecke, K.; Van Meervelt, L.; Kirchner, B.; Binnemans, K., Task-Specific Ionic Liquid for Solubilizing Metal Oxides. *The Journal of Physical Chemistry B* **2006**, 110, (42), 20978-20992.

65. Wasserscheid, P.; Welton, T., *Ionic liquids in synthesis*. 2nd ed.; Wiley-VCH: Weinheim, 2008.
66. Zhang, Q.-G.; Wang, N.-N.; Yu, Z.-W., The Hydrogen Bonding Interactions between the Ionic Liquid 1-Ethyl-3-Methylimidazolium Ethyl Sulfate and Water. *The Journal of Physical Chemistry B* **2010**, 114, (14), 4747-4754.
67. Heym, F.; Etzold, B. J. M.; Kern, C.; Jess, A., An improved method to measure the rate of vaporisation and thermal decomposition of high boiling organic and ionic liquids by thermogravimetric analysis. *Phys Chem Chem Phys* **2010**, 12, (38), 12089-12100.
68. Deyko, A.; Lovelock, K. R. J.; Corfield, J.-A.; Taylor, A. W.; Gooden, P. N.; Villar-Garcia, I. J.; Licence, P.; Jones, R. G.; Krasovskiy, V. G.; Chernikova, E. A.; Kustov, L. M., Measuring and predicting [capital Delta]vapH298 values of ionic liquids. *Phys Chem Chem Phys* **2009**, 11, (38), 8544-8555.
69. Huddleston, J. G.; Visser, A. E.; Reichert, W. M.; Willauer, H. D.; Broker, G. A.; Rogers, R. D., Characterization and comparison of hydrophilic and hydrophobic room temperature ionic liquids incorporating the imidazolium cation. *Green Chem.* **2001**, 3, (4), 156-164.
70. Tokuda, H.; Hayamizu, K.; Ishii, K.; Susan, M. A. B. H.; Watanabe, M., Physicochemical Properties and Structures of Room Temperature Ionic Liquids. 1. Variation of Anionic Species. *The Journal of Physical Chemistry B* **2004**, 108, (42), 16593-16600.
71. Kolbeck, C.; Lehmann, J.; Lovelock, K. R. J.; Cremer, T.; Paape, N.; Wasserscheid, P.; Fröba, A. P.; Maier, F.; Steinrück, H.-P., Density and Surface Tension of Ionic Liquids. *The Journal of Physical Chemistry B* **2010**, 114, (51), 17025-17036.
72. Kulkarni, P. S.; Branco, L. C.; Crespo, J. G.; Nunes, M. C.; Raymundo, A.; Afonso, C. A. M., Comparison of Physicochemical Properties of New Ionic Liquids Based on Imidazolium, Quaternary Ammonium, and Guanidinium Cations. *Chemistry – A European Journal* **2007**, 13, (30), 8478-8488.
73. Bonhôte, P.; Dias, A. P.; Papageorgiou, N.; Kalyanasundaram, K.; Grätzel, M., Hydrophobic, highly conductive ambient-temperature molten salts. *Inorg. Chem.* **1996**, 35, (5), 1168-1178.
74. Tariq, M.; Freire, M. G.; Saramago, B.; Coutinho, J. A. P.; Lopes, J. N. C.; Rebelo, L. P. N., Surface tension of ionic liquids and ionic liquid solutions. *Chem Soc Rev* **2012**, 41, (2), 829-868.
75. Fernández, A.; Torrecilla, J. S.; García, J.; Rodríguez, F., Thermophysical Properties of 1-Ethyl-3-methylimidazolium Ethylsulfate and 1-Butyl-3-methylimidazolium Methylsulfate Ionic Liquids. *Journal of Chemical & Engineering Data* **2007**, 52, (5), 1979-1983.
76. Jacquemin, J.; Husson, P.; Padua, A. A. H.; Majer, V., Density and viscosity of several pure and water-saturated ionic liquids. *Green Chem.* **2006**, 8, (2), 172-180.

- 
77. Martino, W.; de la Mora, J. F.; Yoshida, Y.; Saito, G.; Wilkes, J., Surface tension measurements of highly conducting ionic liquids. *Green Chem.* **2006**, 8, (4), 390-397.
78. Hertz, H., Ueber einen Einfluss des ultravioletten Lichtes auf die elektrische Entladung. *Annalen der Physik* **1887**, 267, (8), 983-1000.
79. Einstein, A., The photoelectric effect. *Ann. Phys* **1905**, 17, (132), 4.
80. van der Heide, P., *X-ray Photoelectron Spectroscopy: An introduction to Principles and Practices*. Wiley: 2011.
81. Vickerman, J. C.; Gilmore, I., *Surface Analysis: The Principal Techniques*. Wiley: 2011.
82. Watts, J. F.; Wolstenholme, J., *An Introduction to Surface Analysis by XPS and AES*. Wiley: 2003.
83. Seah, M. P.; Dench, W. A., Quantitative electron spectroscopy of surfaces: A standard data base for electron inelastic mean free paths in solids. *Surf. Interface Anal.* **1979**, 1, (1), 2-11.
84. Hofmann, S., *Auger- and X-Ray Photoelectron Spectroscopy in Materials Science: A User-Oriented Guide*. Springer Berlin Heidelberg: 2012.
85. O'Connor, J.; Sexton, B.; Smart, R., *Surface Analysis Methods in Materials Science*. Springer Berlin Heidelberg: 2013.
86. Cremer, T., *Ionic Liquid Bulk and Interface Properties: Electronic Interaction, Molecular Orientation and Growth Characteristics*. Springer International Publishing: 2013.
87. Probst, M., PhD Thesis, Friedrich-Alexander University Erlangen-Nürnberg. **2003**.
88. Shen, C.; Buck, M.; Wilton-Ely, J. D. E. T.; Weidner, T.; Zharnikov, M., On the Importance of Purity for the Formation of Self-Assembled Monolayers from Thiocyanates. *Langmuir* **2008**, 24, (13), 6609-6615.
89. Dedkov, Y. S.; Fonin, M.; Rüdiger, U.; Laubschat, C., Rashba Effect in the Graphene/Ni(111) System. *Physical Review Letters* **2008**, 100, (10), 107602.
90. Gamo, Y.; Nagashima, A.; Wakabayashi, M.; Terai, M.; Oshima, C., Atomic structure of monolayer graphite formed on Ni(111). *Surf. Sci.* **1997**, 374, (1-3), 61-64.
91. Rosei, R.; De Crescenzi, M.; Sette, F.; Quaresima, C.; Savoia, A.; Perfetti, P., Structure of graphitic carbon on Ni(111): A surface extended-energy-loss fine-structure study. *Phys. Rev. B* **1983**, 28, (2), 1161-1164.
92. Odahara, G.; Otani, S.; Oshima, C.; Suzuki, M.; Yasue, T.; Koshikawa, T., In-situ observation of graphene growth on Ni(111). *Surf. Sci.* **2011**, 605, (11-12), 1095-1098.
93. Koel, B. E.; Sellidj, A.; Paffett, M. T., Ultrathin films of Pd on Au(111): Evidence for surface alloy formation. *Phys. Rev. B* **1992**, 46, (12), 7846-7856.
94. Deyko, A.; Bajus, S.; Rietzler, F.; Bösmann, A.; Wasserscheid, P.; Steinrück, H.-P.; Maier, F., Interface Properties and Physico-Chemical

Characterization of the Low Temperature Molten Salt Li/K/Cs Acetate. *The Journal of Physical Chemistry C* **2013**.

95. Roberts, R. F.; Allara, D. L.; Pryde, C. A.; Buchanan, D. N. E.; Hobbins, N. D., Mean free path for inelastic scattering of 1.2 keV electrons in thin poly(methylmethacrylate) films. *Surf. Interf. Anal.* **1980**, 2, 5-10.

96. Lovelock, K. R. J.; Kolbeck, C.; Cremer, T.; Paape, N.; Schulz, P. S.; Wasserscheid, P.; Maier, F.; Steinrück, H. P., Influence of Different Substituents on the Surface Composition of Ionic Liquids Studied Using ARXPS. *J Phys Chem B* **2009**, 113, (9), 2854-2864.

97. Köhl, A., *Micro-spectroscopic investigation of valence change processes in resistive switching SrTiO<sub>3</sub> thin films*. Forschungszentrum Jülich, Zentralbibliothek: 2014.

98. Wagner, C. D.; Davis, L. E.; Zeller, M. V.; Taylor, J. A.; Raymond, R. H.; Gale, L. H., Empirical atomic sensitivity factors for quantitative analysis by electron spectroscopy for chemical analysis. *Surf. Interface Anal.* **1981**, 3, (5), 211-225.

99. Rietzler, F.; Nagengast, J.; Steinrück, H. P.; Maier, F., Interface of Ionic Liquids and Carbon: Ultrathin [C<sub>1</sub>C<sub>1</sub>Im][Tf<sub>2</sub>N] Films on Graphite and Graphene. *The Journal of Physical Chemistry C* **2015**, 119, (50), 28068-28076.

100. Katsnelson, M. I., Graphene: carbon in two dimensions. *Materials Today* **2007**, 10, (1-2), 20-27.

101. Tour, J. M., Top-down versus bottom-up fabrication of graphene-based electronics. *Chem. Mat.* **2013**, 26, (1), 163-171.

102. Dahal, A.; Batzill, M., Graphene-nickel interfaces: a review. *Nanoscale* **2014**, 6, (5), 2548-2562.

103. Winterlin, J.; Bocquet, M. L., Graphene on metal surfaces. *Surf. Sci.* **2009**, 603, (10-12), 1841-1852.

104. Baldelli, S.; Bao, J.; Wu, W.; Pei, S.-s., Sum frequency generation study on the orientation of room-temperature ionic liquid at the graphene-ionic liquid interface. *Chem. Phys. Lett.* **2011**, 516, (4-6), 171-173.

105. Bovio, S.; Podesta, A.; Lenardi, C.; Milani, P., Evidence of Extended Solidlike Layering in Bmim NTf<sub>2</sub> Ionic Liquid Thin Films at Room-Temperature. *J Phys Chem B* **2009**, 113, (19), 6600-6603.

106. Zhang, F. C.; Sha, M. L.; Ren, X. P.; Wu, G. Z.; Hu, J.; Zhang, Y., Morphology and wettability of [Bmim][PF<sub>6</sub>] ionic liquid on HOPG substrate. *Chinese Physics Letters* **2010**, 27, (8).

107. Atkin, R.; Warr, G. G., Structure in confined room-temperature ionic liquids. *J. Phys. Chem. C* **2007**, 111, (13), 5162-5168.

108. Ghatee, M. H.; Moosavi, F., Physisorption of hydrophobic and hydrophilic 1-alkyl-3-methylimidazolium ionic liquids on the graphenes. *J. Phys. Chem. C* **2011**, 115, (13), 5626-5636.

109. Fedorov, M. V.; Lynden-Bell, R. M., Probing the neutral graphene-ionic liquid interface: Insights from molecular dynamics simulations. *Phys Chem Chem Phys* **2012**, 14, (8), 2552-2556.

110. Maolin, S.; Fuchun, Z.; Guozhong, W.; Haiping, F.; Chunlei, W.; Shimou, C.; Yi, Z.; Jun, H., Ordering layers of [bmim][PF<sub>6</sub>] ionic liquid on graphite surfaces: Molecular dynamics simulation. *The Journal of Chemical Physics* **2008**, 128, (13), 134504.
111. Kislenco, S. A.; Samoylov, I. S.; Amirov, R. H., Molecular dynamics simulation of the electrochemical interface between a graphite surface and the ionic liquid [BMIM][PF<sub>6</sub>]. *Phys Chem Chem Phys* **2009**, 11, (27), 5584-5590.
112. Steinrück, H. P.; Huber, W.; Pache, T.; Menzel, D., The adsorption of benzene mono- and multilayers on Ni(111) studied by TPD and LEED. *Surf. Sci.* **1989**, 218, (2-3), 293-316.
113. Zhao, W.; Kozlov, S. M.; Höfert, O.; Gotterbarm, K.; Lorenz, M. P. A.; Viñes, F.; Papp, C.; Görling, A.; Steinrück, H.-P., Graphene on Ni(111): Coexistence of Different Surface Structures. *The Journal of Physical Chemistry Letters* **2011**, 2, (7), 759-764.
114. Rafiee, J.; Mi, X.; Gullapalli, H.; Thomas, A. V.; Yavari, F.; Shi, Y.; Ajayan, P. M.; Koratkar, N. A., Wetting transparency of graphene. *Nat Mater* **2012**, 11, (3), 217-222.
115. Bermúdez, M.-D.; Jiménez, A.-E.; Sanes, J.; Carrión, F.-J., Ionic Liquids as Advanced Lubricant Fluids. *Molecules* **2009**, 14, (8), 2888.
116. Somers, A.; Howlett, P.; MacFarlane, D.; Forsyth, M., A Review of Ionic Liquid Lubricants. *Lubricants* **2013**, 1, (1), 3.
117. Armand, M.; Endres, F.; MacFarlane, D. R.; Ohno, H.; Scrosati, B., Ionic-liquid materials for the electrochemical challenges of the future. *Nat Mater* **2009**, 8, (8), 621-629.
118. Tsuda, T.; Hussey, C. L., Electrochemistry of Room-Temperature Ionic Liquids and Melts. In *Modern Aspects of Electrochemistry*, No. 45, White, E. R., Ed. Springer New York: New York, NY, 2009; pp 63-174.
119. Olivier-Bourbigou, H.; Magna, L.; Morvan, D., Ionic liquids and catalysis: Recent progress from knowledge to applications. *Applied Catalysis A: General* **2010**, 373, (1-2), 1-56.
120. Steinrück, H.-P.; Wasserscheid, P., Ionic Liquids in Catalysis. *Catalysis Letters* **2014**, 145, (1), 380-397.
121. Rivera-Rubero, S.; Baldelli, S., Surface spectroscopy of room-temperature ionic liquids on a platinum electrode: A sum frequency generation study. *J Phys Chem B* **2004**, 108, (39), 15133-15140.
122. Endres, F.; Borisenko, N.; El Abedin, S. Z.; Hayes, R.; Atkin, R., The interface ionic liquid(s)/electrode(s): in situ STM and AFM measurements. *Faraday discussions* **2012**, 154, 221-33; discussion 313-33, 465-71.
123. Henriksen, T.; Juhler, R. K.; Svensmark, B.; Cech, N. B., The relative influences of acidity and polarity on responsiveness of small organic molecules to analysis with negative ion electrospray ionization mass spectrometry (ESI-MS). *J Am Soc Mass Spectrom* **2005**, 16, (4), 446-55.

124. Schmidt, A.; Karas, M.; Dülcks, T., Effect of different solution flow rates on analyte ion signals in nano-ESI MS, or: when does ESI turn into nano-ESI? *Journal of the American Society for Mass Spectrometry* **2003**, 14, (5), 492-500.
125. Taylor, G., Disintegration of Water Drops in an Electric Field. *Proceedings of the Royal Society of London. Series A, Mathematical and Physical Sciences* **1964**, 280, (1382), 383-397.
126. Taylor, G., The Force Exerted by an Electric Field on a Long Cylindrical Conductor. *Proceedings of the Royal Society of London. Series A, Mathematical and Physical Sciences* **1966**, 291, (1425), 145-158.
127. Taylor, G., Electrically Driven Jets. *Proceedings of the Royal Society of London. Series A, Mathematical and Physical Sciences* **1969**, 313, (1515), 453-475.
128. Rayleigh, L., XX. On the equilibrium of liquid conducting masses charged with electricity. *Philosophical Magazine Series 5* **1882**, 14, (87), 184-186.
129. Fujiwara, Y.; Saito, N.; Nonaka, H.; Nakanaga, T.; Ichimura, S., A new cluster-ion-beam source for secondary ion mass spectrometry (SIMS) using the electrospray of a pure ionic liquid under high vacuum. *Nuclear Instruments and Methods in Physics Research Section B: Beam Interactions with Materials and Atoms* **2010**, 268, (11-12), 1938-1941.
130. Jackson, G. P.; Duckworth, D. C., Electrospray mass spectrometry of undiluted ionic liquids. *Chem Commun* **2004**, (5), 522-523.
131. Chen, C. H.; Emond, M. H. J.; Kelder, E. M.; Meester, B.; Schoonman, J., ELECTROSTATIC SOL-SPRAY DEPOSITION OF NANOSTRUCTURED CERAMIC THIN FILMS. *Journal of Aerosol Science* **1999**, 30, (7), 959-967.
132. Wilhelm, O.; Pratsinis, S. E.; Perednis, D.; Gauckler, L. J., Electrospray and pressurized spray deposition of yttria-stabilized zirconia films. *Thin Solid Films* **2005**, 479, (1-2), 121-129.
133. Fujitsuka, N.; Sakata, J.; Miyachi, Y.; Mizuno, K.; Ohtsuka, K.; Taga, Y.; Tabata, O., Monolithic pyroelectric infrared image sensor using PVDF thin film. *Sensors and Actuators A: Physical* **1998**, 66, (1-3), 237-243.
134. Hoyer, B.; Sørensen, G.; Jensen, N.; Nielsen, D. B.; Larsen, B., Electrostatic Spraying: A Novel Technique for Preparation of Polymer Coatings on Electrodes. *Anal Chem* **1996**, 68, (21), 3840-3844.
135. Rietveld, I. B.; Kobayashi, K.; Yamada, H.; Matsushige, K., Morphology control of poly(vinylidene fluoride) thin film made with electrospray. *J. Colloid Interface Sci.* **2006**, 298, (2), 639-651.
136. Sakata, J.; Mochizuki, M., Preparation of organic thin films by an electrospray technique I. Crystal forms and their orientation in poly(vinylidene fluoride) films. *Thin Solid Films* **1991**, 195, (1-2), 175-184.
137. Berkland, C.; Pack, D. W.; Kim, K., Controlling surface nano-structure using flow-limited field-injection electrostatic spraying (FFESS) of poly(D,L-lactide-co-glycolide). *Biomaterials* **2004**, 25, (25), 5649-5658.

138. Rietveld, I. B.; Kobayashi, K.; Yamada, H.; Matsushige, K., Electropray Deposition, Model, and Experiment: Toward General Control of Film Morphology. *The Journal of Physical Chemistry B* **2006**, 110, (46), 23351-23364.
139. Armstrong, J. P.; Hurst, C.; Jones, R. G.; Licence, P.; Lovelock, K. R. J.; Satterley, C. J.; Villar-Garcia, I. J., Vapourisation of ionic liquids. *Phys Chem Chem Phys* **2007**, 9, (8), 982-990.
140. Strasser, D.; Goulay, F.; Kelkar, M. S.; Maginn, E. J.; Leone, S. R., Photoelectron spectrum of isolated ion-pairs in ionic liquid vapor. *J. Phys. Chem. A* **2007**, 111, (17), 3191-3195.
141. Alfassi, Z. B.; Huie, R. E.; Milman, B. L.; Neta, P., Electropray ionization mass spectrometry of ionic liquids and determination of their solubility in water. *Anal Bioanal Chem* **2003**, 377, (1), 159-164.
142. Dorbritz, S.; Ruth, W.; Kragl, U., Investigation on Aggregate Formation of Ionic Liquids. *Adv. Synth. Catal.* **2005**, 347, (9), 1273-1279.
143. Dyson, P. J.; Khalaila, I.; Luetzgen, S.; McIndoe, J. S.; Zhao, D., Direct probe electropray (and nanospray) ionization mass spectrometry of neat ionic liquids. *Chem Commun* **2004**, (19), 2204-2205.
144. Juraschek, R.; Dülcks, T.; Karas, M., Nanoelectrospray—more than just a minimized-flow electropray ionization source. *Journal of the American Society for Mass Spectrometry* **1999**, 10, (4), 300-308.
145. Kolbeck, C.; Cremer, T.; Lovelock, K. R. J.; Paape, N.; Schulz, P. S.; Wasserscheid, P.; Maier, F.; Steinrück, H.-P., Influence of Different Anions on the Surface Composition of Ionic Liquids Studied Using ARXPS. *J Phys Chem B* **2009**, 113, (25), 8682-8688.
146. Cremer, T.; Kolbeck, C.; Lovelock, Kevin R. J.; Paape, N.; Wölfel, R.; Schulz, Peter S.; Wasserscheid, P.; Weber, H.; Thar, J.; Kirchner, B.; Maier, F.; Steinrück, H.-P., Towards a Molecular Understanding of Cation-Anion Interactions - Probing the Electronic Structure of Imidazolium Ionic Liquids by NMR Spectroscopy, X-ray Photoelectron Spectroscopy and Theoretical Calculations. *Chemistry - A European Journal* **2010**, 16, (30), 9018-9033.
147. Lovelock, K. R. J.; Armstrong, J. P.; Licence, P.; Jones, R. G., Vaporisation and thermal decomposition of dialkylimidazolium halide ion ionic liquids. *Phys Chem Chem Phys* **2013**.
148. Schmidt, M.; Cubillas, A. M.; Taccardi, N.; Euser, T. G.; Cremer, T.; Maier, F.; Steinrück, H.-P.; Russell, P. S. J.; Wasserscheid, P.; Etzold, B. J. M., Chemical and (Photo)-Catalytical Transformations in Photonic Crystal Fibers. *ChemCatChem* **2013**, 5, (3), 641-650.
149. Voorhees, P. W., The theory of Ostwald ripening. *J Stat Phys* **1985**, 38, (1-2), 231-252.
150. Fernandes, A. M.; Rocha, M. A. A.; Freire, M. G.; Marrucho, I. M.; Coutinho, J. o. A. P.; Santos, L. s. M. N. B. F., Evaluation of Cation–Anion Interaction Strength in Ionic Liquids. *The Journal of Physical Chemistry B* **2011**, 115, (14), 4033-4041.

151. Deetlefs, M.; Hardacre, C.; Nieuwenhuyzen, M.; Padua, A. A. H.; Sheppard, O.; Soper, A. K., Liquid Structure of the Ionic Liquid 1,3-Dimethylimidazolium Bis{(trifluoromethyl)sulfonyl}amide. *The Journal of Physical Chemistry B* **2006**, 110, (24), 12055-12061.
152. Freire, M. G.; Carvalho, P. J.; Fernandes, A. M.; Marrucho, I. M.; Queimada, A. J.; Coutinho, J. A. P., Surface tensions of imidazolium based ionic liquids: Anion, cation, temperature and water effect. *J. Colloid Interface Sci.* **2007**, 314, (2), 621-630.
153. P.J. Linstrom and W.G. Mallard, E., In *NIST Chemistry WebBook, NIST Standard Reference Database Number 69, National Institute of Standards and Technology, Gaithersburg MD, 20899*.
154. SDBSWeb, In National Institute of Advanced Industrial Science and Technology.
155. Kroon, M. C.; Buijs, W.; Peters, C. J.; Witkamp, G.-J., Quantum chemical aided prediction of the thermal decomposition mechanisms and temperatures of ionic liquids. *Thermochim. Acta* **2007**, 465, (1-2), 40-47.
156. Chowdhury, A.; Thynell, S. T., Confined rapid thermolysis/FTIR/ToF studies of imidazolium-based ionic liquids. *Thermochim. Acta* **2006**, 443, (2), 159-172.
157. Thayer, F. K., METHYLETHYL SULFATE AS AN ALKYLATING AGENT. *J. Am. Chem. Soc.* **1924**, 46, (4), 1044-1046.
158. Jacquemin, J.; Goodrich, P.; Jiang, W.; Rooney, D. W.; Hardacre, C., Are Alkyl Sulfate-Based Protic and Aprotic Ionic Liquids Stable with Water and Alcohols? A Thermodynamic Approach. *The Journal of Physical Chemistry B* **2013**, 117, (6), 1938-1949.
159. Wolfenden, R.; Yuan, Y., Monoalkyl sulfates as alkylating agents in water, alkylsulfatase rate enhancements, and the "energy-rich" nature of sulfate half-esters. *Proceedings of the National Academy of Sciences of the United States of America* **2007**, 104, (1), 83-86.
160. Gottfried, J. M.; Maier, F.; Rossa, J.; Gerhard, D.; Schulz, P. S.; Wasserscheid, P.; Steinrück, H. P., Surface studies on the ionic liquid 1-ethyl-3-methylimidazolium ethylsulfate using X-ray photoelectron spectroscopy (XPS). *Z Phys Chem* **2006**, 220, (10-11), 1439-1453.
161. Maier, F.; Gottfried, J. M.; Rossa, J.; Gerhard, D.; Schulz, P. S.; Schwieger, W.; Wasserscheid, P.; Steinrück, H. P., Surface enrichment and depletion effects of ions dissolved in an ionic liquid: an X-ray photoelectron spectroscopy study. *Angew Chem Int Edit* **2006**, 45, (46), 7778-7780.
162. Zebisch, P.; Huber, W.; Steinrück, H. P., Changes in the adsorption and desorption behavior of cyclohexane and benzene on Ni(111) induced by a monoatomic potassium layer. *Surf. Sci.* **1991**, 244, (3), 185-196.
163. Greeley, J.; Mavrikakis, M., Alloy catalysts designed from first principles. *Nat Mater* **2004**, 3, (11), 810-815.

164. Gao, F.; Goodman, D. W., Pd-Au bimetallic catalysts: understanding alloy effects from planar models and (supported) nanoparticles. *Chem Soc Rev* **2012**, 41, (24), 8009-8020.
165. Yi, C. W.; Luo, K.; Wei, T.; Goodman, D. W., The Composition and Structure of Pd–Au Surfaces. *The Journal of Physical Chemistry B* **2005**, 109, (39), 18535-18540.
166. Steinrück, H.-P.; Wasserscheid, P., Ionic Liquids in Catalysis. *Catalysis Letters* **2015**, 145, (1), 380-397.
167. Schernich, S.; Kostyshyn, D.; Wagner, V.; Taccardi, N.; Laurin, M.; Wasserscheid, P.; Libuda, J., Interactions Between the Room-Temperature Ionic Liquid [C<sub>2</sub>C<sub>1</sub>Im][OTf] and Pd(111), Well-Ordered Al<sub>2</sub>O<sub>3</sub>, and Supported Pd Model Catalysts from IR Spectroscopy. *The Journal of Physical Chemistry C* **2014**, 118, (6), 3188-3193.
168. Bauer, T.; Mehl, S.; Brummel, O.; Pohako-Esko, K.; Wasserscheid, P.; Libuda, J., Ligand Effects at Ionic Liquid-Modified Interfaces: Coadsorption of [C<sub>2</sub>C<sub>1</sub>Im][OTf] and CO on Pd(111). *The Journal of Physical Chemistry C* **2016**, 120, (8), 4453-4465.
169. Fernandes, A. M.; Coutinho, J. A. P.; Marrucho, I. M., Gas-phase dissociation of ionic liquid aggregates studied by electrospray ionisation mass spectrometry and energy-variable collision induced dissociation. *Journal of Mass Spectrometry* **2009**, 44, (1), 144-150.
170. Matsuda, T.; Taccardi, N.; Schwegler, J.; Wasserscheid, P.; Steinrück, H.-P.; Maier, F., Inside Cover: Vacuum Surface Science Meets Heterogeneous Catalysis: Dehydrogenation of a Liquid Organic Hydrogen Carrier in the Liquid State (ChemPhysChem 9/2015). *ChemPhysChem* **2015**, 16, (9), 1790-1790.
171. Wowsnick, G.; Teschner, D.; Kasatkin, I.; Girsdies, F.; Armbrüster, M.; Zhang, A.; Grin, Y.; Schlögl, R.; Behrens, M., Surface dynamics of the intermetallic catalyst Pd<sub>2</sub>Ga, Part I – Structural stability in UHV and different gas atmospheres. *J. Catal.* **2014**, 309, 209-220.
172. Kovnir, K.; Armbrüster, M.; Teschner, D.; Venkov, T. V.; Szentmiklósi, L.; Jentoft, F. C.; Knop-Gericke, A.; Grin, Y.; Schlögl, R., In situ surface characterization of the intermetallic compound PdGa – A highly selective hydrogenation catalyst. *Surf. Sci.* **2009**, 603, (10–12), 1784-1792.
173. Hu, P.; Fogler, E.; Diskin-Posner, Y.; Iron, M. A.; Milstein, D., A novel liquid organic hydrogen carrier system based on catalytic peptide formation and hydrogenation. *Nat Commun* **2015**, 6.
174. Teichmann, D.; Stark, K.; Muller, K.; Zottl, G.; Wasserscheid, P.; Arlt, W., Energy storage in residential and commercial buildings via Liquid Organic Hydrogen Carriers (LOHC). *Energy & Environmental Science* **2012**, 5, (10), 9044-9054.
175. Papp, C.; Wasserscheid, P.; Libuda, J.; Steinrück, H.-P., Wasserstoff, chemisch gespeichert. *Nachrichten aus der Chemie* **2014**, 62, (10), 963-969.
176. Markiewicz, M.; Zhang, Y. Q.; Bosmann, A.; Bruckner, N.; Thoming, J.; Wasserscheid, P.; Stolte, S., Environmental and health impact assessment of

Liquid Organic Hydrogen Carrier (LOHC) systems - challenges and preliminary results. *Energy & Environmental Science* **2015**, 8, (3), 1035-1045.

177. T. B. Massalski, H. O., P. R. Subramanian, L. Kacprzak, Binary Alloy Phase Diagrams. *Am. Soc. Metals* **1990**, 2nd Edn.

178. Grabau, M.; Krick Calderón, S.; Rietzler, F.; Niedermaier, I.; Taccardi, N.; Wasserscheid, P.; Maier, F.; Steinrück, H.-P.; Papp, C., Surface enrichment of Pt in Ga<sub>2</sub>O<sub>3</sub> films grown on liquid Pt/Ga alloys. *Surf. Sci.* **2016**, 651, 16-21.

179. Jeurgens, L. P. H.; Sloof, W. G.; Tichelaar, F. D.; Mittemeijer, E. J., Composition and chemical state of the ions of aluminium-oxide films formed by thermal oxidation of aluminium. *Surf. Sci.* **2002**, 506, (3), 313-332.

180. Gabasch, H.; Unterberger, W.; Hayek, K.; Klötzer, B.; Kleimenov, E.; Teschner, D.; Zafeiratos, S.; Hävecker, M.; Knop-Gericke, A.; Schlögl, R.; Han, J.; Ribeiro, F. H.; Aszalos-Kiss, B.; Curtin, T.; Zemlyanov, D., In situ XPS study of Pd(111) oxidation at elevated pressure, Part 2: Palladium oxidation in the 10–1 mbar range. *Surf. Sci.* **2006**, 600, (15), 2980-2989.

181. Titkov, A. I.; Salanov, A. N.; Koscheev, S. V.; Boronin, A. I., Mechanisms of Pd(110) surface reconstruction and oxidation: XPS, LEED and TDS study. *Surf. Sci.* **2006**, 600, (18), 4119-4125.

182. Peuckert, M.; Bonzel, H. P., Characterization of oxidized platinum surfaces by X-ray photoelectron spectroscopy. *Surf. Sci.* **1984**, 145, (1), 239-259.

183. Parkinson, C. R.; Walker, M.; McConville, C. F., Reaction of atomic oxygen with a Pt(111) surface: chemical and structural determination using XPS, CAICISS and LEED. *Surf. Sci.* **2003**, 545, (1–2), 19-33.

184. Fleisch, T. H.; Mains, G. J., Photoreduction and reoxidation of platinum oxide and palladium oxide surfaces. *The Journal of Physical Chemistry* **1986**, 90, (21), 5317-5320.

185. Mittendorfer, F.; Garhofer, A.; Redinger, J.; Klimeš, J.; Harl, J.; Kresse, G., Graphene on Ni(111): Strong interaction and weak adsorption. *Phys. Rev. B* **2011**, 84, (20), 201401.

186. Nuvoli, D.; Valentini, L.; Alzari, V.; Scognamillo, S.; Bon, S. B.; Piccinini, M.; Illescas, J.; Mariani, A., High concentration few-layer graphene sheets obtained by liquid phase exfoliation of graphite in ionic liquid. *J. Mater. Chem.* **2011**, 21, (10), 3428-3431.

---

## List of Abbreviations

AFM	atomic force microscopy
ARXPS	angle-resolved X-ray photoelectron spectroscopy
ASF	atomic sensitivity factor
BE	binding energy
BU	bottom-up
CAW	contact angle of water
CVD	chemical vapor deposition
DFT	density functional theory
EDLC	electric double-layer capacitor
ESCA	electron spectroscopy for chemical analysis
ESI	electrospray ionization
ESID	electrospray ionization deposition
ESI-MS	electrospray ionization mass spectrometry
FWHM	full width at half maximum
HOPG	highly ordered pyrolytic graphite
HREELS	high resolution electron energy loss spectroscopy
HV	high voltage
ICP-AES	inductively coupled plasma atomic emission spectroscopy
ID	information depth
IL	ionic liquid
IL-ESID	electrospray ionization deposition of ionic liquids
IL-PVD	physical vapor deposition of ionic liquids
IMFP	inelastic mean free path
LEED	low energy electron diffraction
LEIS	low energy ion scattering

---

LOHC	liquid organic hydrogen carrier
MDS	molecular dynamics simulations
MIES	metastable impact electron spectroscopy
MP	melting point
MS	mass spectrometry
NEXAFS	near edge X-ray absorption fine structure
OM	optical microscopy
QCM	quartz crystal microbalance
RT	room temperature
SCILL	solid catalyst with ionic liquid layer
SEM	secondary electron multiplier
SFG	sum frequency generation
SILP	supported ionic liquid phase
STM	scanning tunneling microscopy
TD	top-down
ToF-SIMS	time-of- flight secondary ion mass spectrometry
UHV	ultra high vacuum
UPS	ultraviolet photoelectron spectroscopy
XPS	X-ray photoelectron spectroscopy



---

## Acknowledgements

I would like to gratefully acknowledge various people who have helped and supported me in the last years during my work on this thesis.

First, I want to thank my principal supervisor, Prof. Hans-Peter Steinrück, for giving me the opportunity to become part of his workgroup and for all the support he was giving me throughout my time at his institute. Likewise, I would like to acknowledge my second supervisor, Dr. Florian Maier, for his guidance and support and for his constant input of new ideas.

Furthermore, I would like to thank all my fellow colleagues for the unique working atmosphere, in particular the former and present members of the IL group, Till Cremer, Claudia Kolbeck, Alexey Deyko, Inga Niedermaier, Takashi Matsuda, Benjamin May, Patrick Schreiber, and Bettina Heller. Besides, I would like to acknowledge Jens Nagengast, Marius Piermaier, and Johannes Fichtner for their experimental contributions during the work on their master and bachelor theses.

I also want to acknowledge my collaborators working at the same institute, Mathias Grabau and Christian Papp, as well as my collaborators from the Institute of Chemical Reaction Engineering, Prof. Peter Wasserscheid, Prof. Bastian Etzold, Dr. Nicola Taccardi, and Dr. Macarena Munoz Garcia.

I am very grateful to the technical staff of the institute, Hans-Peter Bäumler, Bernd Kress, and Friedhold Wölfel as well as to his co-workers at the mechanical workshop for their technical advice and support, making the design and realization of new experimental setups as convenient as possible.

Last but not least, I want to thank my brothers, Martin and Michael Rietzler, for their editorial assistance. Many thanks also go to the rest of my family, my friends, and my partner, Thomas Konski, for supporting me during the past years and encouraging me through tough times.